A NEW CROSS-OVERLAPPED DECOUPLING COIL STRUCTURE FOR EV DYNAMIC INDUCTIVE WIRELESS CHARGING SYSTEM

YIN JIA LIN

FACULTY OF ENGINEERING

UNIVERSITI MALAYA KUALA LUMPUR

2025

A NEW CROSS-OVERLAPPED DECOUPLING COIL STRUCTURE FOR EV DYNAMIC INDUCTIVE WIRELESS CHARGING SYSTEM

YIN JIA LIN

DISSERTATION SUBMITTED IN PARTIAL FULFILMENT OF THE REQUIREMENTS FOR THE DEGREE OF ENGINEERING SCIENCE

FACULTY OF ENGINEERING UNIVERSITI MALAYA KUALA LUMPUR

2025

UNIVERSITI MALAYA ORIGINAL LITERARY WORK DECLARATION

Name of Candidate: Yin Jialin

Matric No: S2118335

Name of Degree: Master of Engineering Science

Title of Project Paper/Research Report/Dissertation/Thesis ("this Work"):

a new cross-overlapped decoupling coil structure for EV dynamic inductive wireless charging system

Field of Study: Power Electronics (522: Electricity and Energy)

I do solemnly and sincerely declare that:

- (1) I am the sole author/writer of this Work;
- (2) This Work is original;
- (3) Any use of any work in which copyright exists was done by way of fair dealing and for permitted purposes, and any excerpt or extract from, or reference to or reproduction of any copyright work has been disclosed expressly and sufficiently and the title of the Work and its authorship have been acknowledged in this Work;
- (4) I do not have any actual knowledge nor do I ought reasonably to know that the making of this work constitutes an infringement of any copyright work;
- (5) I hereby assign all and every rights in the copyright to this Work to the Universiti Malaya ("UM"), who henceforth shall be owner of the copyright in this Work and that any reproduction or use in any form or by any means whatsoever is prohibited without the written consent of UM having been first had and obtained;
- (6) I am fully aware that if in the course of making this Work I have infringed any copyright whether intentionally or otherwise, I may be subject to legal action or any other action as may be determined by UM.

Candidate's Signature Date: 24th, Feb. 2025

Subscribed and solemnly declared before,

Withess's Signature Date, 24, Feb. 202	Witness's Signature	Date: 24 th , Feb. 2025
--	---------------------	------------------------------------

Name:

Designation:

[A NEW CROSS-OVERLAPPED DECOUPLING COIL STRUCTURE FOR EV DYNAMIC INDUCTIVE WIRELESS CHARGING SYSTEM] ABSTRACT

The multi-transmitter and multi-receiver structure has been extensively discussed in Dynamic Inductive Wireless Charging (DIWC) systems for Electric Vehicles. Multiple coils have already been proven successful in high-power applications. Nevertheless, challenges persist in mitigating the adverse effects of cross-coupling among adjacent multi-coils and achieving higher transfer efficiency and stable output power under dynamic conditions. Thus, this paper proposes a new DIWC magnetic coupler consisting of a cross-overlapped transmitter and single receiver that serves multiple purposes, including decoupling, reduced mutual inductance fluctuation, and achieving high efficiency simultaneously. Moreover, the traversal method uses the finite element analysis tool ANSYS Maxwell to choose the optimized Rx coil turns and size, further improving system performance. A 2kW wireless charging setup is developed to validate the proposed DIWC magnetic coupler. The experimental results show that the output voltage fluctuation can be controlled within ±1%, and the maximum DC-DC efficiency is 92.87%. The longitudinal misalignment performance of the proposed DIWC magnetic coupler is also elaborated in this paper.

Keywords: Coils, decoupling, dynamic inductive wireless charging (DIWC), voltage fluctuations.

[STRUKTUR GANDA TERPISAH BARU UNTUK SISTEM PENGECASAN TANPA WAYAR INDUKTIF DINAMIK KERETA ELEKTRIK]

ABSTRAK

Struktur pemancar dan penerima berganda telah dibincangkan secara meluas dalam sistem Pengecasan Tanpa Wayar Induktif Dinamik(DIWC) untuk Kenderaan Elektrik. Pelbagai gegelung telah terbukti berjaya dalam aplikasi kuasa tinggi. Walau bagaimanapun, cabaran masih wujud dalam mengurangkan kesan buruk daripada saling berhubungan di antara gegelung yang bersebelahan serta dalam mencapai kecekapan pemindahan yang lebih tinggi dan kuasa keluaran yang stabil dalam keadaan dinamik. Oleh itu, kertas ini mencadangkan penyambung magnet DIWC yang baru, terdiri daripada pemancar bersilang dan penerima tunggal yang memenuhi pelbagai tujuan, termasuk pemisahan, pengurangan fluktuasi aruhan salingan, dan pencapaian kecekapan tinggi secara serentak. Selain itu, kaedah traversal menggunakan alat analisis elemen terhingga ANSYS Maxwell untuk memilih giliran dan saiz gegelung Rx yang dioptimumkan, dengan itu meningkatkan prestasi sistem secara lebih lanjut. Sistem pengecasan tanpa wayar 2kW telah dibangunkan untuk mengesahkan penyambung magnet DIWC yang dicadangkan. Keputusan eksperimen menunjukkan bahawa fluktuasi voltan keluaran dapat dikawal dalam lingkungan ±1%, dan kecekapan maksimum DC-DC adalah 92.87%. Prestasi penyelarasan longitudinal penyambung magnet DIWC yang dicadangkan juga diperincikan dalam kertas ini.

Kata kunci: Gegelung, pemisahan, pengecasan tanpa wayar induktif dinamik (DIWC), fluktuasi voltan.

ACKNOWLEDGMENTS

First, I would like to extend my sincere gratitude to my three supervisors, Prof. Dr. Saad Mekhilef, Prof. Dr. Hazlie Bin Mokhlis, and Assoc. Prof. Dr. Tey Kok Soon, for their invaluable guidance, support, and encouragement throughout my master's studies. Their expertise and insightful suggestions have been instrumental in shaping the direction of my research. I learned a lot of things from them in the past three years. Additionally, I deeply appreciate my dear lab mates and my paper co-authors, Peyman Darvish, Amran Hossain, and Mohammad Mozammil Akhtar, for their collaboration and contributions. Their guidance and camaraderie as close friends and fellow researchers at the PEARL lab have been invaluable. Lastly, special thanks are due to my mother Yong He and my father Shanbo Yin for their unwavering encouragement and understanding. Their love and support have sustained me during challenging times.

TABLE OF CONTENTS

Abst	tract	•••••		iii
Abst	trak			iv
Ack	nowledg	gments		v
Tabl	e of Co	ntents		vi
List	of Figu	res		xi
List	of Table	es		xiii
List	of Sym	bols and A	bbreviations	xiv
CHA	APTER	1: INTRO	ODUCTION	1
1.1	Resea	rch Backgı	ound	1
1.2			ent	
1.3			ives	
1.4			dology	
1.5				
1.0	THOSE			,
CHA	APTER	2: LITE	RATURE REVIEW	8
2.1	Introd	uction		8
2.2			ng for EVs	
	2.2.1		EV charging methods	
	2.2.2		EV wireless charging technologies	
			Inductive WPT	
			Capacitive WPT	
			Magnetic resonance WPT	
			Microwave or radio frequency WPT	
		2.2.2.5	Laser WPT	

		2.2.2.6 Magnetic gear and acoustic WPT	15
		2.2.2.7 Comparison between different WPT technologies	15
2.3	Basic	EV-IWPT System	16
2.4	Differ	ent Types of EV-IWPT Charging	17
	2.4.1	Stationary inductive wireless charging	17
	2.4.2	Quasi-dynamic inductive wireless charging	18
	2.4.3	Dynamic inductive wireless charging	18
	2.4.4	Comparison between different EV IWPT charging methods	18
2.5	The D	OIWC History and Development	19
	2.5.1	The early WPT history	19
	2.5.2	The implementation of EV DIWC technology	20
2.6	Analy	sis of the DIWC System	22
	2.6.1	Static model analysis of DIWC system	22
	2.6.2	Coil design parameters	22
		2.6.2.1 Magnetic flux density B	22
		2.6.2.2 Self-inductance L , Mutual inductance M , and Co	upling
		coefficient k	23
		2.6.2.3 Induced voltage U_L	24
	2.6.3	Power losses analysis	25
		2.6.3.1 Rectifier loss <i>P</i> _{Rectifer}	25
		2.6.3.2 Inverter loss <i>P</i> _{Inverter}	25
		2.6.3.3 Power loss of coils and compensated components	26
	2.6.4	Stationary model analysis of the DIWC system	27
2.7	Basic	Compensated Configurations	28
	2.7.1	SS configuration	28
	2.7.2	SP configuration	29

	2.7.3	PS configuration	.31
	2.7.4	PP configuration	.32
	2.7.5	LCC-S topology	.32
2.8	Magne	etic Coupler	.34
	2.8.1	Basic coil structures	.35
		2.8.1.1 Circular coil	.35
		2.8.1.2 Flux pipe	.36
		2.8.1.3 Rectangular coil	.37
		2.8.1.4 DD coil	.38
		2.8.1.5 DDQ coil	.39
		2.8.1.6 Bipolar coil	.39
		2.8.1.7 Other coils	.40
	2.8.2	Categories of single DIWC Tx coil	.42
		2.8.2.1 Long track	.42
		2.8.2.2 Lumped track	.44
	2.8.3	Typical methods of reducing mutual inductance fluctuations in DIV	WC
		system	.44
	2.8.4	Findings of the gap	.45
2.9	Summ	ary	.46
CHA	APTER	3: RESEARCH METHODOLOGY	.47
3.1	Introd	uction	.47
3.2	Design	n Procedures of the Proposed DIWC Magnetic Coupler	.47
3.3	Primai	ry Parameter Settings	.49
	3.3.1	Coil parameters	.50
	3.3.2	Circuit parameters	.50

3.4	Analysis	s of Conventional and Proposed DIWC Magnetic Couplers with Sin	gle Tx
	Coils.		51
3.5	Analysi	s of the Proposed DIWC Magnetic Coupler with Three Segment	ted Tx
	Coils.		56
	3.5.1	Transmitter design with its decoupling method	57
	3.5.2	Receiver design	58
3.6	Analysis	s of the DIWC System with the Proposed DIWC Magnetic Coupler	59
	3.6.1	The DIWC system configuration	59
	3.6.2	Circuit modeling	61
3.7	Experim	nental Prototype	64
	3.7.1	Magnetic coupler	64
	3.7.2	Circuit design	64
3.8	Summar	'y	66
СН	APTER	4: RESULTS AND DISCUSSIONS	67
4.1	Introd	uction	67
4.2	Simul	ated Result	67
	4.2.1	Mutual inductance between adjacent Tx coils M_{T1T2}	67
	4.2.2	Mutual inductance between activated Tx coils and Rx M_{3TR}	68
		4.2.2.1 M_{3TR} in Y direction	68
		4.2.2.2 M_{3TR} with different crossed ratio z	69
		4.2.2.3 M_{3TR} in X direction	70
	4.2.3	The selection of the control method for segmented Tx coils	70
	4.2.4	Rx coil turns N_r and coil length L_{rl} optimization	72
4.3	Experi	imental Results	
	4.3.1	Load R_L and efficiency η	

	4.3.2 Output voltage U_o and efficiency η in Y direction (x =0cm)	.74
4.3.3	Output voltage U_o and efficiency η in Y direction at different X-direction position	ons
	$(x=\pm 4\text{cm}, \pm 10\text{cm})$.76
4.4	Comparison with Other Existing DIWC Magnetic Couplers	.77
4.5	Summary	.78
CHA	APTER 5: CONCLUSION	.79
5.1	Conclusion	.79
5.2	Limitations of the Research	.80
5.3	Future Works	.80
Refe	rences	.82

LIST OF FIGURES

Figure 1.1: Flow chart of research methodology	6
Figure 2.1: Flow chart of WPT technologies	9
Figure 2.2: Equivalent circuit of IWPT (X. Lu et al., 2016; Zhang et al., 2022)	.11
Figure 2.3: Typical diagram for CWPT with compensation networks (Triviño-Cabrera	a et
al., 2020)	.11
Figure 2.4: Generic diagram for MR-WPT system with compensation networks (Kurs	s et
al., 2007)	.13
Figure 2.5: Generic diagram of a MWPT system (Triviño-Cabrera et al., 2020)	. 14
Figure 2.6: Generic diagram of a laser WPT system (Triviño-Cabrera, A. et al, 2020).	. 15
Figure 2.7: General diagram of EV-IWPT System (Siqi & Mi, 2015)	. 17
Figure 2.8: Two-coupled coils model with leakage inductances	.22
Figure 2.9: Equivalent circuit of coupled coils	. 24
Figure 2.10: SS configuration	.28
Figure 2.11: SP configuration	.30
Figure 2.12: PS configuration	.31
Figure 2.13: PP configuration	.32
Figure 2.14: LCC-S topology	
Figure 2.15: Exploded view of general magnetic coupler (Ahmad et al., 2018)	.34
Figure 2.16: Circular coil and its flux distribution (Patil et al., 2017)	.36
Figure 2.17: Flux pipe (Patil et al., 2018)	.37
Figure 2.18: Rectangular coil (Ahmad et al., 2018)	
Figure 2.19: DD coil (Ahmad et al., 2018).	
Figure 2.20: DDQ coil (Ahmad et al., 2018).	.39
Figure 2.21: Bipolar coil (Ahmad et al., 2018).	.40
Figure 2.22: (I) Tripolar coil; (II) Three coil; (III) Four coil; (IV) Crossed DD o	coil
(Mohamed et al., 2020; Patil et al., 2018)	.42
Figure 2.23: Tx coil in DIWC system (I) long track; (II) segmented track (Li et al., 201	
	.42
Figure 2.24: Six generation OLEV's magnetic coupler (Cui et al., 2022)	.43
Figure 3.1: Flow chart of designing the proposed DIWC magnetic coupler	.49
Figure 3.2: Conventional and proposed DIWC magnetic couplers (I) The crossed but no	on-
overlapped DD Tx coil with non-crossed and non-overlapped DD Rx coil; (II) no	on-
crossed and non-overlapped DD Tx and Rx coils; (III) non-crossed but overlapped Tx a	and
Rx coils; (IV) non-crossed but overlapped Tx coil and non-crossed and non-overlapped	ped
Rx coil; (V) Cross-overlapped Tx coil and non-crossed and non-overlapped Rx coil	.55
Figure 3.3: Comparison of five types of DIWC magnetic coupler (Figure 3.3 (I)-(V))
misalignment performance (I) Along the X-direction; (II) Along the Y-direction	.56
Figure 3.4: The structure of proposed DIWC magnetic couplers	
Figure 3.5: (I) Coupling model of the proposed decoupling method	
Figure 3.6: When Rx length l_r =42cm, side view of activated T1, T2, and T3 coils	
Figure 3.7: Configuration of the proposed DIWC system	
Figure 3.8: AC equivalent circuit with resistances	
Figure 3.9: Proposed Tx structure	

Figure 3.10): Experimental Pr	ototype		03
Figure 4.1:	The M_{3TR} variat	ion curve when crossed	I ratio $z = (1/3) \%;$	69
Figure 4.2:	M_{3TR} variation c	urves with different cro	ssed ratio z;	69
Figure 4.3	M_{3TR} variation alo	ng the X direction (whe	en Rx positioned at y	=0cm)70
Figure 4.4:	: Timing of swite	ching action with chan	ged Rx position at	Y direction (R
length $l_{rl}=4$	2cm)		•••••	7
Figure 4.5:	The M_{3TR} variatio	n with changed Rx Y-d	irection position and	l different value
	=	en <i>N_r</i> =16);		
		tour map of coupling of		
-	_	tween load resistance I	•	
Figure 1 8:	II I and II way	eforms and power anal	vzer images at differ	ent Ry position
•	* ' * '	. (II) $y=18$ cm. (III) $y=3$ 0	•	•
		output voltage along Y		
-	=			
_		iciency and output vol ±10cm)		
_				
_				
_	ositions (x=±4cm,			
_	ositions (x=±4cm,			
_	ositions (x=±4cm,			
_	ositions (x=±4cm,			

LIST OF TABLES

Table 2.1: Comparison among different WPT techniques	16
Table 2.2 Comparison between different EV IWPT charging methods	18
Table 2.3: Different EV IWPT projects	21
Table 2.4: Comparison of different coil structures	41
Table 2.5: Comparison of six generation OLEV's long track structure	43
Table 2.6: Characteristics of lumped track and long track	44
Table 2.7: Recent research on reducing mutual inductance fluctuations throu	gh DIWC
magnetic coupler design.	45
Table 2.8:Comparison of existing designs with the main purposes of	achieving
decoupling, reduced mutual inductance fluctuations and optimized efficiency	46
Table 3.1: The key parameters of the proposed magnetic coupler	50
Table 3.2: The primary circuit parameters setting	51
Table 3.3: Experimental Prototype Parameters	65
Table 4.1: Simulation values of the mutual inductances between adjacent Tx s	
coils (when N_{t3} =4)	68
Table 4.2: Comparison with other DIWC magnetic couplers	77

LIST OF SYMBOLS AND ABBREVIATIONS

AC : Alternating current

AWG : American wire gauge

AWPT : Acoustic WPT

C : Resonant capacitor

CC : Constant current

CO₂ : Carbon dioxide

CV : Constant voltage

CWPT : Capacitive wireless power transfer

DC : Direct current

DD : Bipolar

DIWC : Dynamic inductive wireless charging

DWC : Dynamic wireless charging

EMF : Electromotive force

EV : Electric vehicle

EVs : Electric vehicles

FEA : Finite element analysis

FHA : Fundamental harmonic analysis

CWPT : Capacitive WPT

IWPT : Inductive WPT

KAIST : Korea advanced institute of science and technology

KCL : Kirchhoff's current law

KVL : Kirchhoff's voltage law

L : Self-inductance

LBNL : Lawrence berkeley national laboratory

LCC : Inductor-capacitor-capacitor

LCL : Inductor - capacitor - Inductor

MGWPT : Magnetic gear WPT

MIT : Massachusetts institute of technology

MIMO Magnetic multiple-input multiple-output

MOSFET : Metal oxide silicon field effect transistor

MRCWPT : Magnetic resonance coupled WPT

MRMT : Multiple Rx and Tx coil

MROT : Multiple Rx and one Tx coil

MRWPT : Magnetic resonant WPT

MWPT : Microwave wireless power transfer

OLEV : On-line EV

ORMT : One Rx and multiple Tx coil

ORNL : Oak ridge national laboratory

OROT : One Rx and Tx coil

PATH : Partners for advanced transit and highway

PM : permanent magnet

PP : Parallel-Parallel

PS : Parallel-Series

PWM : Pulse width modulation

Q : Unipolar

QDWC : Quasi-dynamic wireless charging

RC : Rectangular coil

RF : Radio frequency

RFID : Radio frequency identification

RMS : Root of mean square

RPEV : Road powered EV

Rx : Receiver

SBEB : Santa barbara electric bus

SP : Series-Parallel

SPS : Series-Series

SWC : Static wireless charging

TP : Tripolar pad

Tx : Transmitter

UOA : University of Auckland

ZPA : Zero phase angle

ZVS : Zero Voltage Switching

CHAPTER 1: INTRODUCTION

1.1 Research Background

Global climate change and the depletion of fossil fuels have driven significant changes in the power and transportation sectors. The sector of transport, as a major source of substantial energy consumption and carbon emissions, contributes to over one-fifth of the total global carbon dioxide (CO₂) emissions (Li & Loo, 2014). The majority of these emissions stem from the consumption of fossil fuels in road transportation (Cardama et al., 2023). To address this increasingly severe challenge, electric vehicles (EVs), invented earlier than traditional fuel vehicles by American Thomas Davcnport in 1834, are rapidly emerging as a green and sustainable transportation option. Using batteries and electric motors instead of internal combustion engines in traditional vehicles significantly lowers carbon emissions and reduces reliance on fossil fuels (Covic & Boys, 2013). Nevertheless, the widespread adoption of electric vehicles brings forth many challenges concerning electric vehicle (EV) charging issues. Currently, wired charging is the predominant method used to recharge EV batteries, requiring a physical link between the electrical power source and EVs. Whether at home or in public spaces, implementing wired EV charging necessitates the development of robust charging platforms and infrastructure, which can incur substantial construction costs. Furthermore, the extended time required to charge EV batteries also remains a significant constraint on the widespread adoption of EVs (Solvi Hoen et al., 2023). The simultaneous charging with a large number of EVs also imposes a significant burden on the power grid (Neaimeh et al., 2015). Additionally, frequent plugging and unplugging of the charging cable can cause wear and tear, reducing its lifespan and posing a safety risk due to exposed wires. Adverse weather conditions, such as heavy rain, also increase the risk to the operator's safety when handling charging cables. Hence, identifying the appropriate energy transfer method is a critical technical challenge for EV applications. Wireless power transfer (WPT) technologies, enabling

wireless vehicle charging, are effective solutions and have gained significant attention from the scientific community.

Current WPT methods, based on the car's motion during charging, include Stationary Wireless Charging (SWC), Quasi-dynamic Wireless Charging (QDWC), and Dynamic Wireless Charging (DWC). (Ahmad et al., 2018). DWC technology enables EVs to charge while on the move (Mohamed et al., 2022). As the EV moves, it continuously receives wireless power from transmitter (Tx) coils, eliminating the necessity for stationary charging stations. DWC technology finds applications across various industrial and domestic settings, proving particularly advantageous for EVs. Compared to SWC and QDWC technologies, DWC significantly alleviates driving range anxiety and reduces charging times by skipping the need to stop at fixed charging stations. Although DWC technology requires a large amount of cost to install a track, the cost of manufacturing batteries can be saved at the same time, which has verified its potential for widespread application in previous research (Ahmad et al., 2018).

Inductive Power Transfer (IPT) technologies of EVs, as one of the WPT technologies, performs better performance in most current EV applications regarding its noiselessness, galvanic isolation, better misalignment tolerance in a large range, and can achieve high power across a relatively large air gap (10–40 cm) (Mohamed & Mohammed, 2018). This range suits the installation requirements of most vehicles (X. Lu et al., 2016). In IPT systems, the coupler is essential for converting electrical energy into magnetic energy and vice versa, facilitating efficient energy transfer across an air gap. This component typically includes a Tx coil or cable line connected to a power source, which is embedded beneath the road, and the Rx coil receives the transferred energy wirelessly and is installed under the vehicle body (Siqi & Mi, 2015). Effective coil design is crucial, as suboptimal design can hinder wireless power transfer (Boys & Covic, 2014). To boost the performance dynamics of the EV-DWC system, optimizing coil design to maximize

output power and improve energy transfer efficiency is essential.

The longitudinal dimensional configuration of the DWC coupler is categorized into long-track and lumped-track coil types (Ahmad et al., 2018; Buja et al., 2016). Among them, the long-track Tx coil type has a length longer than that of the Rx coil. As EVs pass over these track coils, continuous power supply is ensured without the need for switching control (Li et al., 2019). Its simple circuit structure is advantageous, but this type typically exhibits lower efficiency. On the other hand, the lumped track consists of Tx coils, similar in size to the Rx coil, embedded under the road surface, and powered independently (Choi et al., 2013). This design achieves higher efficiency and lower magnetic leakage than the long-track structure, with a suitable coupling coefficient to power multiple EVs concurrently.

1.2 Problem Statement

Mutual inductance, as an electromagnetism parameter, is essential during the design process of the DIWC magnetic coupler. The stability of the mutual inductance between Tx and Rx is proportionally related to the performance of the output voltage or power during EVs moving. In contrast, the mutual inductance between Tx coils may have an adverse impact on the whole system's transfer efficiency. Placing segmented coils spaced apart serves the dual purpose of mitigating cross-coupling between adjacent coils and saving coil material cost, but the output power or voltage will drop even to zero as the Rx coil moves further from the Tx coils (Li et al., 2019; Liu et al., 2022). Not only does this circumstance negatively affect the battery longevity, but it also impacts charging performance, especially in high-speed EV applications (Li et al., 2019). Decreasing the gap between adjacent Tx coils or bringing them closer to each other can be effective (Wang et al., 2018; Zhou et al., 2024). However, the inevitable cross-coupling phenomenon that occurs on the same side of Tx coils will be strengthened simultaneously. Furthermore, it has been demonstrated that the multi-coil configuration improves the

magnetic field coupling, enabling enhancing the magnetic field coupling between Tx and Rx, thereby delivering more energy to the battery (Hossain et al., 2022). However, it also simultaneously increases the undesirable cross-coupling with adjacent multiple coils placed side by side. Therefore, there is a significant challenge associated with the realization of decoupling, improved efficiency, and reduced mutual inductance fluctuation.

Although numerous studies have been conducted, none can achieve all three objectives concurrently. Existing research on magnetic coupler design can be divided into several approaches: optimizing the coil turns (Li et al., 2019), size (Hossain et al., 2022), winding method (Darvish et al., 2023; Zhou et al., 2024), and distance between adjacent Tx coils (Liu et al., 2022; F. Lu et al., 2016), combining different coil structures (Li et al., 2019) or coil arrangement including overlapping and crossing techniques (Cai et al., 2022; Liu et al., 2017; Wang et al., 2018; Xiang et al., 2018). Yong Li et al. proposed a DIWC system addressing cross-coupling between adjacent Tx coils. The magnetic flux generated by bipolar (DD) coils is in two opposite directions, which can naturally realize decoupling with unipolar (Q) coils (Li et al., 2019). However, an overlapped Rx with a DD and a Q coil is required to continuously obtain stable power from Tx, resulting in underutilization of the Rx coils and increased coil construction costs. X. Li et al. (2020) utilize specific sizing of both DD and Q coils to eliminate cross-coupling between adjacent segmented Tx coils. Additionally, the DD coil achieves natural decoupling with the Q Tx coils, but also with the Q Rx coil. Consequently, the Tx DD coil is unable to participate in the energy transfer. In summary, there is a need for achieving decoupling between adjacent segmented Tx coils, reduced mutual inductance fluctuation and enhanced transfer efficiency at the same time.

1.3 Research Objectives

This research mainly aims to propose a new DIWC magnetic coupler with multiple purposes, including achieving decoupling between adjacent Tx coils, improved efficiency, and reduced output pulsation during the dynamic charging process. The study has following objectives as below.

- (I) To analyze the characteristics of existing coil structures, aiming to achieve decoupling between adjacent Tx coils, improve efficiency, and reduce output power pulsation in the DIWC system.
- (II) To optimize and validate the proposed Tx coil structure through finite element analysis (FEA) simulations and experimental implementation.
- (III) To compare the performance of the newly proposed Tx coil with other typical coil structures.

1.4 Research Methodology

First, review related literature and summarize several types of existing coil structures used in DIWC systems, comparing their characteristics. Next, based on established criteria and practical considerations, set the desired mutual inductance value between the Tx and Rx coils along with its desired fluctuation under dynamic conditions, and determine the constants and variables of the Tx and Rx coils for the proposed DIWC magnetic coupler. Then, build the corresponding coil simulation model and optimize coil parameters by ANSYS Maxwell. The optimized parameters include determining coil width, number of turns, coil length, and coil arrangement, with the goal of minimizing mutual inductance between the Tx and Rx coils and eliminating cross-coupling between adjacent Tx coils. Afterward, construct a lab prototype to validate the performance of the proposed structure. Collect and compare the power-on test results of the proposed structure with those of existing structures. Finally, compile the entire study and findings

into a report for submission. The overall research methodology is summarized in the flowchart shown in Figure 1.1.

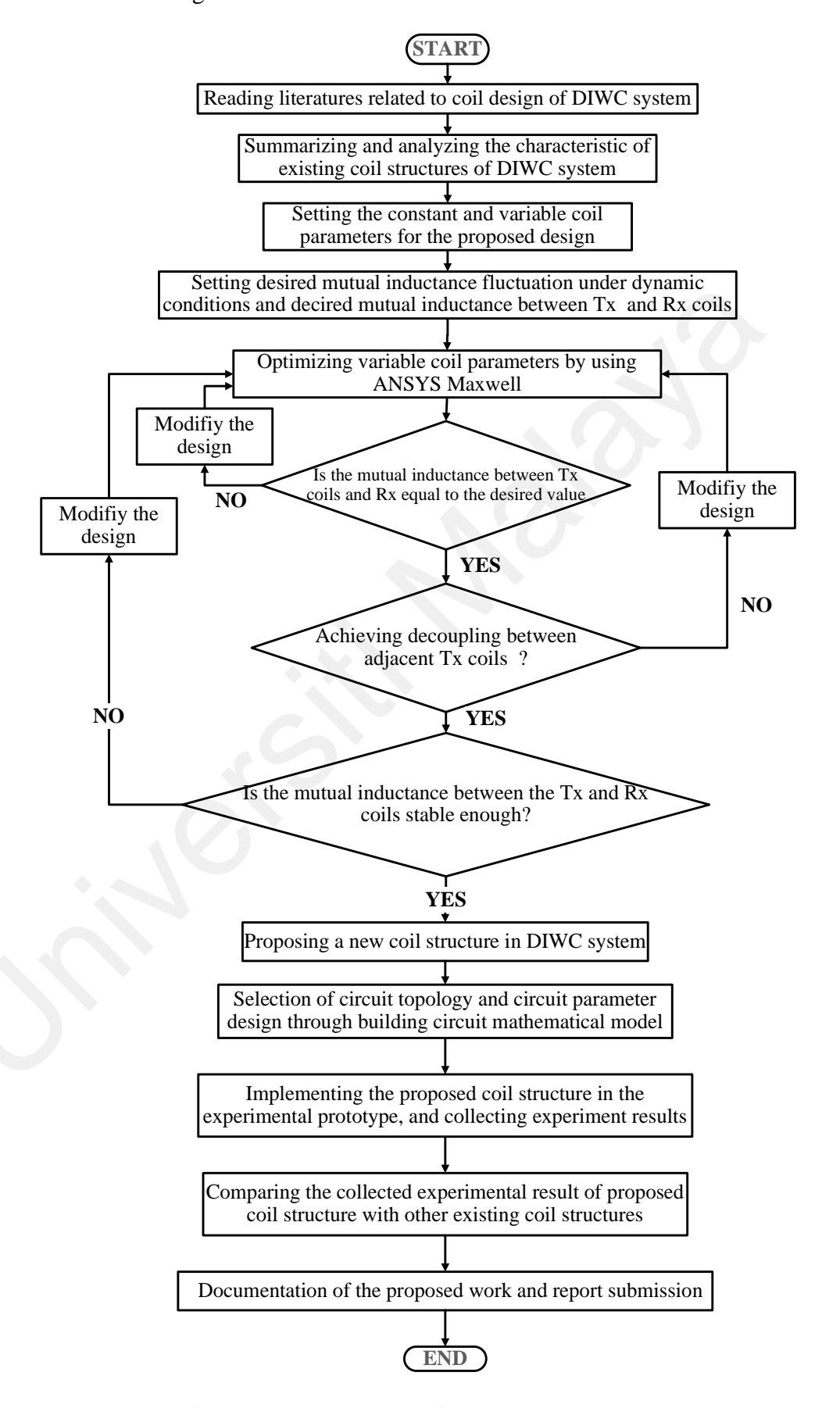


Figure 1.1: Flow chart of research methodology

1.5 Thesis Outline

This study proposes a new cross-overlapped decoupling structure for the EV-DIWC system. The proposed structure mainly aims to achieve decoupling between adjacent Tx coils and simultaneously reduce power fluctuation and high energy transfer efficiency. This thesis is organized into five chapters:

Chapter 1 provides a brief introduction to the thesis. It addresses the following questions: why this thesis is being conducted, what the thesis entails, and how the thesis will be conducted, which is outlined in the following sections: research background, problem statement and objectives, and research methodology.

Chapter 2 presents a detailed literature review of the DWPT system. The early development history of WPT technologies is provided first. After that, analysis and comparison among various types of WPT techniques, typical basic coil structures, and compensation topologies are introduced. In addition to this, the chapter gives a simple circuit analysis of a dynamic charging system. Moreover, two types of DWPT magnetic couplers are classified by Tx length, named long and lumped track, along with various solutions for circuit design of DWC systems and reducing output power pulsation in DIWC systems.

Chapter 3 details the research methodology of the proposed DIWC magnetic coupler, compares it with other coil structures, and evaluates the system using fundamental harmonic analysis (FHA). It also explains the implementation of the DIWC system.

Chapter 4 details the simulated result and experimental and based on the prototype of the proposed DIWC system featuring the newly proposed magnetic coupler. Explanations are provided for each set of experimental data. Additionally, a comparison between the experimental data of the proposed structure and existing structures is included.

Chapter 5 concludes by summarizing the key contributions of the research and exploring limitations and potential future directions for further work.

CHAPTER 2: LITERATURE REVIEW

2.1 Introduction

This chapter offers an in-depth review of EV-DIWC systems. It starts with a brief introduction to various EV charging methods, emphasizing the advantages of wireless charging. It then presents and compares different WPT technologies based on their classifications. The emphasis is on Inductive Power Transfer (IPT) technology, examining fundamental compensated topologies and coil designs used in DIWC systems through comparative analysis. Additionally, the chapter covers analysis of typical circuit topology design used in DIWC system.

2.2 Wireless charging for EVs

EV Wireless charging refers to charging EVs wirelessly. This section briefly covers three types of charging methods and then introduces various wireless charging technologies with a focus on inductive WPT, which is widely used in EVs.

2.2.1 Different EV charging methods

Due to limitations in the energy density of EV batteries, the size of batteries installed in vehicles restricts the amount of energy that can be stored, necessitating periodic recharging. Currently, there are three primary methods for charging EV batteries: wired charging, wireless charging, and battery replacement (Yilmaz & Krein, 2013). Wired charging remains the predominant method due to its high performance in energy transfer, despite requiring unavoidable construction and maintenance costs for charging facilities, and an increased risk of electrical safety incidents involving human contact (Mi et al., 2016). Battery replacement entails swapping out depleted batteries for fully charged ones at designated stations. This method offers a safer and faster-charging alternative for EVs but entails substantial costs for constructing and maintaining replacement stations equipped to store numerous batteries securely (Wang & Dorrell, 2013). Moreover, to accommodate varying charging standards and spatial dimensions for storing EV batteries,

it is necessary to stock batteries of diverse specifications in advance, further raising costs (Wang & Dorrell, 2013). Wireless charging, enabling transfer power without physical connections, is deemed safer than wired methods. Moreover, it avoids port damage caused by frequent plugging and unplugging, extending the device's lifespan. Wireless charging is increasingly gaining attention in the EV industry, positioning itself as a significant and transformative trend in the future of EV development.

2.2.2 Different EV wireless charging technologies

Wireless charging is based on WPT technologies. In this section, the range of WPT technologies are explored, as shown in Figure 2.1, categorized by their transmission distances. In addition, according to the different principles of energy transmission in a contactless state, WPT technologies are broadly categorized into non-radiative coupling-based and radiative waved-based WPT (X. Lu et al., 2016). In the radiative WPT, power is transmitted through electromagnetic waves in the Hz to THz frequency range, encompassing methods such as laser WPT (LWPT) (Kapranov et al., 2017), microwave WPT (MWPT) (Matsumoto, 2002; Shinohara et al., 2013), radio-frequency (RF) WPT (Shinohara, 2010), magnetic gear WPT and acoustic WPT. Non-radiative coupled-based WPT encompasses three primary technologies: inductive WPT (IWPT) (Liu et al., 2017), magnetic resonant WPT (MRWPT) (Kurs et al., 2007) and capacitive WPT (CWPT) (Ludois et al., 2012).

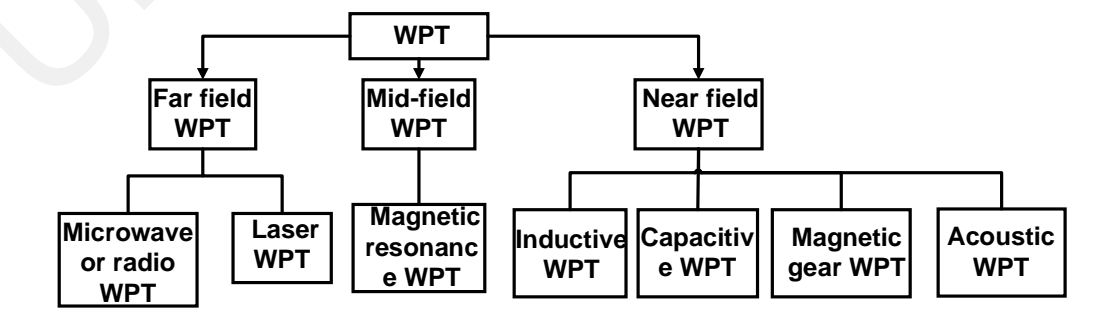


Figure 2.1: Flow chart of WPT technologies

2.2.2.1 Inductive WPT

IWPT is a near-field, non-radiative technology based on electromagnetic induction, as shown in Figure 2.2. This method supplies an alternating current of a specific frequency to the primary coil L_1 , generating a fluctuating magnetic field through magnetic coupling. This magnetic field is then captured by the secondary coil L_2 , which induces a voltage and allows for efficient high-power transfer across relatively short distances (10 to 40 cm) between the Tx and Rx coils (Macharia, 2017).

This process is governed by Faraday's law and Ampère's law. Ampère's law asserts that a varying electric field generates a corresponding magnetic field. When the system's frequency remains constant, the magnetic field's magnitude variations are linked to the current flowing through the wire, as the equation represents. The variable gauges the capacity of a magnetic field source to generate a magnetic field, indicating the concentration of magnetic field lines per unit length.

$$\oint \overline{H}dl = I \tag{2.1}$$

Faraday's law states that variations in magnetic flux through a closed loop induce an electromotive force (EMF) in the circuit. When the circuit is closed, this EMF results in an electric current. In the equation (2.2), ϕ denotes the magnetic flux passing through the area of the coil. A current is induced on the opposite side of the coil by an alternating magnetic field generated on one side. Consequently, the secondary coil must be precisely tuned to the operating frequency, a task that can often be difficult. As a result, the effective charging distance of EV is typically restricted within 20cm (Lu et al., 2015). Commercial applications of IWPT include technologies like passive radio frequency identification (RFID), which get power from readers through IWPT technology. Another notable example is magnetic multiple-input multiple-output (MIMO), an advanced system developed by researchers at MIT (Ahson & Ilyas, 2017; Jadidian & Katabi, 2014).

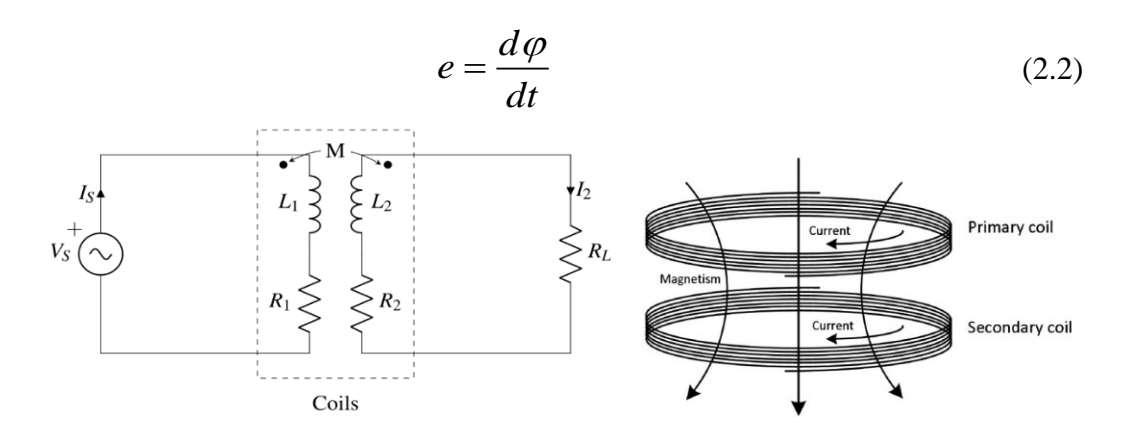


Figure 2.2: Equivalent circuit of IWPT (X. Lu et al., 2016; Zhang et al., 2022)

2.2.2.2 Capacitive WPT

CWPT is a form of near-field and non-radiative WPT that distinguishes itself from other methods by utilizing electric fields instead of magnetic fields. Figure 2.3 shows that CWPT uses two metal plates as electrodes—one on the Tx side and one on the Rx side—to transfer energy through a high-frequency electric field. The plates act as coupled capacitors, with the space between them as the dielectric (Kline et al., 2011). CWPT does not produce leakage magnetic fields and allows for effective electric field control between the Tx and Rx. Without significantly affecting system efficiency, power can also be transferred in the presence of metallic objects. However, achieving high levels of energy transfer requires very high electric field intensities, which limits its application to lower power levels (Regensburger et al., 2018). Additionally, CWPT technology can pose risks of high voltage electric shock and produce harmful ozone (Erel et al., 2021).

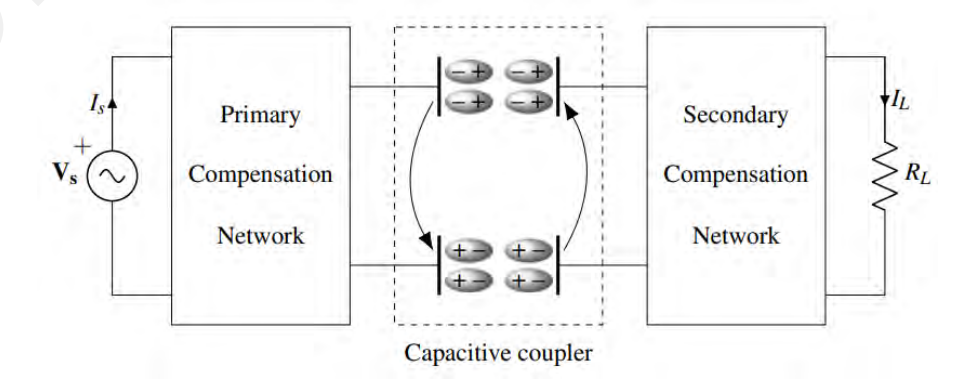


Figure 2.3: Typical diagram for CWPT with compensation networks (Triviño-Cabrera et al., 2020)

2.2.2.3 Magnetic resonance WPT

In comparison to inductive WPT, MRWPT, as depicted in Figure 2.4, operates as a near-field, non-radiative technology. Within the "strong-coupled" regime of coupledmode theory (Triviño-Cabrera et al., 2020), MRWPT can deliver the same amount of power over longer distances with less intense magnetic fields while maintaining relatively high efficiency. This is because it relies on evanescent wave coupling, transferring electrical energy between two resonant coils through oscillating magnetic fields. When both coils are adjusted to the same resonant frequency using a compensation network, they achieve strong coupling, leading to high energy transfer efficiency and minimal leakage to non-resonant environments. Moreover, operating within the megahertz frequency range, magnetic resonance WPT typically has high-quality factors. As the charging distance grows, these high-quality factors help to counteract the significant reduction in coupling efficiency, thus improving the overall effectiveness of the charging process. In this context, "Mid-field" refers to distances up to 4–10 times the coil diameter (Karalis et al., 2008). Magnetic resonance can effectively transfer energy using resonant coils smaller than the wavelength, whereas magnetic induction relies on coils comparable in size to the wavelength. As a result, magnetic resonance is ideal for mid-field energy transfer applications, while magnetic induction is limited to shorter distances.

The WiTricity technology, invented and proposed by MIT researchers, enables lighting a 60W bulb with a transmission distance of more than 2km (Kurs et al., 2007). However, its reliance on a distributed capacitive coil for operation presents a significant obstacle to shrinking the size of a WiTricity Rx and mounting such a big coil on EVs or portable electronic devices. Furthermore, the efficiency of MRWPT technology, when it is in the same case as inductive WPT, is generally lower than that of magnetic induction, which limits its widespread adoption (Karalis et al., 2008; Triviño-Cabrera & Sánchez, 2018).

Additionally, achieving high efficiency in MRWPT often requires coils with high self-inductance, which increases the system's weight (Prengel, Helwig, & Modler, 2014).

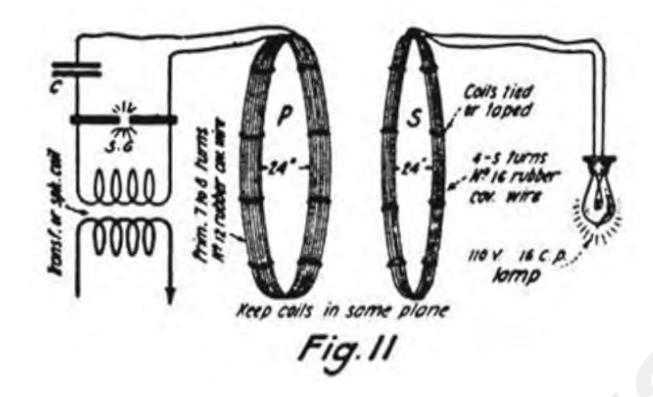


Figure 2.4: Generic diagram for MR-WPT system with compensation networks (Kurs et al., 2007)

2.2.2.4 Microwave or radio frequency WPT

MWPT or RF WPT are technologies that enable the transmission of electrical energy over long distances using electromagnetic waves, which are radiative WPT techniques and classified into wave-based WPT. MWPT involves using microwave frequencies to transfer energy by constantly interacting on both sides. This method is effective over substantial distances in the far-field range, where energy is concentrated and directed through antennas. MWPT is often considered for applications requiring high power levels, such as satellite-based solar power systems or long-distance power beaming. RF power transfer operates on similar principles but uses lower frequencies than microwaves. RF-WPT is typically used for shorter distances and lower power applications, such as powering small electronic devices or sensors. Both methods leverage the ability to convert electrical energy into electromagnetic waves, which are transmitted through space and converted back into electrical energy by receiving antennas.

A typical WPT system transmitting power by microwave is illustrated in Figure 2.5. A high-voltage DC generator powers a magnetron, which generates a microwave signal. After traveling through space at light speed, the radio or microwave is captured by the receiver rectenna and then converted to electricity through RF-to-DC conversion. During

the full process of energy transfer, the accuracy of impedance matching between the antenna and the voltage multiplier and the power density, captured by the receiving antenna, is unavoidable to affect system performance directly (Kapranov et al., 2017; Ladan et al., 2013; Shinohara et al., 2013).

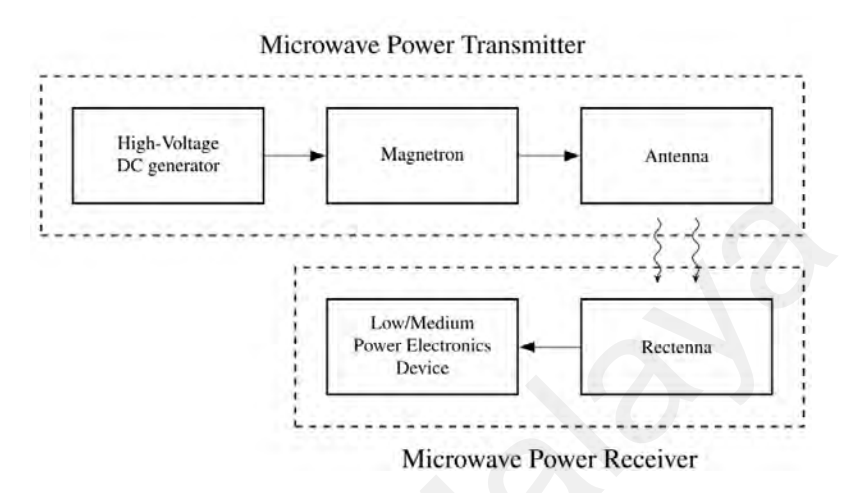


Figure 2.5: Generic diagram of a MWPT system (Triviño-Cabrera et al., 2020)
2.2.2.5 Laser WPT

As depicted in Figure 2.6, Laser WPT technology permits using electromagnetic waves in the THz frequency range for power transfer. This process is accomplished by transforming electrical current into a laser beam using high-power laser diodes or solid-state lasers. These lasers provide precise directionality and high energy density, enabling efficient and accurate long-distance energy transmission. Subsequently, the laser light is captured on the Rx side and converted back into electrical power by a photoelectric Rx or photovoltaic cell. The system also features a DC-DC converter and regulation circuit to provide stable and suitable power output (Jin & Zhou, 2018).

This type necessitates that the Tx and Rx remain relatively close, as obstacles can obstruct the energy transmission. When these conditions are satisfied, the distance can be further extended. The high directivity of laser WPT is beneficial, as it reduces interference with other systems. However, transmitting energy via laser beams comes with significant safety risks for human boday, including blindness, burns, and potentially fatal injuries. Furthermore, the current system efficiency is restricted to approximately 25% (Jin &

Zhou, 2018). This limits its practical applications. At present, laser WPT is particularly unsuitable for charging EVs, especially in DWC systems, because of the challenges in safety, designing stable and efficient charging devices. However, advancements in laser technology and photovoltaic cells may address these issues soon.

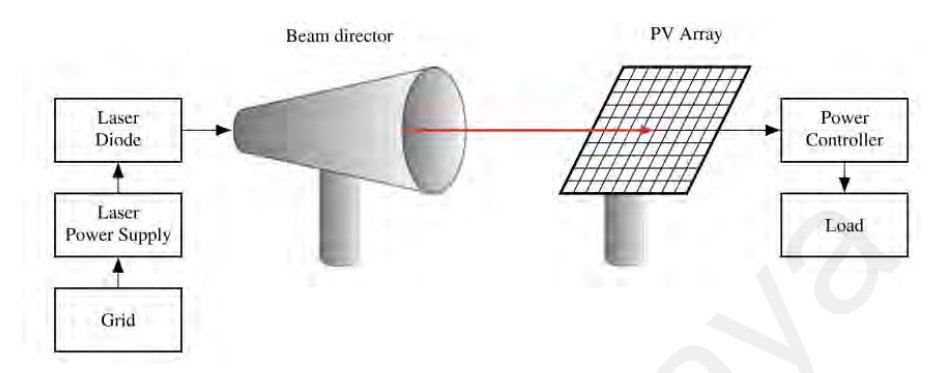


Figure 2.6: Generic diagram of a laser WPT system (Triviño-Cabrera, A. et al, 2020)

2.2.2.6 Magnetic gear and acoustic WPT

Transmitting power through magnetic or acoustic can also be seen as WPT technologies. In the magnetic gear WPT system, two synchronized permanent magnets are positioned side by side, substituting the coils, metal plates, or antennas typically used in other WPT technologies at the same positions. The mechanical torque generated by the primary power source applied to the transmitter winding causes the primary permanent magnet (PM) to rotate, thereby transferring torque to the secondary PM through mechanical interaction (Panchal et al., 2018). On the other hand, acoustic WPT typically employs ultrasonic waves, which are sound waves with frequencies exceeding the audible range, generally above 20 kHz (Tseng et al., 2017). Both of them suffer from limitations in power level or effective transferred distance, negative effects on the surrounding environment, human body risk, and so on.

2.2.2.7 Comparison between different WPT technologies

The following compares different WPT techniques as portrayed in Table 2.1.

Table 2.1: Comparison among different WPT techniques

WPT Technology	Frequency	Distance		Transmission Medium
Inductive	A few Hz to 1MHz	0 to 40cm	Near field	Magnetic field
Magnetic resonant	A few Hz to 1GHz	Below a few meters	Mid- field	Resonant magnetic field
Capacitive	Several MHz	A few centimeters	Near field	Electric field
Microwave	300 MHz -1Hz	A few meters	Far-field	Microwave
Laser	More than 1thz	A few kilometers	Far-field	Beam
Magnetic gear	150 to 300Hz	10-15cm	Near field	Mechanical force
Acoustic	0.5 to 3 MHz	70-30cm	Near field	Ultrasonic waves

2.3 Basic EV-IWPT System

A typical EV-DIWC system features both primary and secondary sides, as illustrated in Figure 2.7 (Siqi & Mi, 2015). The primary side comprises an AC/DC power converter, a DC-AC inverter, a primary compensation circuit, Tx coils for IWPT or Tx metal plates for CWPT. The AC-DC converter changes single-phase or three-phase AC from the grid into stable DC, which is then converted to high-frequency AC (typically 80-90 kHz) by the inverter, as specified by SAE J2954 standard (X. Lu et al., 2016). The high-frequency inverter should operate in soft-switching mode, ensuring that the voltage or current through each switch is nearly zero during switching events. This approach minimizes switching losses and enhances power transfer to the secondary side. Achieving this requires employing a network of capacitors and inductors on both the primary and secondary sides. Various common compensated topologies have been proposed and analyzed. The secondary side typically includes a secondary compensation network, an Rx coil (for IWPT technology) or a metal plate (for CWPT technology), a rectifier, and a load. The coils or metal plates on both sides are designed to receive power from the primary side. The rectifier transforms the induced AC voltage into DC voltage to power

the load. Furthermore, in IWPT system, ferrite and aluminum or metal plates are used on both sides of the coils to reduce magnetic field leakage.

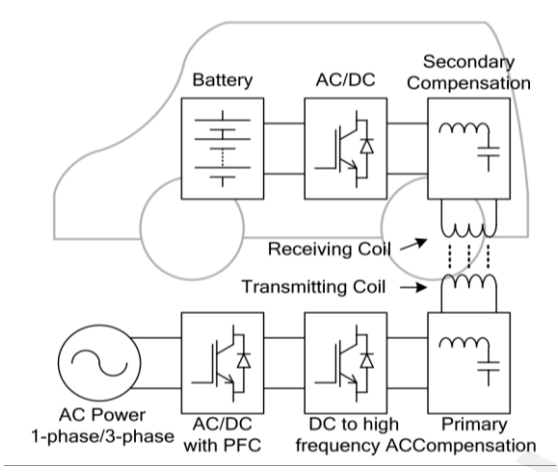


Figure 2.7: General diagram of EV-IWPT System (Siqi & Mi, 2015)

2.4 Different Types of EV IWPT Charging

According to the motion of EVs during wireless EV charging, IWPT technologies of EVs can be categorized into three types: Stationary inductive wireless charging (SIWC), Quasi-dynamic inductive wireless charging (QDIWC), and Dynamic inductive wireless charging (DIWC) (Ahmad et al., 2018).

2.4.1 Stationary inductive wireless charging

SIWC refers to charging electric vehicles (EVs) while parked for extended periods. Electrical energy is transmitted from the charging pad installed on the ground to EV batteries storied in vehicles via electromagnetic induction, rather than through wires. The key advantages of SIWC technology include minimizing wear and tear from frequent plugging and unplugging of charging connectors and reducing the risk of electric leakage during manual charging operations, especially under adverse weather conditions. However, this method requires a large amount of wireless charging infrastructures, leading to high investment in land, equipment and maintenance. Moreover, compared to wired charging, lower charging efficiency shows in SIWC system because of the current technological constraints. Furthermore, precise EV positioning is required to minimize the magnetic field loss generated between Tx and Rx.

2.4.2 Quasi-dynamic inductive wireless charging

QDIWC is a middle ground between SIWC and DIWC, commonly used at locations where EVs can charge for short durations, such as at traffic light intersections (Mohamed et al., 2017). In this system, Tx coils or cables are installed within the road surface, while Rx coils are installed on the vehicle. This setup facilitates charging during brief stops. However, QDIWC is designed for short charging periods, so it may not fully charge a vehicle unless it makes several stops.

2.4.3 Dynamic inductive wireless charging

DIWC refers to the technology of charging vehicles while they are continuously moving. With the widespread adoption of DIWC, the waiting time for vehicle charging is significantly reduced, and vehicles can operate with smaller batteries. This advancement could significantly boost the production and adoption of EVs, potentially lessening the dependency on major breakthroughs in battery technology, and aligning well with the current trends in EV development (Onar et al., 2013).

2.4.4 Comparison between different EV IWPT charging methods

Table 2.2 provides a comparison between SIWC, DIWC and QDIWC charging methods.

Table 2.2 Comparison between different EV IWPT charging methods

Criteria	SIWC	QDIWC	DIWC	
EV status	EV status Static		On the move	
Battery size affect	No affect	Less reduced	Reduced	
Driving Range anxiety	No reduced	Less reduced	Reduced	
Market	High	Low	Low	
acceptance	111611	Low	Low	
Construction cost	High	Low	High	
Needed power	Low	Middle	High	
converters	LOW	Wilduic	Iligii	
Need coil material	Low	Middle	High	
cost	LOW	Middle	High	
Application	Home garages,	Traffic lights at an	Urban roads,	
scenarios	charging stations	intersection, toll booths	parking lots	

2.5 The DIWC History and Development

2.5.1 The early WPT history

The development of DIWC technologies traces back to the early discoveries in electromagnetism. In 1819, Hans Christian Ørsted conducted a pivotal experiment using a simple setup that included a wire and a compass. Ørsted passed an electric current through the wire and positioned the current-carrying wire near the compass. He observed that the compass needle, which typically oriented north because of the Earth's magnetic field, was deflected from its usual position. This deflection indicated the additional magnetic field created around the wire by the electric current, thereby groundbreakingly revealing the fundamental link between electricity and magnetism. Ørsted's findings were instrumental in inspiring other scientists, like André-Marie Ampère, Michael Faraday, and Biot Savart, to explore and formalize the relationship between electricity and magnetism. In 1864, a British physicist and mathematician, named James Clerk Maxwell, introduced a set of equations referred to as Maxwell's equations. He later compiled his findings in a comprehensive treatise, titled "A Treatise on Electricity and Magnetism" (Maxwell, 1873). Those equations fundamentally help people how electric and magnetic fields interact and propagate, and they theoretically predict the existence of electromagnetic waves. Its predictions about electromagnetic waves were experimentally confirmed by Heinrich Hertz, a German physicist, in 1988 (X. Lu et al., 2016). Hertz's pioneering experiments are considered among the earliest and most significant WPT demonstrations.

Nikola Tesla, who is the originator of AC electricity and a pioneer working on long-distance WPT technologies. He invented the technology of "Tesla coils" in 1893, which is used to generate strong electric fields that could transmit power wirelessly over short distances. In 1896, Nikola Tesla successfully transmitted high-frequency electricity over a distance of approximately 25 miles using his Tesla coil technology. This achievement involved lighting 200 bulbs and powering an electric motor. However, the high voltages

required for creating electric arcs posed significant risks, potentially causing harmful effects to both people and nearby electrical equipment (Tesla, 1914). Additionally, Tesla designed "Wardenclyffe Tower" to explore the possibility of transmitting power wirelessly across the globe. However, this thought was not widely implemented due to the big challenges of substantial construction costs and technical bottlenecks (X. Lu et al., 2016). Most of the work done by Nikola Tesla cannot be applied to large-scale manufacturing. However, it has profoundly inspired subsequent research.

2.5.2 The implementation of EV DIWC technology

In 1894, French inventors, named Hutin and LeBlanc, filed a patent for an innovative system to charge EVs using a contactless transformer (Hutin & LeBlanc, 1894). In the proposed system for electrified railways, the underground transmitter, driven by a 3 kHz alternating current, generates a fluctuating magnetic field that induces a voltage in the Rx, thereby powering the EV motors. Although the system proposed in this patent was not commercialized due to technical limitations of the time and it is still in progress until now. This event signaled the inception of the concept of EV-DIWC (Shladover, 1988). Furthermore, the concept of Road-powered EVs (RPEVs) was first introduced after proposing that patent. The 1976 development of highway cars with an IWPT system marked a significant early effort to explore DIWC for EVs (Shladover, 1988). In the system, the airgap distance was set at 2.5cm, and the operating frequency was 18Hz, which experimentally verified the feasibility of DIWC technology. Although the prototype encountered technical challenges and was not fully operational, this early work set the stage for the subsequent Santa Barbara Electric Bus (SBEB) Project initiated in 1979 (Lashkari et al., 1986; Lechner & Shladover, 1986).

In 1976, the Lawrence Berkeley National Laboratory (LBNL) team successfully designed the world's first experimental prototype adopting DIWC technology (Bolger, 1994; Bolger et al., 1978; Bolger et al., 1979). In 1986, researchers at the University of

California, Berkeley, first developed the first complete DIWC system as part of the Partners for Advanced Transit and Highway (PATH) Project. The system featured a 213-meter-long Tx, operating with 1,200A AC at 400 Hz, and an Rx that achieved 60 kW of power at a 7.6 cm gap with 60% efficiency. Despite its technical success, high construction costs, acoustic noise generated from the operation, high power supply and Rx coils, and low system efficiency limited its widespread use (Bolger, 1994). Since 2009, The Korea Advanced Institute of Science and Technology (KAIST) has developed and tested multiple prototypes of EV-DWC systems, which belong to the online electric vehicle (OLEV) project, and many advanced results have been achieved in the research and commercialization of EVs (Choi et al., 2014). The OLEV project is the first commercialized EV-DWC project worldwide. Six generations of OLEVs have been developed until now (Choi et al., 2014). Table 2.3, presented below, provides a brief comparison of various existing DIWC projects. E-type, Falt-type, W-type, U-type, or I-type are the Tx track coil types, which will be discussed in the following sections.

Table 2.3: Different EV IWPT projects

Institutes or	T/OOT	Tx	Rx	Application	Airgon	Power	Efficiency	Eroguanau
Teams	year	1X	KX	Application	Airgap	Power	Efficiency	Frequency
	2009	E-type	E-type	Golf Bus	1cm	3000W	88%	20kHz
*	2009	U-	Flat	Bus	17cm	6000W	72%	20kHz
	2009	type	type	Dus	1 / СП	0000 W	1 2 70	
KAIST	2010	W-	DD	Tram	12cm	15kW	74%	60kHz
	2010	type	coil	Hain	12011	138 77	7470	UUKIIZ
	2016	I-type	DD	Bus	20cm	27kW	80%	
	2010	1 type	coil	Dus	200111	271011	0070	
Bombardier	2010			Trams	6cm	200kW	90%	20kHz
Utah State	2016	016 CC C		Bus		25kW	86%	20kHz
University	2010	cc	CC	Dus		23K W	8070	ZUKITZ
OLNL	2016	RC	RC	car	16.2cm	20kW	93%	22kHz
Conductix-	2002	E-type	F-type	Bus	4cm	120kW	90%	15kHz
Wamfler AG	2002	E-type	1-турс	Dus	40111	120K W	90%	IJKIIZ
ETH Zurich	2013	RC	RC	Car	16cm	50kW	95.8%	85kHz
	2013	DD	DDQ	Car	12.5cm	10kW	90%	20kHz
The								
Polytechnic	2021	Triple	Triple	5.am	5cm	100kW	04.120/	051 ₅ 11 ₇₇
University of	2021	CC	CC	5cm	SCIII	100kW	94.12%	85kHz
Turin								

2.6 Analysis of the DIWC System

2.6.1 Static model analysis of DIWC system

Figure 2.8 illustrates a model of two-coupled coils for the DIWC system. The magnetic flux from the Tx and Rx coils is illustrated with blue and red lines, respectively. N_1 and N_2 represent the number of turns in the primary and secondary coils. U_1 and U_2 are the voltages across the primary and secondary coils, respectively, while i_1 and i_2 denote the currents in these coils. φ_{11} and φ_{22} are the self-magnetic fluxes of the Tx and Rx coils, and φ_{12} and φ_{21} indicate the mutual magnetic fluxes between them.

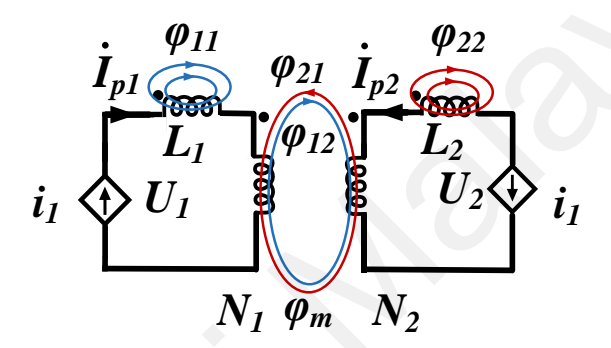


Figure 2.8: Two-coupled coils model with leakage inductances

2.6.2 Coil design parameters

2.6.2.1 Magnetic flux density B

As depicted in the equation (2.3), the magnetic flux density B describes the strength of the magnetic field flux φ . It characterizes the ability of the magnetic medium to conduct the magnetic field. Is used to describe the strength of the magnetic field flux φ . It defines the capability of the magnetic medium to conduct the magnetic field.

$$B = \mu H \tag{2.3}$$

Biot-Savart law, detailed in (2.4), describes the relationship between current and the magnetic field it produces. It can be observed that the field strength of a straight conductor diminishes with increasing distance. Additionally, for a circular coil, the center of the loop always generates the strongest magnetic field density *B*. The magnetic field is more consistent within the interior for a long solenoid but drops off sharply outside.

$$d\vec{B} = \frac{\mu_0}{4\pi} I \frac{d\vec{l} \times \vec{r}}{r^3}$$
 (2.4)

Here, the symbol μ_{θ} , denoting the permeability of free space, with a value of $4\pi \times 10^{-7}$ H/m. The term dl denotes the infinitesimal vector element of the conductor.

Therefore, for a circular coil, its magnetic field density $B_{circular}$ at the center of a circular coil with N turns is

$$B_{circular} = N \int_0^{2\pi} \frac{\mu_0 I}{4\pi R} d\theta = \frac{\mu_0 N I}{2R}$$
 (2.5)

Where R represents the radius of the coil.

For a rectangular coil, assume the length of the coil edge is a; the coil turn is set as 1. The length of the coil edge is b, the AC current flows evenly along its edges, and the magnetic field density on each side is B_s ; the overall magnetic field density at the center of the rectangular coil is represented by B_{rec} . Then

$$B_{\rm e} = \int_0^{\rm a} \int_0^{\rm b} \frac{\mu_0 I}{2\pi \sqrt{a^2 + b^2}} dl$$

$$B_{\rm rec} = \frac{{\rm a} + b}{2} B_e$$
(2.6)

$$B_{\rm rec} = \frac{a+b}{2} B_e \tag{2.7}$$

2.6.2.2 Self-inductance L, mutual inductance M, and coupling coefficient k.

Self-inductance (L), an electromagnetism parameter, originated from the discovery of a magnetic field surrounding the current-carrying conductor, as shown in (2.8). It quantifies how effectively a conductor can store energy in its generated magnetic field.

$$L = \frac{N\varphi}{i} = N \frac{d\varphi}{di}$$
 (2.8)

Where the relative permeability of a medium is μ_r . Substitute (2.3) into (2.8),

$$L_{i} = \frac{\mu_{0}\mu_{r}N_{i}^{2}A}{I}$$
 (i=1,2)

Where A denotes the cross-sectional area.

Mutual inductance (M) is the amount that describes the electromagnetic coupling between two coils. According to Neumann's law

$$M_{ij} = \frac{\mu_0}{4\pi} \int_{C_i} \int_{C_j} \frac{\overrightarrow{dl_i} . \overrightarrow{dl_j}}{|r_1 - r_2|}$$
(2.10)

Where r_1 and r_2 are the position vectors of a tiny current element on the respective magnetic generators, r_1 - r_2 is the distance between two tiny current elements.

The coupling coefficient k, as expressed in the equation (2.11), describes the extent of coupling of two adjacent coils. Mutual inductance M and self-inductance of two coils, L_1 and L_2 , as presented in Figure 2.8, depend on the coil dimensions, shape, and ferrite core arrangement (Cai et al., 2022). For efficient power transfer in an IWPT system, the air gap between the coils is generally between 10 and 40 cm (Mohamed et al., 2022).

$$k = \frac{M_{12}}{\sqrt{L_1 L_2}} \tag{2.11}$$

2.6.2.3 Induced voltage U_L

In Figure 2.8, the induced voltage U_i is

$$U_{i} = -L_{i} \frac{di}{dt} (i=1,2)$$
 (2.12)

As the current i_{p1} and i_{p2} through the conductor varies portrayed in Figure 2.9, it changes the magnetic field, inducing a voltage that opposes the current change, as stated by Lenz's Law.

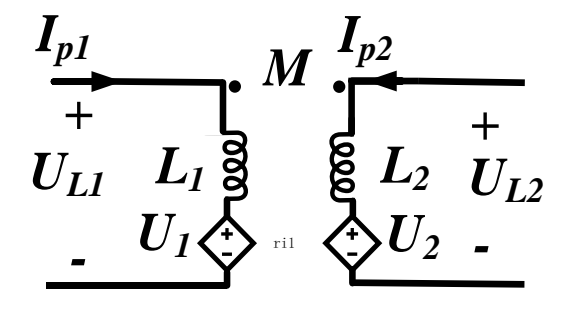


Figure 2.9: Equivalent circuit of coupled coils

2.6.3 Power losses analysis

Generally, power losses in a typical WPT system mainly come from three parts: coupling coils, rectifiers, and inverters. Power loss of rectifier and inverter is composed of conduction and switching losses (Li, Xu, et al., 2018; Thrimawithana et al., 2011).

2.6.3.1 Rectifier loss $P_{Rectifer}$

The rectifier is composed of diodes. The conduction loss of the diode is

$$P_{cond-D} = \frac{2\sqrt{2}}{\pi} U_f I_0 + r_D I_0^2$$
 (2.13)

Where U_{AK} is anode-cathode voltage, U_f is threshold voltage and r_D denotes the equivalent on-state resistance of diode. I_0 is the current passing through the rectifier.

$$P_{SW_{-D}} = \frac{12\sqrt{3}}{\pi} U_1 I_0 f_T \cos(\frac{\varphi}{2}) \frac{Q_{RR}}{I_{R-D}}$$
 (2.14)

It can be concluded that the switching loss of the rectifier in the WPT system can be ignored since the diode in the rectifier works at a power-grid frequency. So, the power loss of the rectifier is

$$P_{Rectifier} \approx 2 \int_0^{T_S} P_{cond_D} dt \tag{2.15}$$

2.6.3.2 Inverter loss $P_{Inverter}$

Inverter is consisted of MOSFETs. The conduction loss of MOSFET is

$$P_{\text{cond_MOS}} = \frac{1}{T_s} \int_0^{T_s} \mathbf{r}_{DS} i_D^2 dt = \mathbf{r}_{DS} I_0^2$$
 (2.16)

When the full bridge inverter works, two MOSFETs are always connected in the circuits. So, the conduction loss of the inverter is

$$P_{\text{cond}_INV} = 2P_{\text{cond}_MOS} + 2P_{\text{cond}_D}$$
 (2.17)

Where r_{DS} represents the on-state resistance of MOSFET.

The switching loss of MOSFET is

$$P_{SW_MOS} = V_{DS_AV} I_{d_SW} 4 f_T (\frac{e_{SW_ON} + e_{SW_ON}}{V_R I_R})$$
 (2.18)

Therefore, when the typical full-bridge inverter works, the switching loss of the inverter in the typical WPT system is

$$P_{SW_INV} = \frac{6\sqrt{6}}{\pi} I_0 V_{DC} f_T \left(\frac{e_{SW_ON} + e_{SW_ON}}{V_R I_R} + \frac{Q_{RR}}{I_{R_D}} \right) + P_{SW_D}$$
 (2.19)

Where V_{DC} is the RMS value of the full-bridge inverter's output voltage, I_0 is the current passing through the MOSFETs (Thrimawithana et al., 2011).

Then, the total inverter loss is

$$P_{Inverter} = P_{con_INV} + P_{SW_INV}$$
 (2.20)

2.6.3.3 Power loss of coils and compensated components

The coil resistance is a key factor that proportionally impacts system efficiency due to the magnetic coupling between the coils (Li, Xu, et al., 2018). The coil resistance R_C in the magnetic coupler incorporates two parts, which are indicated below.

$$R_{C} = R_{DC} + R_{AC}$$

$$R_{DC} = \frac{4\rho_{W}l_{W}}{k\pi d_{str}^{2}} = \frac{4\rho_{W}l_{T}N_{l}}{k\pi d_{str}^{2}} \qquad R_{AC} = \frac{4\rho_{W}l_{W}}{\pi k} \left(\frac{1}{d^{2}} + \frac{\pi^{3}(5N_{ll}^{2} - 1)d^{4}}{2880\delta^{4}\rho^{2}k^{2}}\right)$$
(2.21)

Where $\rho=1/w$ is the resistivity, d is the wire diameter, l_w is the winding length of the coil, and l_T is the mean length value of the coil turns.

In equation (2.21), R_{DC} denotes the DC wire resistance, which depends on the wire's material, length, and cross-sectional area. Conversely, R_{AC} , the resistance caused by high-frequency electromagnetic fields, includes three components: the proximity effect, which reflects the influence of adjacent current-carrying conductors on the wire; hysteresis losses, associated with the magnetic materials used in the magnetic coupler design; and the skin effect, which accounts for eddy currents induced by alternating fields (Patil et al., 2018; Roßkopf et al., 2013; Wojda & Kazimierczuk, 2018). To minimize the resistance caused by coil winding wire, Litz wire—characterized by the gauge of its strands or the insulating materials used—is commonly chosen for coil design in IWPT systems. The production and manufacturing of Litz wire primarily adhere to the American Wire Gauge (AWG) standards. In the compensation network, the compensated inductors and capacitors also have internal resistance R_c and R_l , which can be presented as

$$R_{c} = \frac{D_{C}}{\omega C} \qquad \qquad R_{l} = \frac{\omega L}{O} \tag{2.22}$$

2.6.4 Stationary model analysis of the DIWC system

Based on the brief introduction of all the essential physical parameters mentioned above, the stationary system analysis of the DIWC system, as depicted in, can be summarized as follows:

$$U_{L1} = N_1 \frac{d\varphi_{11}}{dt} + N_1 \frac{d(\varphi_{12} - \varphi_{21})}{dt} \quad U_{L2} = N_2 \frac{d\varphi_{22}}{dt} + N_2 \frac{d(\varphi_{21} - \varphi_{12})}{dt} \quad (2.23)$$

Since this ideal model does not account for the leakage mutual inductance, all magnetic energy is assumed to interact between the two coupling coils without any energy loss.

Consequently, in accordance with Ampere's circuital law, the condition is:

$$M = \frac{N_1 \varphi_{21}}{i_2} = \frac{N_2 \varphi_{12}}{i_1}, \quad L_1 = \frac{N_1 \varphi_{11}}{i_1}, \quad L_2 = \frac{N_2 \varphi_{22}}{i_2}$$
 (2.24)

Substitute the equation (2.8) and (2.24) into (2.23), then

$$U_{L1} = L_1 \frac{di_1}{dt} - M \frac{di_2}{dt} \qquad U_{L2} = L_2 \frac{di_1}{dt} - M \frac{di_1}{dt}$$
 (2.25)

It is evident that the induced voltage generated by the coupling coils primarily depends on both the self-inductance of the coils and their mutual inductance. To analyze the coupling coil system further, Figure 2.9 is introduced. Assume S_{12} or S_{21} represents the apparent power phasor that interacts between two connected coils via the magnetic field.

$$\dot{S}_{12} = U_{12} \dot{I}_{2} = j\omega M \dot{I}_{1} \dot{I}_{2} = j\omega M I_{1} I_{2} (\cos \theta_{12} - j \sin \theta_{12})$$

$$= \omega M \dot{I}_{1} \dot{I}_{2} \sin \theta_{12} + j\omega M I_{1} I_{2} \cos \theta_{12}$$

$$\dot{S}_{21} = U_{21} \dot{I}_{1} = j\omega M \dot{I}_{2} \dot{I}_{1} = j\omega M I_{1} I_{2} (\cos \theta_{21} - j \sin \theta_{12})$$

$$= \omega M \dot{I}_{1} \dot{I}_{2} \sin \theta_{21} + j\omega M I_{1} I_{2} \cos \theta_{21}$$
(2.26)

Where θ_{12} or θ_{21} is the phase angle of coil currents i_1 and i_2 .

It can be determined that the apparent power S_{12} or S_{21} equals the active power when the coil's phase angle is 90°. To achieve this, it is crucial to minimize the reactive power and adjust the phase angle to approach 90°.

2.7 Basic Compensated Configurations

In the earlier sections, magnetic flux leakage was disregarded, although it presents an unavoidable low coupling coefficient, significantly impacting the performance of the WPT system. Furthermore, the rise in reactive power also elevates the input apparent power level, subsequently increasing the inverter's output current, which leads to higher switching losses and system costs, as shown in equation (2.18). To maximize the active power delivered to the load side and minimize inverter losses, incorporating a resonant circuit in the WPT system is essential. This approach allows for constant voltage (CV) or constant current (CC) charging without requiring additional control modules. The basic compensation topologies, including Series-Series (SS), Series-Parallel (SP), Parallel-Series (PS), and Parallel-Parallel (PP), are analyzed as follows. The fundamental harmonic analysis (FHA) model is used to simplify the circuit model and do the calculations.

2.7.1 SS configuration

According to Kirchhoff voltage laws, in Figure 2.10, the input voltage U_1 and output voltage U_2 is

Figure 2.10: SS configuration

When the circuit reaches resonance, it must meet the following conditions:

$$(j\omega L_1 + \frac{1}{j\omega C_1})I_1 - j\omega MI_2 = 0$$
 $(j\omega L_2 + \frac{1}{j\omega C_2})I_2 - j\omega MI_1 = 0$ (2.28)

Therefore, in this type of topology, the compensated components relationship is

$$\frac{C_1}{C_2} = \frac{L_2}{L_1} \tag{2.29}$$

It can be observed that the key advantage of the SS configuration is that the capacitor design remains unaffected by variations in mutual inductance M, making it highly suitable for use in the DIWC system. In a DIWC system with an SS configuration, the issue of reducing mutual inductance fluctuations can be effectively disregarded.

However, based on the two preceding equations, it can be deduced the input impedance Z_{in} is as follows:

$$Z_{in} = \frac{U_1}{I_1} = R_1 + j(\omega L_1 - \frac{1}{\omega C_1}) + \frac{\omega^2 M^2}{(R_2 + R_L) + j(\omega L_2 - \frac{1}{\omega C_2})}$$
(2.30)

The system DC-DC transfer efficiency is

$$\eta = \frac{\omega^2 M^2 R_L}{(R_2 + R_L)^2 R_1 + \omega^2 M^2 (R_2 + R_L)}$$
(2.31)

It can be observed that, if the secondary side is disconnected while the primary side remains powered, the equivalent impedance of this topology corresponds to the resistance of compensated components, which is relatively low. Consequently, as noted, a high current will be generated almost immediately, potentially damaging circuit components.

2.7.2 SP configuration

For SP configuration shown in Figure 2.11, according to the Kirchhoff voltage laws (KVL) and current laws (KCL), the equation is expressed as

$$U_{1} = (R_{1} + j\omega L_{1} + \frac{1}{j\omega C_{1}})I_{1} - j\omega MI_{2} \qquad I_{2} = I_{C2} + I_{L}$$

$$U_{2} = -(R_{2} + j\omega L_{2})I_{2} + j\omega MI_{1} \qquad U_{2} = R_{L}I_{L} = \frac{1}{j\omega C_{2}}I_{C2}$$
(2.32)

From the equation, it is derived that.

$$I_{L} = \frac{j\omega M}{R_{L} + (R_{2} + j\omega L_{2})(j\omega C_{2}R_{L} + 1)}I_{1}$$
 (2.33)

When the SP configuration circuit occurs resonance, the resonant condition is

$$(j\omega L_1 + \frac{1}{j\omega C_1})I_1 - j\omega MI_2 = 0 \qquad j\omega L_2I_2 + j\omega MI_1 = 0$$

$$U_1 \qquad L_1 \qquad R_2$$

$$L_2 \qquad C_2 \qquad R_L$$
(2.34)

Figure 2.11: SP configuration

From (2.34), the compensation network design should follow.

$$C_1(L_1L_2 - M^2) = C_2L_2^2 (2.35)$$

The input impedance Z_{in} can be deduced as follows.

$$Z_{in} = \frac{U_1}{I_1} = (R_1 + j\omega L_1 + \frac{1}{j\omega C_1}) + \frac{\omega^2 M^2 (j\omega C_2 R_L + 1)}{R_L + (R_2 + j\omega L_2) (j\omega C_2 R_L + 1)}$$
(2.36)

To avoid the reactive power generated by the source, the following condition have to impose that:

$$\omega L_{1} - \frac{1}{\omega C_{1}} = -lmag(\frac{\omega^{2} M^{2} (j\omega C_{2} R_{L} + 1)}{R_{L} + (R_{2} + j\omega L_{2})(j\omega C_{2} R_{L} + 1)})$$
(2.37)

The DC-DC system efficiency is

$$\eta = \frac{\omega^{2} M^{2} R_{L} \left(R_{2}^{2} + \omega^{2} \left(L_{2} + C_{2} R_{L} R_{2}\right)^{2}\right) \left(1 + \omega^{2} C_{2}^{2} R_{L}^{2}\right)}{\left(R_{1} \left(R_{2}^{2} + \omega^{2} \left(L_{2} + C_{2} R_{L} R_{2}\right)^{2}\right) + \omega^{2} M^{2} \left(R_{2} + R_{L} + \omega^{2} C_{2}^{2} R_{L}^{2} R_{2}\right)\right) \left(\left(R_{2} + R_{L} + \omega^{2} C_{2}^{2} R_{L}^{2} R_{2}\right)^{2} + \omega^{2} L_{2}^{2}\right)}$$
(2.38)

Based on the analysis above, it is evident that equation (2.36) still encounters the issue of short circuits when the Rx side is open in SP-topology circuits. This challenge remains significant when implementing this configuration in DIWC applications. Furthermore, in (2.35), The involvement of variable *M* affects resonance conditions to change if the mutual inductance varies, which is unavoidable due to movement of EVs in a DIWC system. To address these challenges, Series-Parallel-Series (SPS) topology or Inductor-Capacitor-Inductor (LCL) compensation is proposed (Mohamed et al., 2022).

2.7.3 PS configuration

The equivalent circuit of the PS topology system is illustrated in Figure 2.12. In this configuration, the Tx coupling coil is connected in parallel with the AC voltage source. The KVL equations are as follows:

$$U_{1} = (R_{1} + j\omega L_{1})I_{p} - j\omega MI_{2} \qquad I_{1} = I_{C1} + I_{p}$$

$$U_{2} = -(R_{2} + j\omega L_{2})I_{2} + j\omega MI_{1} \qquad U_{1} = I_{p}(R_{1} + j\omega L_{1}) = \frac{1}{j\omega C_{1}}I_{C1} \qquad (2.39)$$

$$U_{1} \bigcirc \begin{matrix} R_{1} \\ C_{1} \end{matrix} \qquad \begin{matrix} R_{2} \\ C_{2} \end{matrix} \qquad \begin{matrix} C_{2} \\ R_{L} \end{matrix}$$

Figure 2.12: PS configuration

When the circuit occurs resonance, the resonant condition is

$$C_1(L_1 + \frac{M^4}{L_1C_2L_2R_L}) = C_2L_2 \tag{2.40}$$

The input impedance Z_{in} is

$$Z_{in} = \frac{U_1}{I_1} = \frac{1}{(R_1 + j\omega L_1 + j\omega C_1)(R_L + R_2 + j\omega L_2 + \frac{1}{j\omega C_2}) + \omega^2 M^2}$$
(2.41)

The condition below should be met when the reactive power drops to zero.

$$lmag(Z_{in}) = \frac{\omega L_1 \left(1 - \omega^2 L_1 C_1\right) - \omega C_1 \left(R_1 + \frac{\omega^2 M^2}{R_2 + R_L}\right)^2}{\left(1 - \omega^2 L_1 C_1\right)^2 + \omega^2 C_1^2 \left(R_1 + \frac{\omega^2 M^2}{R_2 + R_L}\right)^2}$$
(2.42)

The system DC-DC transfer efficiency is

$$\eta = \frac{\omega^2 M^2 R_L}{R_1 (R_2 + R_L) + (R_1 + R_L) \omega^2 M^2}$$
 (2.43)

In the PS configuration, the compensation capacitor on the primary side is influenced not only by the coupling system of the Tx and Rx coils but also by the load. Thus, the parallel compensation topology on the primary side is more appropriate for systems where the Tx and Rx sides are relatively stable, and the load remains fairly constant.

2.7.4 PP configuration

The analysis of the Tx and Rx sides shown in Figure 2.13 gives as below:

$$U_{1} = (R_{1} + j\omega L_{1})I_{p} - j\omega MI_{2} \qquad I_{1} = I_{C1} + I_{p}$$

$$U_{2} = -(R_{2} + j\omega L_{2})I_{2} + j\omega MI_{1} \qquad U_{1} = I_{p}(R_{1} + j\omega L_{1}) = \frac{1}{j\omega C_{1}}I_{C1} \qquad (2.44)$$

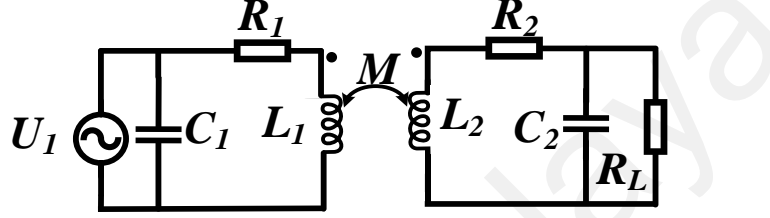


Figure 2.13: PP configuration

The capacitors and inductors are designed as follows.

$$(L_1L_2 - M^2) \quad C_2L_2^2 = C_1(M^4C_2R_L + L_2(L_1L_2 - M^2)^2)$$
 The input impedance Z_{in} is

$$Z_{in} = \frac{U_{1}}{I_{1}} = \frac{1}{\frac{R_{L} + (R_{2} + j\omega L_{2})(1 + j\omega C_{2}R_{L})}{(R_{1} + j\omega L_{1})(R_{L} + (R_{2} + j\omega L_{2})(1 + j\omega C_{2}R_{L})) + \omega^{2}M^{2}(1 + j\omega C_{2}R_{L})} + j\omega C_{1}}$$
(2.46)

The system DC-DC efficiency is

$$\eta = \frac{\left(\omega^{2} M^{2} A^{2} \left(1 + \omega^{2} C_{2}^{2} R_{L}^{2}\right)\right) R_{L}}{\left(R_{1} A B + B^{2} - \omega^{2} L_{1} L_{2} A\right)^{2} + \left(A B \omega L_{1} + A \omega L_{2} R_{1} + B \omega^{2} L_{2}\right)^{2}} \frac{A L_{1}}{C_{1} \left(A R_{1} + \omega^{2} M^{2} B\right)}$$
where $A = R_{2}^{2} + \omega^{2} (L_{2} + C_{2} R_{L} R_{2})^{2}$, $B = R_{2} + R_{L} + \omega^{2} C_{2}^{2} R_{L}^{2} R_{2}$

$$(2.47)$$

The PP configuration exhibits the same characteristics as the PS configuration, making this topology unsuitable for dynamic charging as well.

2.7.5 LCC-S topology

In a hybrid compensation network, diverse composite topologies can be created by combining capacitors and inductors in various configurations. The frequently utilized topologies include LCC-S, LCC-LCC, SPS, and others. The LCC-S topology presented

in Figure 2.14 can achieve a constant voltage (CV) output mode, with the system's output power being proportional to the square of the mutual inductance M. When an offset occurs, the reduction in mutual inductance will greatly diminish the system's output power. Conversely, the LCC-LCC topology can achieve a constant current (CC) output mode, and the double-sided LCC provides greater flexibility in adjustment compared to LCC-S. However, it involves more compensation parameters, making the design more complex.

The LCC-S compensation topology provides several advantages, with the LCC type used on the Tx side and the Series type applied on the secondary side. When the LCC topology is tuned to the resonant frequency, the inverters deliver only active power to the load, and the Tx current remains unaffected by the load. On the Rx side, using a single capacitor in series with the Rx coil reduces both the cost and complexity of the circuit compared to more intricate compensation networks. Moreover, power loss is slightly lower than in higher-order compensation networks. The LCC-S topology also has the benefit of adjusting the voltage gain by modifying the compensated inductance.

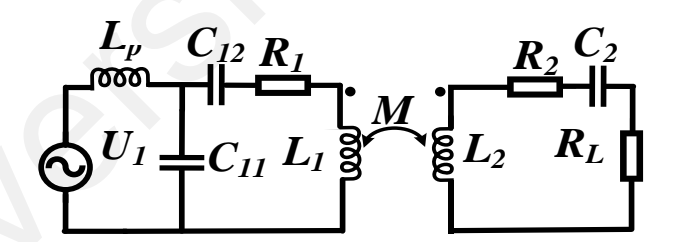


Figure 2.14: LCC-S topology

According to the topology, the system input impedance Z_{in} and the voltage gain of output to input G_v can be obtained,

$$\begin{cases} Z_{\rm in} = \frac{8L_{\rm fl}^2 R_{\rm L}}{\pi^2 M^2} \\ G_{\rm v} = \frac{U_{\rm out}}{U_{\rm in}} = \frac{M}{L_{\rm fl}} \end{cases}$$
(2.48)

The equation (2.48) indicates that the LCC-S configuration has the characteristic of constant voltage output. The output voltage is unaffected by the load. Therefore, to adjust the output voltage in constant voltage mode, assuming the mutual inductance and input

voltage remain relatively stable, it is essential to ensure that the inductance value of the primary-side compensation (L_p) matches the mutual inductance (M) between the Tx and Rx. This approach is ideal for DIWC applications and simplifies the system design process. (Li et al., 2019; Mohamed et al., 2022).

2.8 Magnetic Coupler

The magnetic coupler used in the IWPT system, containing a pair of planar coils, accompanied by ferrites and an electromagnetic shield on each side, is the most important element for deciding magnetic coupling performance and WPT system output characteristics, as portrayed in Figure 2.15. The size, turns, and shape of the coil, the airgap distance between Tx and Rx, the material of the wire used to wind coils, and the arrangement of the ferrite and electromagnetic shield are mainly considered during the process of magnetic coupler design. Furthermore, the factors related to economic cost and commercial use must also be considered. For instance, in the Tx side of the dynamic charging system based on IPT technology, a larger amount of coil is required to be mounted on the road. Essential reductions in coil material cost can inspire the widespread use of DIWC applications in current research regarding magnetic coupler design. The factors of coil misalignment, coupling factor, and quality factor, referring to the relationship between coil self-inductance and coil resistance, are mainly discussed, leading to the emergence of various types of coil structures (Mohamed et al., 2020).

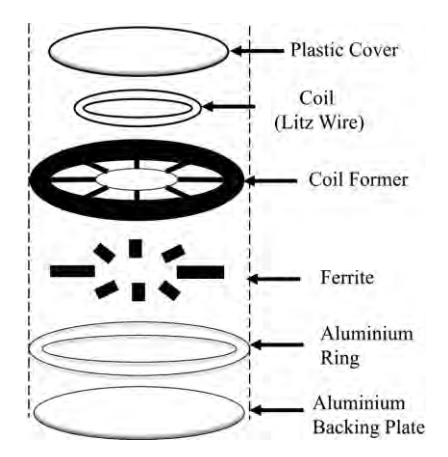


Figure 2.15: Exploded view of general magnetic coupler (Ahmad et al., 2018)

2.8.1 Basic coil structures

The magnetic coupler currently used is classified by whether the magnetic field is distributed on both sides or a single side of a coil. can be divided into single-side flux type and doubled-side flux type. The single-side flux type refers to the coil primarily possessing a magnetic field on one side, while in the double-sided type, the magnetic field is distributed on both sides of the coil. On the other hand, polarized and non-polarized coils are terms describing whether the coil can generate a magnetic field with a specific directionality. In this section, a brief introduction for several basic coil structures is provided.

2.8.1.1 Circular coil

The circular coil is widely used and analyzed in EV WPT systems, especially for SWC applications (Bosshard et al., 2014; Miller & Daga, 2015). The magnetic field generated by a circular coil looks like a fountain, and this flux pattern is beneficial for reducing flux leakage (Long et al., 2016). For a static WPT system with one circular Rx and one Tx coil, the misalignment tolerance in each direction is the same; that is, there is no directionality. In 2011, Budhia, Covic, et al. (2011) optimized circular coil, especially by studying and comparing the number, shape and distribution of magnetic cores, which effectively reduced the consumption of magnetic cores, lightened the coil mass, improved the efficiency and realized the power transmission of 2~5kW with a large air gap and have good misalignment tolerance. However, the magnetic field generated by circular coils is highly limited by the pad diameter. Compared with other coils of the same size, the coupling coefficient of the circular coil is small when the air gap spacing and offset are the same. When the air gap spacing is 1/4 of the coil diameter, the coupling coefficient is about 0.2 (Covic & Boys, 2013; Patil et al., 2018). Furthermore, the circular coil also faces a power null-point problem when one side of the coils gets around 40%

misalignment, resulting in power/output voltage fluctuations. Therefore, the circular coil is unsuitable for the EV DIWC system.

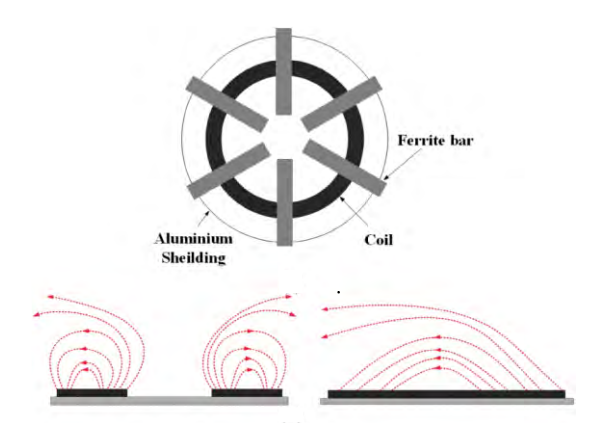


Figure 2.16: Circular coil and its flux distribution (Patil et al., 2017)

2.8.1.2 Flux pipe

UA 's team proposed a Flux pipe coil, as shown in Figure 2.17. This type has two coil terminals which are wound on the same core. The flux pipe coil, with a magnetic flux height approximately half the length of the coil, demonstrates strong lateral misalignment performance over a wide range, while maintaining a coupling factor comparable to that of a circular coil. This coil was initially proposed as an improvement to the traditional circular coil design (Budhia, Boys, et al., 2011; Budhia, Covic, et al., 2011). However, it is so challenging to get practical use since its coil shape is solenoid; a big performance decrease caused by the magnetic field conduction impediments occurs when one side of the flux pipe is touched or put near the aluminum shield. The flux loss lowers the WPT system efficiency (Patil et al., 2017). Moreover, a large magnetic field leakage occurs on the left and right sides of the flux pipe. Some latest research trying to combining this structure with other types of coil structures in order to improve other coil structures misalignment tolerance, but the disadvantage of enlarged magnetic flux loss still exists, an increased coil wire cost and coil weight are also needed to be considered (Wang et al., 2024). The researcher from Saitama University in Japan was also proposed similar structures like Flux pipe coil, named H type of coil, before (Chigira et al., 2011; Takanashi

et al., 2012). The same problems of magnetic field leakage on both sides of coils exist in this H-type of coil, too (Takanashi et al., 2012).

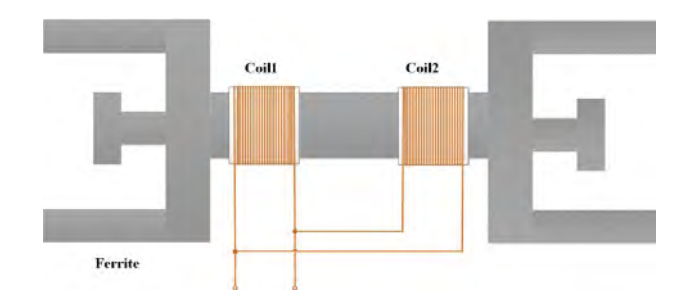


Figure 2.17: Flux pipe (Patil et al., 2018)

2.8.1.3 Rectangular coil

Compared with circularly polarized coils of the same size, rectangular or square coils may show a lower magnetic coupling and system efficiency for a given coil area (Bosshard et al., 2014). However, the rectangular coil, shown in Figure 2.18, may improve its coupling ability by extending the coil area. Moreover, a better misalignment tolerance, larger cost-effectiveness, and better power capability can be presented at the same time (Ahmad et al., 2018; Chen et al., 2016). This is because it can generate a more uniform and more concentrated magnetic field near the corner of the coil, which can show a better performance in the DWC system (Bosshard et al., 2014). F. Lu et al. (2016) proposed a DIWC system including six rectangular Tx segmented coils placed side by side. Experiment results show that around ±2% power fluctuation is achieved as Rx moves along the row of rectangular coils, indicating the superiority of implementing rectangular coils in the DWC system.

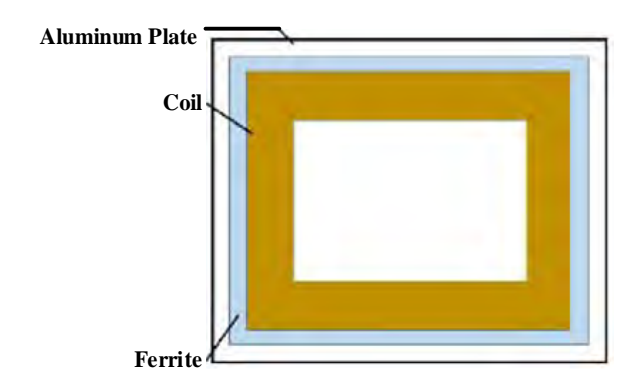


Figure 2.18: Rectangular coil (Ahmad et al., 2018)

2.8.1.4 **DD** coil

In 2013, the UA team introduced a quasi-double coil design, the DD (double D) coil, crafted from a single wire. This design, presented in Figure 2.19, merges the features of both flux pipes and circular coils. (Budhia, Boys, et al., 2011). The winding directions of the left and right coils are opposite, resulting in their magnetic fields being connected in series while their electrical connections are in parallel. Therefore, by orienting the winding directions of the left and right coils oppositely and connecting their magnetic fields in series while their electrical connections are in parallel, the central magnetic flux of the two coils is enhanced. This configuration effectively increases the magnetic field height, which is approximately half the length of the coil, thereby improving both the coupling and the ability to resist offsets between the coils (Budhia, Boys, et al., 2011). Additionally, the magnetic field is mainly concentrated on one side of the coil. In contrast to a solenoid coil, which has magnetic fields distributed on both sides, the DD coil enhances the efficiency of the magnetic field utilization. This design reduces magnetic field leakage and minimizes the impact of metal shielding on the WPT system. Li et al. (2014) developed an 8kW wireless charging system using DD coils, achieving an efficiency of approximately 95.66% with a transmission distance of 20 cm. The system maintained a high efficiency of 95.39% even with a lateral offset of 30 cm. Furthermore, DD coils can also be suitable to be implemented in DIWC applications. For instance, Liu et al. (2023) constructed a DIWC system solely using DD coils on Tx and Rx sides, and, at last, the voltage fluctuation is generally less than 4.6%, and the system overall efficiency can reach more than 90.75% with 8cm distance of airgap between Tx and Rx. However, due to the parallel distribution of the magnetic field of the DD-type coil, it cannot be mixed with a single coil. In addition, when the coil offset exceeds about 34%, the coupling factor may get zero (Budhia, Boys, et al., 2011). The same power null point problem exists in dynamic charging applications (Buja et al., 2016).

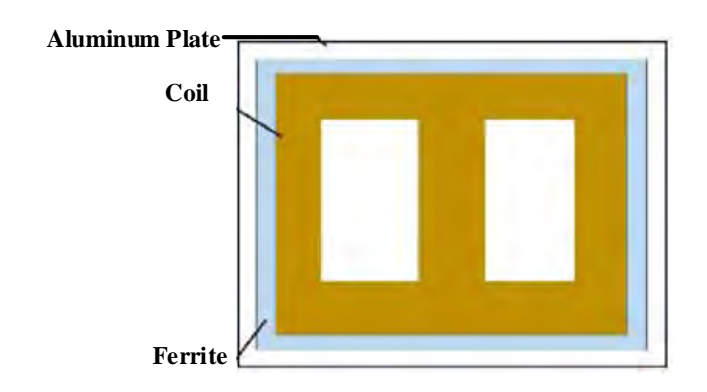


Figure 2.19: DD coil (Ahmad et al., 2018).

2.8.1.5 DDQ coil

Considering the bad misalignment tolerance of DD coils, the UA team proposed a DDQ coil to solve this problem by adding a quadrature coil on the center of the DD coil, as shown in Figure 2.20, which strengths the magnetic coupling and improves misalignment tolerance compared with DD coil. This combined magnetic coupler effectively solves the problem of the magnetic field zero point, and the charging area is also extended (Budhia, Boys, et al., 2011). However, it also brings disadvantages such as increased Litz wire cost and makes circuit design more complicated. The coil size is also two times larger than circular and square coils (Budhia, Covic, et al., 2011).

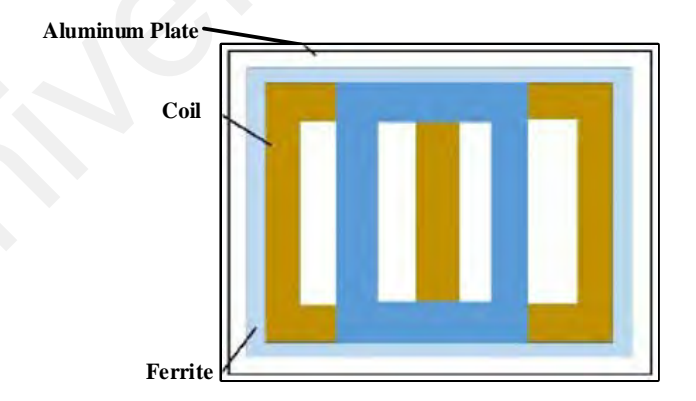


Figure 2.20: DDQ coil (Ahmad et al., 2018).

2.8.1.6 Bipolar coil

To reduce the cost of copper wire, Zaheer A.A. proposed the bipolar coil as portrayed in Figure 2.21. Unlike the DD and DDQ coils, where one D-shaped coil overlaps half of the area of the other, the bipolar coil serves as an intermediate design between the DD

and DDQ coils. It can gather more magnetic flux than DD coils but not as much as DDQ coils (Boys & Covic, 2015; Covic et al., 2011; Zaheer et al., 2013). However, its simpler geometry reduces copper costs and losses by 25.17% compared to the DDQ coil, while still maintaining similar functionality (Zaheer et al., 2013).

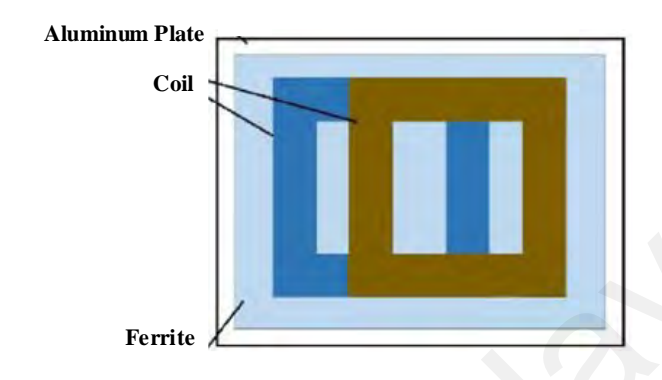


Figure 2.21: Bipolar coil (Ahmad et al., 2018).

2.8.1.7 Other coils

Other multi-coil designs are briefly illustrated in Figure 2.22. Tripolar (TP) coil contains three partly-overlapped coils and each coil achieves decoupling with another coil as shown in Figure 2.22 (I) (Kim et al., 2016; Kim et al., 2014). Three coils can work separately and show high rotational misalignment tolerance after assembling them together. Kim et al. (2016) implemented this TP coil as the Tx and circular or bipolar coil as Rx. The hardware results present a significant apparent power reduction obtained in the system with the proposed TP coils. Furthermore, the challenges of magnetic field leakage and EMF are also mitigated (Protection, 2010).

A three-coil structure was proposed by the KAIST team in 2014 (Moon et al., 2014). As depicted in Figure 2.22 (II), a small coil is nested in a large coil, and the added small coil enhances the coupling degree between the Tx and the Rx coil. Two more added coils denote a higher coupling factor is further achieved in the four-coil structure, as presented in Figure 2.22 (III) (Moon et al., 2014; Moon & Moon, 2015). The tolerance to the variation of load resistance or charging distance, contributed by added coils, is also increased (Moon et al., 2014). However, the phenomenon of frequency splitting,

potentially resulting in system efficiency reduction, should be avoided by carefully adhering to proper but complicated and strict design procedures. A crossed-DD coil structure, as depicted in Figure 2.22 (IV), has been examined by positioning two coils on the same plane with partial or complete overlap (Lv et al., 2020). Decoupling can be effectively achieved between two identical crossed DD coils placed side by side (Xiang et al., 2018). It can be concluded that the crossed-DD coil significantly enhances the misalignment tolerance of the magnetic coupler, making it particularly suitable for use in DIWC applications (Lv et al., 2020; Xiang et al., 2018; Yin et al., 2024).

Table 2.4 presents a comparison of different coil structures as below.

Table 2.4: Comparison of different coil structures

Coil shape	Misali- gnment tolerance	Magnetic flux	Transm- ission distance	Polarization	Leakage flux	Commonly used in DIWC system
Circular	Poor	Single- sided	Low	Non- polarized	High	Tx/Rx Coil
Rectangular	Medium	Single - sided	Low	Non- polarized	Medium	Tx/Rx Coil
Flux pipe/H type	Poor	Double- sided	Low	Polarized	Medium	
DD	Medium	Single- sided	Medium	Polarized	Extremely low	Tx/Rx Coil
DDQ	High	Double- sided	High	No- polarized	Extremely low	Tx/Rx Coil
Bipolar	Medium	Double- sided	High	Polarized	Low	Rx
Tripolar	High	Single- sided	High	Polarized	Low	Tx/Rx Coil
Crossed-DD	High	Double- sided	Medium	Polarized	Medium	Tx

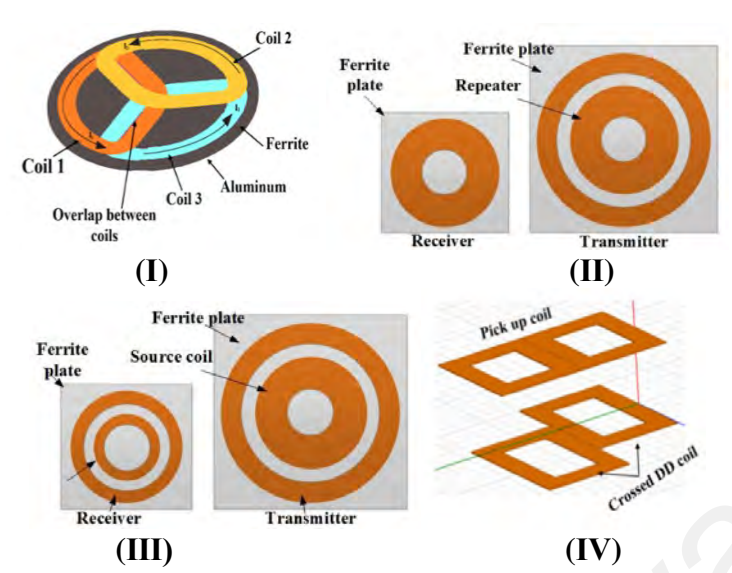


Figure 2.22: (I) Tripolar coil; (II) Three coil; (III) Four coil; (IV) Crossed DD coil (Mohamed et al., 2020; Patil et al., 2018).

2.8.2 Categories of single DIWC Tx coil

In the DIWC system of EVs, as illustrated in Figure 2.23, there are basically two categories of single Tx coil used in the DIWC system, depending on Tx coil length, namely long track and lumped track coil type (Li et al., 2019).

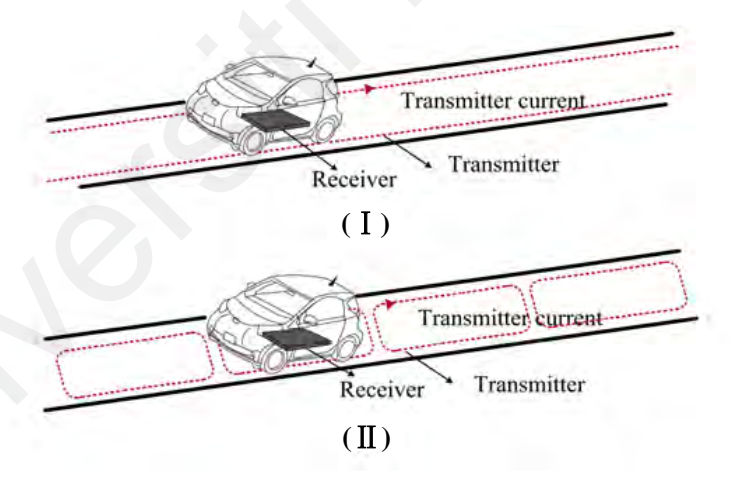


Figure 2.23: Tx coil in DIWC system (I) long track; (II) segmented track (Li et al., 2019).

2.8.2.1 Long track

The long-track coil type, it was the oldest type of DIWC single Tx coil, which was proposed in 1994 (Bolger, 1994). The Tx side only requires a single coil with extended coil length. The length of the Tx coil is longer than that of the Rx coil, the EV charging system can continue to supply power, and the magnetic coupler can show a constant coupling factor when driving above the transmitter without frequent switching control. It

also means that charging more than one EV at the same time is possible. This structure has fewer circuit components, and the power distribution network and control are simple. However, such a long Tx coil leads to increased magnetic field loss and reduced coupling factor and system efficiency. When some part of this type of magnetic coupler meets some technical problem and cannot work, it causes a large broken charging area. This problem can be solved by lumped track type, which makes it easier to replace faulty transmitting coils. A lumped track is composed of multiple individual coils; the length of a single Tx coil is close to the length of a single Rx coil. The KAIST team has contributed a lot to this type of track coil type, and six generations of DIWC magnetic couplers with long-track-coil type have been shown in Table 2.5 and Figure 2.24.

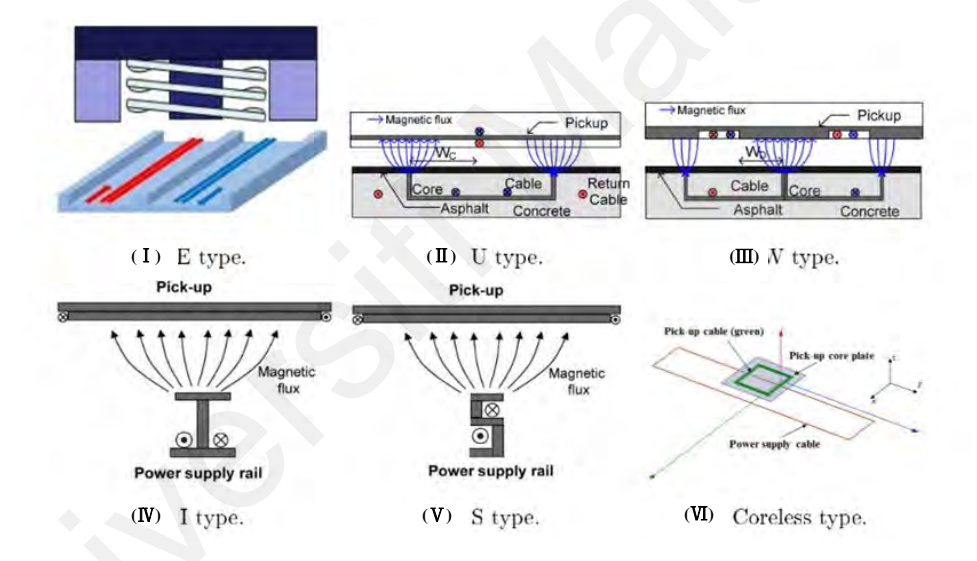


Figure 2.24: Six generation OLEV's magnetic coupler (Cui et al., 2022)

Table 2.5: Comparison of six generation OLEV's long track structure

Parameters	U-Type	E-Type	I-Type	S-Type	W-Type	Coreless
	J 1	71		71	31	type
Track width	Large	Small	Small	Small	Medium	Small
Airgap	Medium	Small	High	High	High	High
Leakage EMF	High	Low	Medium	Small	High	Very low
Lateral	Medium	Small	Medium	Large	Medium	Large
misalignment	Wicdium	Siliali	Miculuiii	Large	Miculuiii	Large
Efficiency	Low	High	High	Low	Medium	High
Output power	Small	Small	High	High	High	High

2.8.2.2 Lumped track

Compared to the long-track coil type, the lumped-track coil type comprises multiple segmented Tx coils, and each coil is roughly the same length as the Rx coil, resulting in lower magnetic field leakage and enhanced system efficiency. However, the Rx coil receives power predominantly from nearby Tx coils, with frequent activation and deactivation of the Tx coils is contingent on the relative position of Rx with respect to the Tx coils to save energy and reduce interference from the external environment on the system. Thus, adopting an appropriate Tx segmented control method for this type of magnetic coupler is indispensable (Li et al., 2019).

The characteristics between the lumped track coil type and the long track coil type are shown in Table 2.6.

Table 2.6: Characteristics of lumped track and long track

Type	Advantages	Disadvantages		
	Lower cost;	Lower coupling factor;		
Long track	Constant power transfer;	Harder to repair and replace broken		
	Simpler circuit structure.	coils		
	Less leakage magnetic	Higher Litz Wire cost;		
Lumped track	field; Better system efficiency; Easier to control.	Complex circuit structure and control		
		strategy;		
		Need to consider the mutual inductance		
	Easier to control.	between Tx coils.		

2.8.3 Typical methods of reducing mutual inductance fluctuations in DIWC system

At present, most of the research on reducing mutual inductance fluctuations focuses on the optimization design of magnetic couplers. Several factors are considered in this process, including optimizing coil turns, coil length or width, the spacing between adjacent Tx coils; integrating coils with different coil shapes. Table 2.7 summarizes the recent research progress on reducing mutual inductance fluctuations by optimizing the DIWC magnetic coupler.

Table 2.7: Recent research on reducing mutual inductance fluctuations through DIWC magnetic coupler design.

Solution Types	Description of Solutions	References
Coil turns	Optimizing Rx coil turns to minimize fluctuations	(Li et al., 2019)
	Using DD coil shows better misalignment tolerance	(Liu et al., 2023)
Coil shape	Integrate DD and Q on the Rx side to compensate for fluctuation with each other.	(Li et al., 2019)
	Put two small DD coils on both sides of long Q coil	(Shi et al., 2021)
	Increase Rx coil length a bit	(Li et al., 2019)
Coil dimension	Reduce Rx coil size to improve misalignment tolerance	(Cai et al., 2022)
	Two-layer DD coil partly overlapped	(Liu et al., 2017)
Coil amon gament	Two Q coils partly overlapped	(Wang, Y. et al. 2018)
Coil arrangement	Put DD coil crossed.	(Xiang et al., 2018)
	Change the spacing between adjacent coils.	(Mukhatov et al., 2018)
Magnetic core arrangement	Reduce fluctuations by properly arranging ferrite bars	(Cui et al., 2018; Liu et al., 2023)
Coil winding A Q coil with an opposite windin direction is added		(Shi et al., 2022)
Coil number	Adopting a dual Rx structure to fix the fluctuations	(Campi et al., 2021)
Con number	Adopting a triple Rx structure to fix the fluctuations	(Zhou et al., 2024)

2.8.4 Findings of the gap

In this section, the research gap identified in this study is summarized. The research problem is outlined and emphasized in Section 1.2, which highlights the necessity of developing a new multi-purpose magnetic coupler for DIWC systems. The proposed design aims to address key challenges, mainly including minimizing decoupling between adjacent Tx coils, reducing mutual inductance fluctuations, and optimizing power transfer efficiency. Table 2.8 provides a comparative analysis of existing designs in relation to multiple objectives. In Table 2.8, it can be concluded that crossed coil structures can help reduce mutual inductance fluctuations and overlapped coil structures can help optimize transfer efficiency. Therefore, the possibility to propose a multi-purposes magnetic coupler design, including the purposes shown in Table 2.8, is generated by combining the

characteristics of these two types of coil structures. A much more detailed and comprehensive comparison of various coil structures, supported by simulation results, is detailed in Section 3.4.

Table 2.8: Comparison of existing designs with the main purposes of achieving decoupling, reduced mutual inductance fluctuations and optimized efficiency

Referenc es	Tx coil shape	Rx coil shape	Achieve decouplin g between adjacent Tx coils?	Reduce mutual inductanc e fluctuatio n?	Enhance transfer efficienc y?	Maximiz e the coil usage?	Avoi d Powe r null point ?
(Li et al., 2019)	DD or Q coil	Overlap -ped DD and Q coils	Yes	Yes	No	No	No
(X. Li et al., 2020)	Overla p-ped DD and Q coils	Q coil	Yes	Yes	No	No	Yes
(Liu et al. 2017)	Crosse d DD coil	DD coil	Yes	Yes	Yes	No	Yes
(Liu et al. 2022)	DD coil	DD coil	No	Yes	No	Yes	No
(Cai et al., 2022)	Partly overlap -ped Q coil	Circul ar coil	Yes	Yes	No	Yes	Yes
(F. Lu et al., 2016)	Q coil	Q coil	No	Yes	No	Yes	Yes
(S. Li et al.,2020)	Q coil	Q coil	Yes	Yes	No	Yes	Yes
Proposed	Q coil	Q coil	Yes	Yes	Yes	Yes	Yes

2.9 Summary

This chapter examines wireless charging for EVs, focusing on DIWC technologies. It compares various charging methods and different WPT technologies. Key aspects regarding to the research like coil design, power losses, and compensated configurations are analyzed, alongside magnetic coupler structures. The chapter also highlights historical developments, challenges in reducing mutual inductance fluctuations, and identifies research gaps. The necessity and possibilities of this research, aimed at proposing a new cross-overalpped DIWC magnetic coupler with multiple purposes, is highlighted.

CHAPTER 3: RESEARCH METHODOLOGY

3.1 Introduction

This chapter presents a systematic analysis of the proposed magnetic coupler. It begins with a comprehensive explanation of the design methodology for the proposed DIWC magnetic coupler. Based on this flowchart, primary parameter setting is given in Section 3.3. Furthermore, a comparative analysis is conducted between conventional and the proposed DIWC magnetic couplers. The objective is to preliminarily demonstrate the superior performance of the proposed cross-overlapped Tx coil structure, as outlined in Section 3.4. Section 3.5 analyses the proposed DIWC magnetic coupler featuring three activated segmented Tx coils, including methods for decoupling adjacent coils and obtaining stable mutual inductance between Tx coils and Rx through simulations conducted in ANSYS Maxwell. Section 3.6 provides a detailed circuit analysis of the DIWC system incorporating the proposed structure, utilizing the fundamental harmonic analysis (FHA) method. Finally, Section 3.7 discusses the experimental setup of the DIWC system with the proposed magnetic coupler.

3.2 Design Procedures of the Proposed DIWC Magnetic Coupler

Figure 3.1 shows the flow chart of the proposed magnetic coupler's design. By reading literature related coil design for DIWC system. The advantages and disadvantages of conventional crossed and overlapped coil structures are comprehensively analyzed. There is a critical need to develop a novel coil structure that integrates the beneficial features of both crossed and overlapped configurations while effectively addressing their respective limitations, as finally identified in this research. Therefore, a cross-overlapped coil structure is proposed, with its effectiveness being preliminarily validated through comparative analysis of mutual inductance variation with conventional single-Tx designs in Section 3.4. To further evaluate the performance of the proposed structure under dynamic conditions, multiple segmented Tx coils are incorporated in proposed structure,

as detailed in Section 3.5 and Section 3.6 of this chapter. However, to achieve desired and stable mutual inductance between Tx coils and Rx with simultaneous decoupling between adjacent Tx coils, several critical parameters must be defined before designing the proposed structure, as outlined in Section 3.3. These include the primary dimensions of the ti1 and ti2 coils, the operating frequency (ω) , the input voltage (U_{in}) , the airgap distance (d_{tr}), the desired mutual inductance between the activated Tx coils and the Rx coil, and the acceptable range of mutual inductance fluctuations (α). Initially, Nti₃ is set to 1, and N_r is designed to match N_{ti1} , N_{ti2} , and N_{ti3} . The coil turns N_{ti3} are then incrementally increased until the simulated mutual inductance M approaches the desired mutual inductance M_s between the Tx coils and Rx. Next, the mutual inductance M_{T1T2} or M_{T2T3} between adjacent segmented Tx coils is simulated. By adjusting the turns of the ti3coil (N_{ti3}) , M_{T1T2} or M_{T2T3} is reduced to zero. Depending on whether M_{T1T2} or M_{T2T3} is positive or negative, the widths of the ti1, ti2, and ti3 coils are optimized until M_{T1T2} or M_{T2T3} reaches zero, ensuring decoupling between adjacent Tx coils. To further optimize system efficiency, the coupling coefficient between the activated Tx coils and the Rx coil is maximized by fine-tuning the Rx coil's length and turns. Additionally, an appropriate segmented coil control method is implemented. Ultimately, a magnetic coupler featuring a cross-overlapped Tx coil structure is proposed, achieving the desired mutual inductance M_s and fluctuation α . This design has been validated through simulation, analysis, and experimental prototyping.

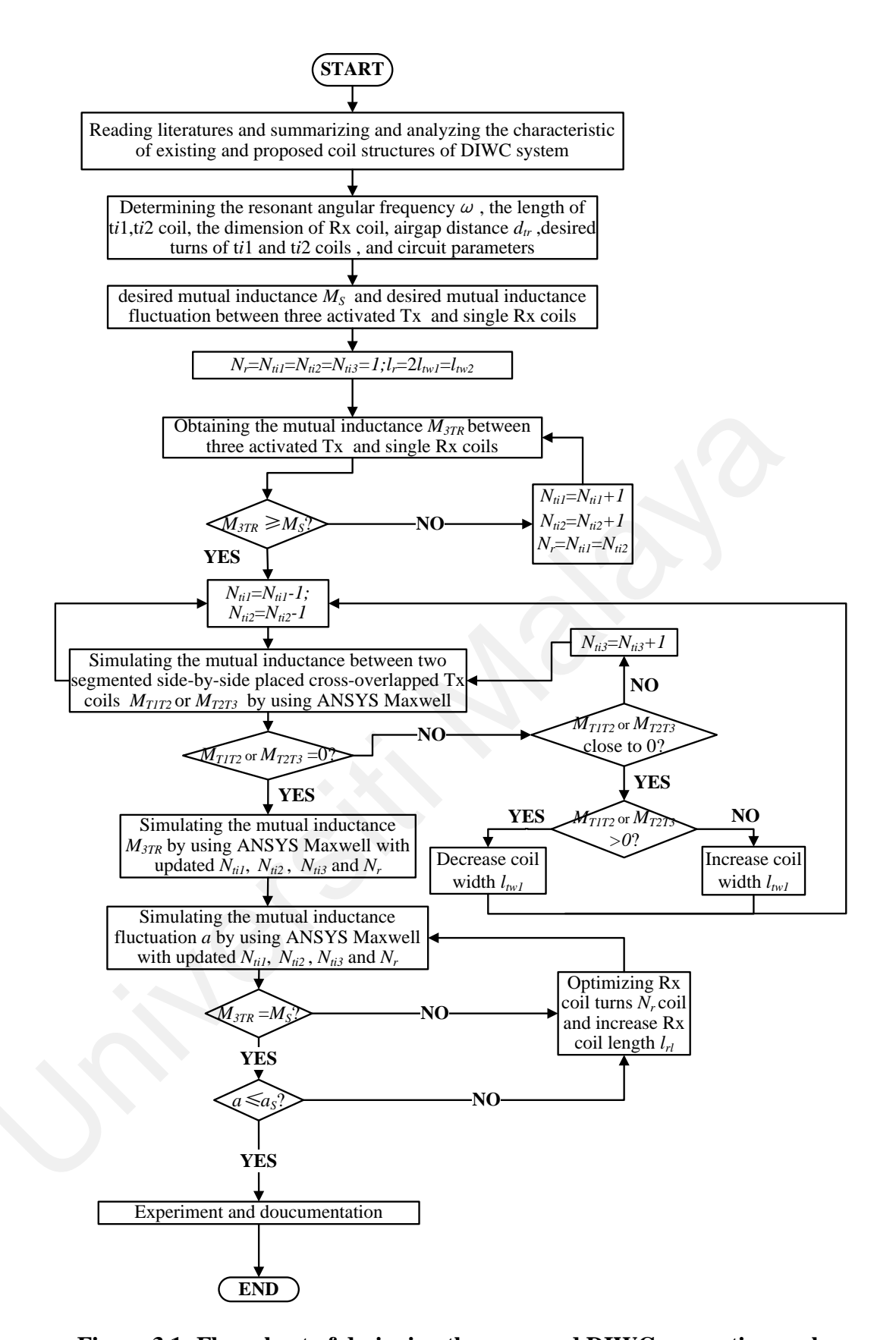


Figure 3.1: Flow chart of designing the proposed DIWC magnetic coupler

3.3 Primary Parameter Settings

This study includes a case study in Chapter 3 to verify the efficacy of the proposed structure and the design approach elaborated in Section 3.2. The coil parameters for the

proposed configuration are extracted from the simulation model constructed using ANSYS Maxwell. Employing these parameters enables the decoupling of adjacent Tx coils and ensures stable mutual inductance between the Tx coils and the Rx. Furthermore, critical circuit parameters are set prior to the experimental setup.

3.3.1 Coil parameters

The relevant key parameters of the proposed DIWC magnetic coupler are listed in Table 3.1. The airgap distance between Tx and Rx is set as 120mm. The proposed coil structure is presented in Figure 3.2 (V). The dimension of the small Tx Q coils is 210*360 mm², the dimension of the big Tx Q coil is 420*360 mm² and the dimension of the Rx Q coil is 420*360 mm². The zero points of the DIWC magnetic couplers, labeled as "O₁", are set at the center position of the single Tx coil. The variables *x* and *y*, depicted in Table 3.1 represent the Rx coil position along the X and Y directions, respectively.

Table 3.1: The key parameters of the proposed magnetic coupler

Symbol	Description	Value	Symbol	Description	Value	
Symbol		(mm)			(mm)	
d_{tr}	Airgap	120	l_{rw}	Width of the Rx coils	210	
d	Litz wire diameter	4.5	C, C 1	Crossed distance	c=120	
и	Litz wire diameter	4.3	C, C1	Crossed distance	$c_I = 180$	
l_t	Length of the single	360	142. 7	Winding length of	72	
ι_t	Tx coils	300	w_{t1}	small Tx Q coils	12	
l_{rl}	Length of the Rx	360	W_{t2}	Winding length of big	18	
ι_{Pl}	coil	300	VV 12	Tx Q coils	10	
1	Width of the small	210	- 11	Winding length of Rx	72	
l_{tw1}	Tx Q coils	210	w_r	coil	72	
1	Width of the big Tx	420	0	The second of th	<i>x</i> =0,	
l_{tw2}	Q coils	420	O_I	The central position	y=0	

3.3.2 Circuit parameters

For the circuit design, the primary parameters are outlined in Table 3.2. The implemented WPT system operates at a frequency of 85 kHz, with an input voltage (U_{dc}) of 180 V. The target mutual inductance between the activated Tx coils and the Rx is set

at 33 μ H, with desired fluctuations (α) constrained to within $\pm 1\%$. The experimental setup is designed to deliver a power input of 2 kW.

Table 3.2: The primary circuit parameters setting

f	Operating frequency	85kHz	U_{dc}	Input voltage	180V
Ms	Desired mutual inductance between activated Tx coils and Rx	33	α	Desired mutual inductance fluctuation between Tx and Rx coils	±1%
P_{in}	Input power level	2kW			

3.4 Analysis of Conventional and Proposed DIWC Magnetic Couplers with Single Tx

A comprehensive analysis of the newly proposed DIWC magnetic coupler is provided in this section, as portrayed in Figure 3.2 (V). Three types of conventional DIWC magnetic couplers have been gathered from existing research. These types include the crossed but non-overlapped DD Tx coil with non-crossed and non-overlapped DD Rx coil (Xiang et al., 2018), non-crossed and non-overlapped DD Tx and Rx coil (Buja et al., 2016), non-crossed but overlapped Tx and Rx coils (Y. Li et al., 2020; Li, Lin, et al., 2018), as depicted in Figure 3.2 (I)-(III). In addition, the coil structure shown in Figure 3.2 (IV) is also analyzed and compared with the proposed one mentioned above, which consists of the Tx with no-crossed but overlapped triple Q coils and the Rx with no-crossed and no-overlapped dual Q coils. Figure 3.3 illustrates the variation trend of mutual inductance between Tx and Rx along the X and Y directions for the five types of DIWC magnetic couplers presented in Figure 3.2 (I)-(V).

Compared to the circular coil, the DD coil exhibits better misalignment tolerance in the Y direction, verifying its greater suitability for DIWC applications (Buja et al., 2016). However, the problem lies in the fact that when adjacent DD Tx coils are placed side by

side, it inevitably results in cross-coupling between them, and the system efficiency will decrease if this phenomenon is not eliminated (Li et al., 2019). Moreover, when the DD coil is offset along the X direction shown in Figure 3.2 (II), transfer power will dramatically decrease, leading to a power null point phenomenon as presented in Figure 3.3 (I) (Buja et al., 2016). To address the aforementioned issues, placing the DD Tx coil in a crossed configuration, as shown in Figure 3.2 (I), and setting coil width l_{twl} to onequarter of the coil length l_t can effectively achieve natural decoupling with same-side identical crossed DD coils (Xiang et al., 2018). However, by comparing the crossed and non-crossed Tx coil designs shown in Figure 3.3 (I) and Figure 3.3 (II), the crossed configuration results in lower mutual inductance. Moreover, the problem of power nullpoint or zero mutual inductance still exists. Consequently, regarding the problems mentioned above of weakened magnetic field and occurrence of power null-points, inserting a Q coil in Tx of Figure 3.2 (II), shown in Figure 3.2 (III), can help address these problems by strengthening the mutual coupling between Tx and Rx coils. For the DIWC magnetic coupler portrayed in Figure 3.2 (III), light-green Rx and light-blue Tx Q coils can realize natural decoupling with green Rx and blue Tx DD coils, respectively (Li, Lin, et al., 2018). This leads to two independent coils in Tx and Rx, eventually increasing the power transfer capability. However, simultaneous natural decoupling can be achieved between the Rx light-green Q and the Tx blue DD coils, as well as between the Rx green DD and the Tx light-blue Q coils, as shown in Figure 3.2 (III), resulting in underutilization and construction costs of the Rx coil, which are evident in both static charging and dynamic charging applications (Li et al., 2019; Li, Lin, et al., 2018). Additionally, compared with single-layer Rx coil structure, the use of dual-layer Rx coils implies increased vehicle weight and the necessity for added volume in the limited installation space of EVs. Moreover, magnetic saturation may occur in this mixed structure of Q and DD coils, caused by one side of the coupler producing a more intense magnetic field

compared to the other side of the coil (Li, Lin, et al., 2018). This issue can be addressed by adjusting the phase difference of the current between the Q and DD coils to 90 degrees. However, more circuitry needs to be added to the system, resulting in higher system costs and losses (Y. Li et al., 2020). Furthermore, according to the comparison between overlapped (Figure 3.2 (III)) and non-overlapped coils (Figure 3.2 (I), (II)) as shown in Figure 3.3, it can be concluded that although overlapped coils can transfer more power due to its enhancement on mutual coupling, the power null-point phenomenon or zero mutual inductance may persist in X direction misalignment as illustrated in (III) curve (-21 cm < x < -10 cm or 10 cm < x < 21 cm) of Figure 3.3 (I) if the light-colored Q coil is not optimally designed properly (Y. Li et al., 2020; Li, Lin, et al., 2018). Another DIWC magnetic coupler with overlapped Tx coils is described in Figure 3.2 (IV). The current direction of the blue DD Tx and green DD Rx coils are respectively transformed into dual Q coils. By comparing the X-direction and Y-direction performance of the DIWC magnetic couplers (Figure 3.2 (III)) in Figure 3.3 (I)-(II), it is evident that the magnetic coupler shown in Figure 3.2 (IV) not only can completely avoid the occurrence of power null-points but also achieve much more stable mutual inductance in X-direction. It also obtains higher mutual inductance between Rx and Tx compared to all other DIWC magnetic couplers in Figure 3.2. Moreover, it requires the installation of only a singlelayer Rx coil, which is more desirable for EV applications. However, this overlapped Tx structure of the DIWC magnetic coupler also intensifies the unwanted cross-coupling between same-side Tx coils in DIWC applications. Furthermore, compared to the structure that can naturally achieve decoupling between DD and Q coils, there is significant mutual inductance between blue and light-blue Q coils in Figure 3.2 (IV), resulting in increased self-inductance of the Tx coil if they are connected in series. As a result of increasing both self-inductance and cross-coupling between same-side Tx coils, the cost of compensated components in Tx will be increased (F. Lu et al., 2016).

To address the primary limitations of Figure 3.2 (IV) while preserving its key advantages over other DIWC magnetic couplers illustrated in Figure 3.2 (I)-(III), the proposed Tx structure has been introduced in Figure 3.2 (V). The Tx features one large Q coil and two small Q coils of the same size. These three coils are positioned in a crossed and partially overlapped configuration, thereby forming a Tx coil group with similar current directions as portrayed in Figure 3.2 (IV). The interspacing c between adjacent Tx coils in Figure 3.2 (IV) is equal to one-third of the Tx coil length l_t in order to realize decoupling between adjacent Tx coils and reduce mutual inductance fluctuation. Further details on how to realize decoupling between adjacent coils will be outlined in Section 3.5. In the proposed system, the Rx coil employs a single Q coil of the same total size as the dual Q coils used in Figure 3.2 (IV).

According to the analysis in Figure 3.3, the proposed magnetic coupler, compared to non-overlapped Tx structures illustrated in Figure 3.2 (I) and Figure 3.2 (II), possesses the characteristic of an overlapped coil structure to enhance mutual coupling, similar to the overlapped structures presented in Figure 3.2 (III) and Figure 3.2 (IV). Furthermore, the proposed magnetic coupler also exhibits characteristics reminiscent of the crossed structure in Figure 3.2 (II). Consequently, when compared to non-crossed Tx coil structures portrayed in Figure 3.2 (II), (III), and (IV), mutual inductance fluctuation during the motion of the Rx in the Y direction, depicted in Figure 3.3 (II), is notably improved. The same function of decoupling can also be achieved between adjacent Tx coils like the crossed structure shown in Figure 3.2 (I), setting it apart from all other structures presented in Figure 3.2. Compared to the mixed structure comprising Q and DD coils shown in Figure 3.2 (III) and the structure solely utilizing DD coils presented in Figure 3.2 (II) and Figure 3.2 (III), the proposed magnetic coupler can achieve much better X-direction misalignment tolerance and also avoid the occurrence of power zero points. Moreover, compared to Figure 3.2 (III), the proposed magnetic coupler utilizes only a

single-layer Rx (Li et al., 2019; Li, Lin, et al., 2018). Thus, it can be concluded that this newly proposed DIWC magnetic coupler combines the features of crossed and overlapped coil structures by addressing the primary limitations of Figure 3.2 (IV) while preserving its key advantages over the other coil structures shown in Figure 3.2.

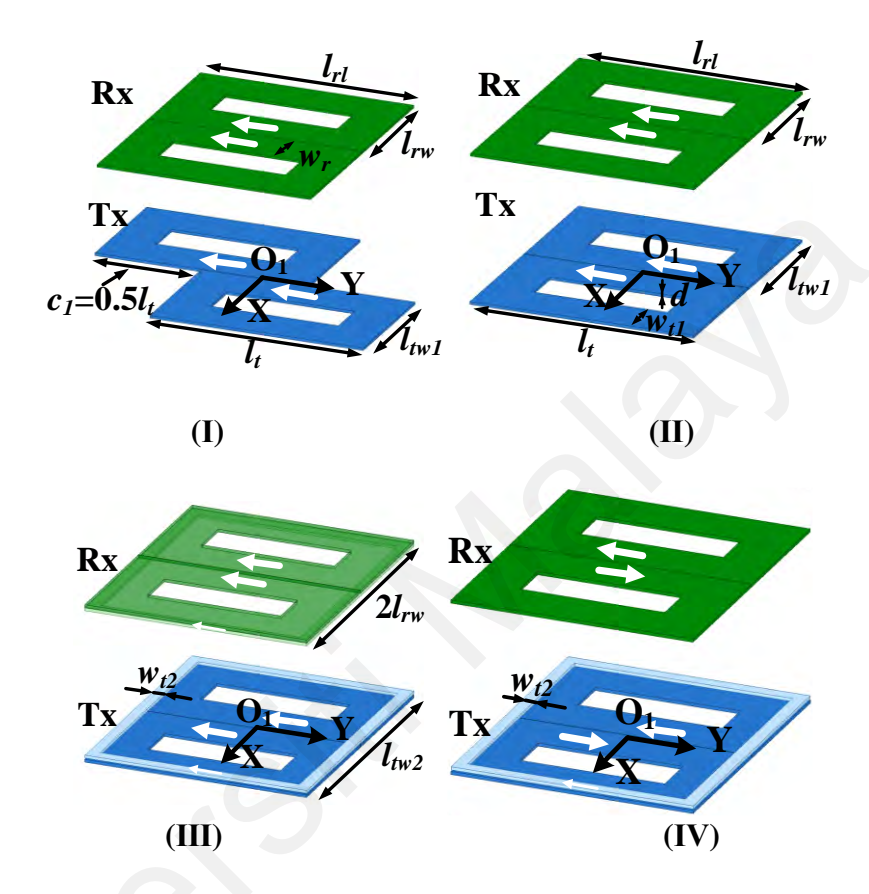


Figure 3.2: Conventional and proposed DIWC magnetic couplers (I) The crossed but non-overlapped DD Tx coil with non-crossed and non-overlapped DD Rx coil; (II) non-crossed and non-overlapped DD Tx and Rx coils; (III) non-crossed but overlapped Tx and Rx coils; (IV) non-crossed but overlapped Tx coil and non-crossed and non-overlapped Rx coil; (V) Cross-overlapped Tx coil and non-crossed and non-overlapped Rx coil

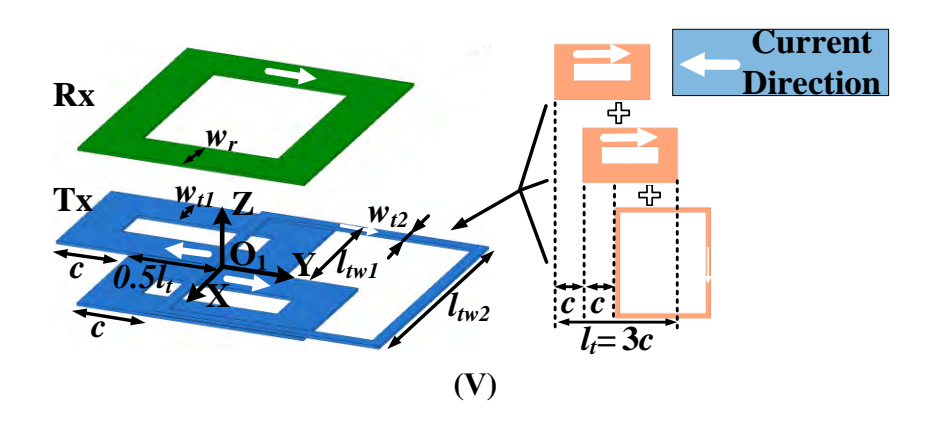


Figure 3.2, continued: Conventional and proposed DIWC magnetic couplers (I) The crossed but non-overlapped DD Tx coil with non-crossed and non-overlapped DD Rx coil; (II) non-crossed and non-overlapped DD Tx and Rx coils; (III) non-crossed but overlapped Tx and Rx coils; (IV) non-crossed but overlapped Tx coil and non-crossed and non-overlapped Rx coil; (V) Cross-overlapped Tx coil and non-crossed and non-overlapped Rx coil

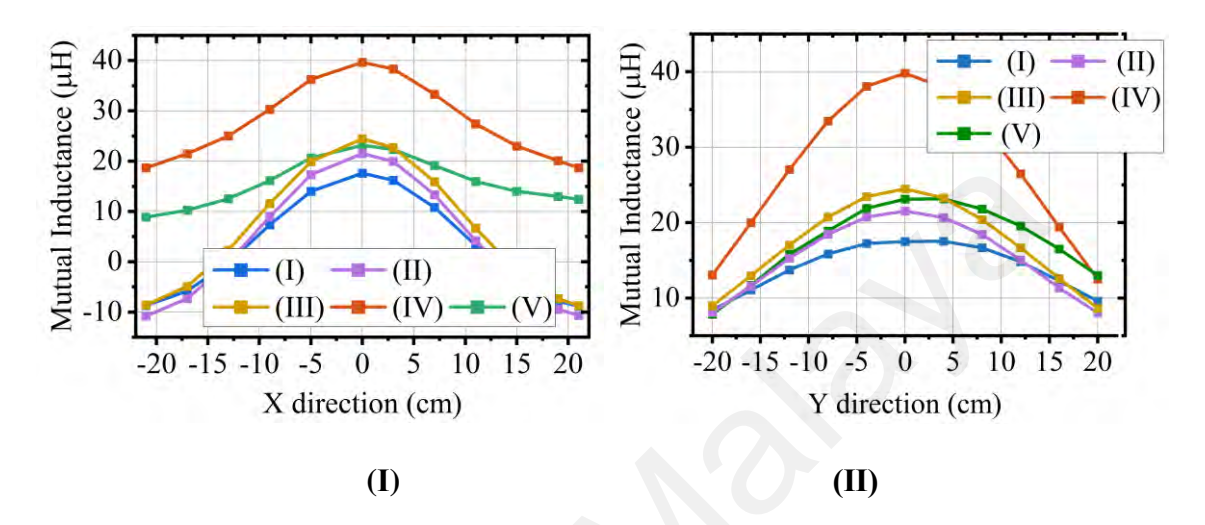


Figure 3.3: Comparison of five types of DIWC magnetic coupler (Figure 3.3 (I)-(V)) misalignment performance (I) Along the X-direction; (II) Along the Y-direction

3.5 Analysis of the Proposed DIWC Magnetic Coupler with Three Segmented Tx Coils

The magnetic coupler proposed in Figure 3.2 (V) is employed in this DIWC system with the purpose of testing its dynamic performance, as illustrated in Figure 3.4. The coils labeled as ti1, ti2, and ti3 together constitute the Ti (i=1,2,3,4) coil group. The T1, T2, and T3 coil groups are tagged in blue, red, and yellow, respectively. The single Rx Q coil is represented in green. The coil arrangement of the proposed DIWC magnetic coupler with T1, T2, and T3 coil groups are also presented in Figure 3.4. The point "O" is set as the zero-starting position of Rx coil movement.

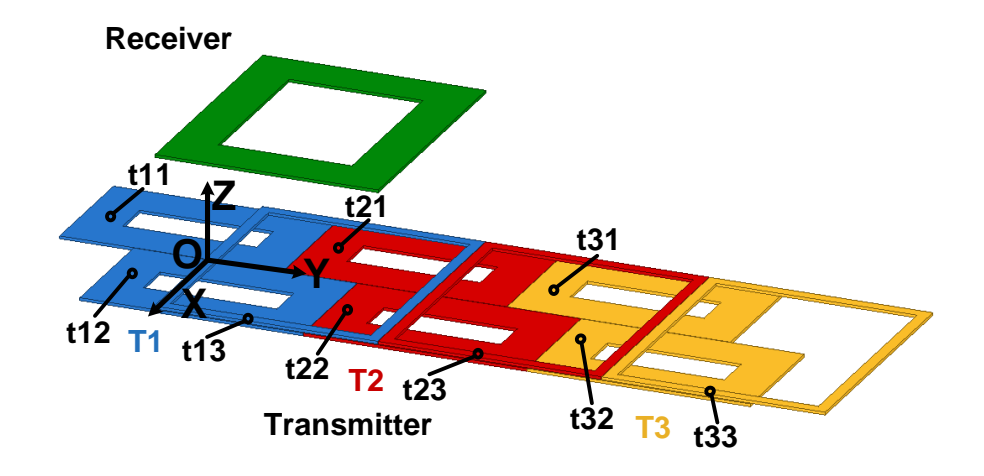


Figure 3.4: The structure of proposed DIWC magnetic couplers

3.5.1 Transmitter design with its decoupling method

In the Tx, L_{ti1} , L_{ti2} , and L_{ti3} represent the self-inductance of ti1, ti2 and ti3 coils. The mutual coupling that exists between the T1 and T2 coil groups, tagged in blue and red, is illustrated in Figure 3.5 (I), respectively. The self-inductances of Ti coil groups, labeled as L_{Ti} (i=1,2,3,4), are represented as follows.

$$L_{Ti} = L_{ti1} + L_{ti2} + L_{ti3} + 2M_{ti1ti2} + 2M_{ti1ti3} + 2M_{ti2ti3}$$
 (3.1)

The coupling model describing the mutual inductance between T1 and T2 coils is also shown in Figure 3.5 (II). According to Kirchhoff's law, the voltages at the T1 or T2 coil group can be expressed as. (j=1,2,3)

$$\dot{U}_{T1} = j\omega(\sum_{j=1}^{3} L_{t1j} - 2M_{t11t12} + 2M_{t11t13} + 2M_{t12t13})\dot{I}_{t1} + j\omega(-\sum_{j=1}^{3} M_{t11t2j} - \sum_{j=1}^{3} M_{t12t2j} + M_{t13t21} + M_{t13t22} - M_{t13t23})\dot{I}_{t2}$$

$$\dot{U}_{T2} = j\omega(-\sum_{j=1}^{3} M_{t11t2j} - \sum_{j=1}^{3} M_{t12t2j} + M_{t13t21} + M_{t13t22} - M_{t13t23})\dot{I}_{t1} + j\omega(\sum_{j=1}^{3} L_{t2j} - 2M_{t21t22} + 2M_{t21t23} + 2M_{t22t23})\dot{I}_{t2}$$

$$M_{T1T2} = -\sum_{j=1}^{3} |M_{t11t2j}| - \sum_{j=1}^{3} |M_{t12t2j}| - |M_{t13t23}| + |M_{t13t21}| + |M_{t13t21}| + |M_{t13t22}| = 0$$
(3.2)

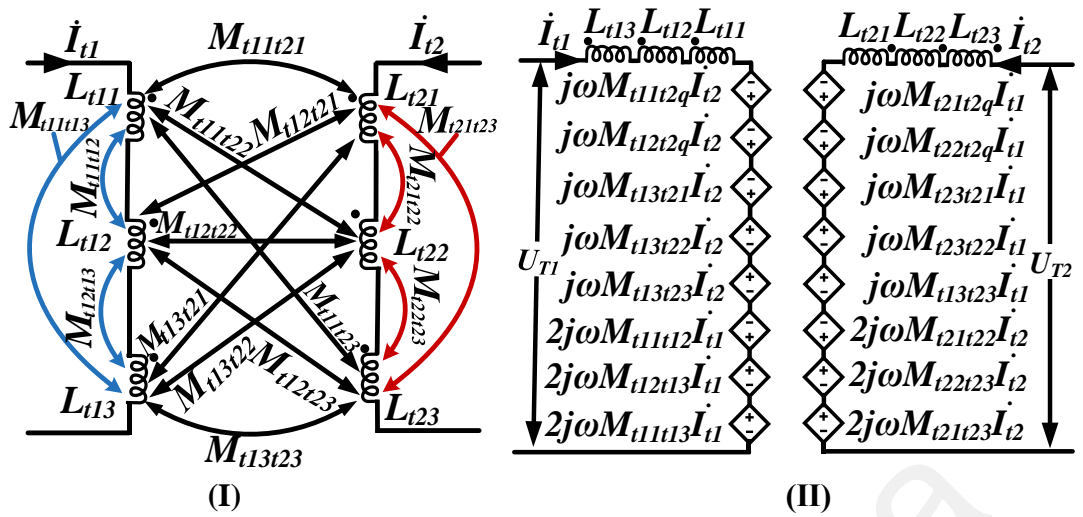


Figure 3.5: (I) Coupling model of the proposed decoupling method (II) Equivalent circuit of the model (q = 1, 2, 3)

3.5.2 Receiver design

In the Rx, the self-inductance of the Rx coil is labeled as L_R . When T1 ,T2 and T3 coils transfer power during the moving process of Rx coils as depicted in Figure 3.6, the mutual inductance between the Rx coil and the ti1, ti2, and ti3 coils can be denoted as M_{ti1R} , M_{ti2R} , M_{ti3R} (i=1,2,3), respectively. The overall mutual inductance between Ti and Rx coils can be expressed as follows:

$$M_{T1R} = \sum_{i=1}^{3} M_{\text{tli}R} \ M_{T2R} = \sum_{i=1}^{3} M_{\text{t2i}R} \ M_{T3R} = \sum_{i=1}^{3} M_{\text{t3i}R}$$
 (3.4)

 M_{3TR} represents the sum of mutual inductance between T1, T2, T3, and Rx coils expressed in (3.5).

$$M_{3TR} = M_{T1R} + M_{T2R} + M_{T3R} (3.5)$$

The coupling coefficient between Tx and Rx k_{TR} , expressed in (3.6a) and (3.6a), can significantly affect the efficiency performance of the DIWC system (Cai et al., 2022; F. Lu et al., 2016).

$$k_{T1R} = \frac{M_{T1R}}{\sqrt{L_{T1}L_R}} \qquad k_{T2R} = \frac{M_{T2R}}{\sqrt{L_{T2}L_R}} \qquad k_{T1R} = \frac{M_{T3R}}{\sqrt{L_{T3}L_R}}$$
 (3.6a)
$$k_{TR} = k_{T1R} + k_{T2R} + k_{T3R}$$
 (3.6b)

The cross distance between the ti1 and ti2 coils is assumed to be the same as the cross distance between the ti2 and ti3 coils to obtain relatively uniform mutual coupling between Tx and Rx coils. Both distances are labeled as c, shown in Figure 3.2 (V). The cross ratio of the Tx is defined as z, which is expressed in (3.7).

$$z = \frac{c}{l_t} \tag{3.7}$$

The number of coils turns N_{ti} (i=1,2,3), and N_r is expressed in (3.8) where d is equal to 0.45cm.

$$N_{t1} = N_{t2} = \frac{w_{t1}}{d}, N_{t3} = \frac{w_{t2}}{d}, N_r = \frac{w_r}{d}$$
 (3.8)

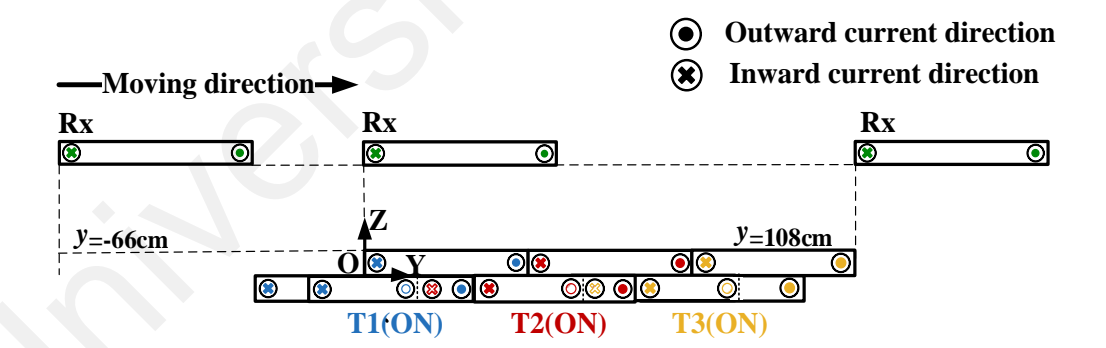


Figure 3.6: When Rx length l_r =42cm, side view of activated T1, T2, and T3 coils

3.6 Analysis of the DIWC system with the Proposed DIWC Magnetic Coupler

3.6.1 The DIWC system configuration

Figure 3.7 illustrated the configuration of the proposed DIWC system with the Tx structure of the lumped track coil type. U_{in} and U_o represent the input and output DC voltage, respectively. On the Tx side, four branches of segmented Tx coils, denoted as T1, T2, T3, and T4, are connected in parallel and are used in conjunction with a common

full-bridge inverter. This arrangement aims to reduce circuit costs and avoid the safety risks associated with operating inverters in high-power and high-voltage lines, compared to the alternative of connecting a separate inverter in each branch (Mohamed et al., 2022). On the Rx side, Rx coils are connected to a rectifier. After rectification, a resistive load R_L can replace the battery equivalent impedance (Hossain et al., 2022). For obtaining better transfer efficiency, the typical range of the actual battery equivalent impedance in EV systems is chosen and considered as 10 to 100 ohms for systems with a power level of less than 2 kW in this research (Li et al., 2019). LCC-S compensated topology, where L_{pi} , C_{pi} , and C_{ti} (i=1,2,3,4) constitute the LCC compensation network on the Tx side while C_r constitutes series compensation topology on the Rx side, can achieve an independent load voltage U_o that remains unaffected by variations in the load resistance R_L . Thus, the system can obtain an output characteristic of constant voltage (CV) (Darvish et al., 2021). Switches S_{pi} (i=1,2,3,4) added between the inverter and LCC compensation networks will be turned ON and OFF (activated or deactivated) depending on the position of the Rx coil, an approach known as segmented control (Li et al., 2019). This will be further discussed in Chapter 4.

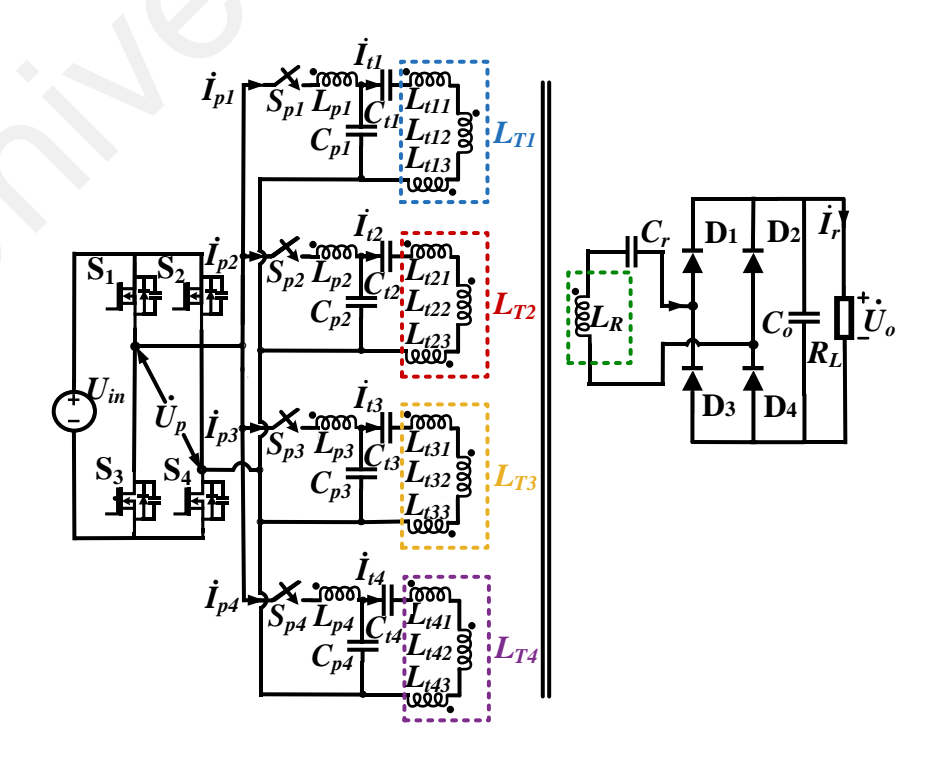


Figure 3.7: Configuration of the proposed DIWC system

3.6.2 Circuit modeling

In this part, a circuit analysis considering coil AC resistances is conducted to the output characteristics of the DIWC system with three activated Tx segmented coils (T1, T2, and T3), as shown in Figure 3.8. The primary voltage phasor of the full-bridge inverter can be represented as (3.9). The equivalent resistances of rectifier R_{Lrec} can be represented as (3.10).

$$\dot{U}_p = \frac{4\dot{U}_{in}}{\sqrt{2}\pi} \angle 0^\circ \tag{3.9}$$

$$R_{Lrec} = \frac{8R_L}{\pi^2} \tag{3.10}$$

Several variables used for the system analysis are expressed in (3.11) (i=1,2,3).

$$ZL_{pi} = j\omega L_{pi} \quad ZL_{Ti} = j\omega L_{Ti} \quad ZL_{R} = j\omega L_{R}$$

$$ZC_{pi} = \frac{1}{j\omega C_{pi}} \quad ZC_{ti} = \frac{1}{j\omega C_{ti}} \quad ZM_{TiR} = j\omega M_{TiR}$$

$$ZM_{TIT2} = j\omega M_{TIT2} \quad ZM_{TIT3} = j\omega M_{TIT3} \quad ZM_{T2T3} = j\omega M_{T2T3}$$
(3.11)

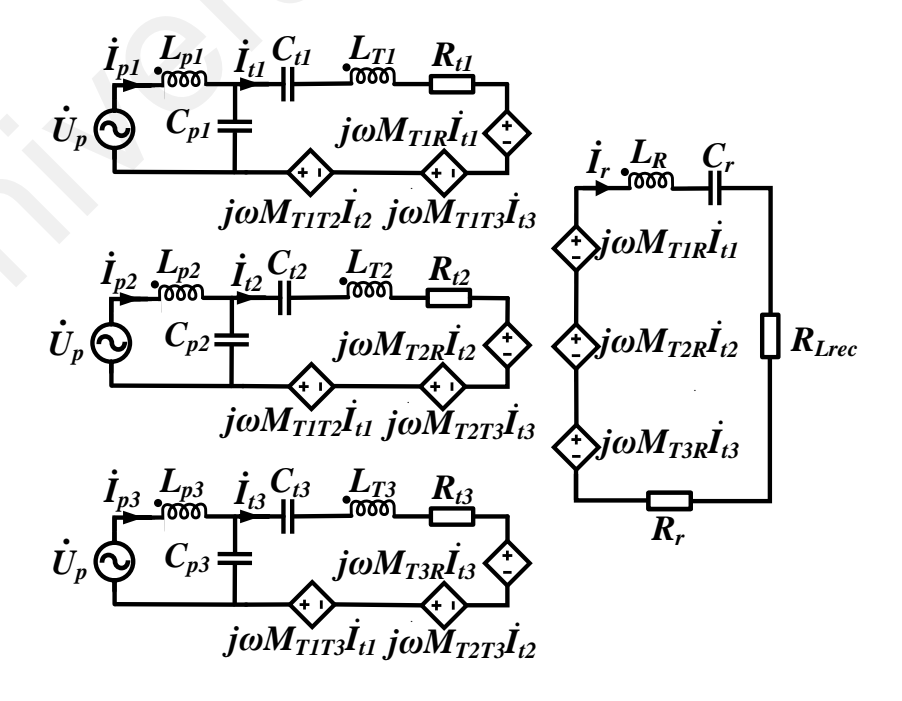


Figure 3.8: AC equivalent circuit with resistances

Based on equation (3.11), the Kirchhoff voltage law equations can be expressed in (3.2). R_{ti} is the AC resistance of the T*i* coils (where, i=1,2,3). R_r is the AC resistance of the Rx.

$$\begin{bmatrix} \dot{U}_{p} \\ \dot{U}_{p} \\ \dot{U}_{p} \\ 0 \\ 0 \\ 0 \\ 0 \end{bmatrix} = \begin{bmatrix} (ZL_{p1} + ZC_{p1})\dot{I}_{p1} - ZC_{p1}\dot{I}_{t1} \\ (ZL_{p2} + ZC_{p2})\dot{I}_{p2} - ZC_{p2}\dot{I}_{t2} \\ (ZL_{p3} + ZC_{p3})\dot{I}_{p3} - ZC_{p3}\dot{I}_{t3} \\ -ZC_{p1}\dot{I}_{p1} + (ZL_{T1} + ZC_{t1} + ZC_{p1} + R_{t1})\dot{I}_{t1} - ZM_{t1t2}\dot{I}_{t2} - ZM_{t1t3}\dot{I}_{t3} + ZM_{T1R}\dot{I}_{r} \\ -ZC_{p2}\dot{I}_{p2} + (ZL_{T2} + ZC_{t2} + ZC_{p2} + R_{t2})\dot{I}_{t2} - ZM_{t1t2}\dot{I}_{t1} - ZM_{t2t3}\dot{I}_{t3} + ZM_{T2R}\dot{I}_{r} \\ -ZC_{p3}\dot{I}_{p3} + (ZL_{T3} + ZC_{t3} + ZC_{p3} + R_{t3})\dot{I}_{t3} - ZM_{t1t3}\dot{I}_{t1} - ZM_{t2t3}\dot{I}_{t2} + ZM_{T3R}\dot{I}_{r} \\ ZM_{T1R}\dot{I}_{t1} + ZM_{T2R}\dot{I}_{t2} + ZM_{T3R}\dot{I}_{t3} + (R_{Lrec} + R_{r} + ZL_{R} + ZC_{r})\dot{I}_{r} \end{bmatrix}$$

$$(3.2)$$

To eliminate reactive power and increase power transfer capability, the system should operate near the ZPA condition. The capacitor values meeting the resonant condition for each loop are shown in equation (3.3)

$$C_{pi} = \frac{1}{\omega^{2} L_{pi}} \qquad C_{r} = \frac{1}{\omega^{2} L_{r}}$$

$$C_{t1} = \frac{1}{\omega^{2} (L_{T1} - L_{p1} + M_{a})} \qquad C_{t3} = \frac{1}{\omega^{2} (L_{T3} - L_{p3} + M_{c})}$$

$$C_{t2} = \frac{1}{\omega^{2} (L_{T2} - L_{p2} + M_{b})}$$
(3.3)

Where M_a , M_b , and M_c are given by

$$M_{a} = M_{T1T2} + M_{T1T3}$$

$$M_{b} = M_{T1T2} + M_{T2T3}$$

$$M_{c} = M_{T1T3} + M_{T2T3}$$
(3.4)

By substituting equations (3.3) and (3.4) into equation (3.2), the current in each loop can be derived as follows.

$$\left|\dot{I}_{ii}\right| = \frac{4}{\sqrt{2\pi\omega L_{ni}}} \left|\dot{U}_{in}\right|, \quad i = 1, 2, 3$$

$$\left|\dot{I}_{r}\right| = \frac{4}{\sqrt{2\pi}(R_{Lrec} + R_{r})} \left(\frac{M_{T1R}}{L_{p1}} + \frac{M_{T2R}}{L_{p2}} + \frac{M_{T3R}}{L_{p3}}\right) \left|\dot{U}_{in}\right| \tag{3.5}$$

$$\left|\dot{I}_{pi}\right| = \frac{4M_{TiR}}{\sqrt{2\pi L_{pi}(R_{Lrec} + R_{r})}} \left| \left(\frac{M_{T1R}}{L_{p1}} + \frac{M_{T2R}}{L_{p2}} + \frac{M_{T3R}}{L_{p3}} \right) - \frac{R_{ti}}{\omega^{2} L_{pi}^{2}} \right| \dot{U}_{in} \right|$$

In equation (3.5), given that the input voltage U_{in} and the frequency are fixed, the self-inductances of L_{p1} , L_{p2} , and L_{p3} are designed to be identical to ensure constant currents in each loop of the transmitter coils $I_{t1} = I_{t2} = I_{t3}$ (Li et al., 2019). Consequently, by solving I_r in (3.5), the output voltage U_o and output power P_o can be represented as

$$\left|\dot{U}_{O}\right| = \left|\dot{I}_{r}\right| R_{Lrec}, \quad P_{O} = \left|\dot{I}_{r}\right| * \left|\dot{U}_{O}\right| \tag{3.6}$$

Similarly, from (3.5), the input power P_{in} can be derived as

$$P_{in} = \left(\left| \dot{I}_{p1} \right| + \left| \dot{I}_{p2} \right| + \left| \dot{I}_{p3} \right| \right) * 4 \dot{U}_{in} / \left(\sqrt{2}\pi \right)$$
(3.7)

Eventually, according to (3.9)-(3.7), the efficiency can be derived as (3.8).

$$\eta = \frac{R_{Lrec} \left| W_{1} Z M_{T1R} + W_{2} Z M_{T2R} + W_{3} Z M_{T3R} \right|^{2}}{\left(R_{Lrec} + R_{r} \right) \left| W_{1} Z M_{T1R} + W_{2} Z M_{T2R} + W_{3} Z M_{T3R} \right|^{2} - \left(R_{Lrec} + R_{r} \right)^{2} \left| W_{1}^{2} R_{r1} + W_{2}^{2} R_{r2} + W_{3}^{2} R_{r3} \right|}$$

$$(3.8)$$

Where, W_i is given by:

$$W_i = 1/ZL_{ni} = 1/ZC_{ni}, \quad i = 1, 2, 3$$
 (3.9)

3.7 Experimental Prototype

3.7.1 Magnetic coupler

Four segmented Tx coils, including Ti coils (i=1,2,3,4), are constructed in the setup as portrayed in Figure 3.9. This is because four segmented Tx coils with the switching actions can be regarded as a typical unit during the Rx movement process, which is sufficient to experimentally verify the dynamic performance of the proposed magnetic coupler. AWG 38,800 strands of Litz wire with a wire diameter of 0.45cm are utilized to make a magnetic coupler and resonant inductor. The values of self-inductances and mutual inductances are measured using the GWINSTEK-8210 LCR meter, which is suitable for testing the system frequencies below 1MHz.

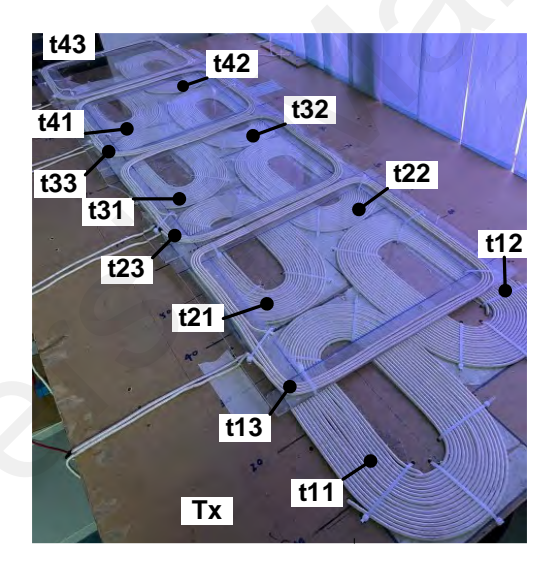


Figure 3.9: Proposed Tx structure

3.7.2 Circuit design

The circuit design, as illustrated in Figure 3.10, follows the schematic presented in Figure 3.7. The values of compensated capacitor C_{pi} , C_{ti} (i=1,2,3,4) are measured by the LCR meter; several resonant film capacitors with a low dissipation factor are selected to reduce reactive power caused by the compensated components and to maximize the parameters of system efficiency as much as possible. The detailed proposed DIWC system is listed in Table 3.2 and Table 3.3. A full-bridge inverter containing four SiC

MOSFETs (C2M0080120D) is used on the primary side. The full-bridge rectifiers consist of four fast-recovery diodes. An electronic load is connected to the rectifier as its load. YOKOGAWA WT500 power analyzer measures the DC-DC efficiency η and output voltage U_o .

For the experimental parameter setting, the primary parameter setting shown in Section 3.3 is implemented. The value of compensated inductors L_{pi} (i=1,2,3) should be identical and configured as 31 μ H. Thus, the theoretical value of mutual inductance M_{3TR} is 32.7 μ H, according to (Li et al., 2019). This value met the requirement of desired mutual inductance M_s . The load resistance R_L is 20 Ω when the setup is tested to evaluate its dynamic performance along both the Y and X directions.

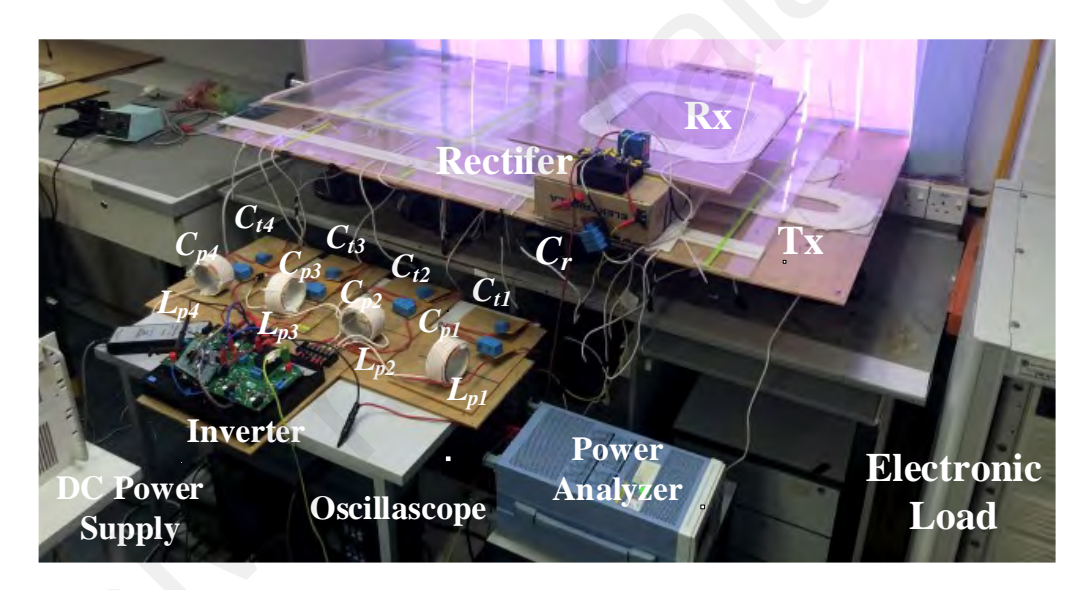


Figure 3.10: Experimental Prototype

Table 3.3: Experimental Prototype Parameters

Parameter	Value	Parameter	Value	Parameter	Value`		
L_{T1}	164.81µH	L_{p1}	31.3μΗ	C_{p1}	112.01nF		
L_{T2}	164.55μΗ	L_{p2}	31.3µH	C_{p2}	112.01nF		
L_{T3}	164.25μΗ	L_{p3}	31.3µH	C_{p3}	112.03nF		
L_{T4}	164.44μΗ	L_{p4}	31.3µH	C_{p4}	112.01nF		
L_R	165.14μΗ	C_{t1}	26.3nF	C_{t2}	26.3nF		
C_{t3}	26.3nF	C_{t4}	26.3nF	C_{t2}	20.85nF		
C_r	22.4nF	R_{T1}	0.15Ω	R_{T2}	0.17Ω		
R_{T3}	0.15Ω	R_{T4}	0.15Ω	R_r	0.1Ω		
R_L	20Ω						

3.8 Summary

In this chapter, a new cross-overlapped coil structure is proposed and thoroughly analyzed. This design, which integrates the characteristics of both crossed and overlapped coil structures, is compared with existing DIWC magnetic couplers using a single Tx coil. Additionally, simulations using ANSYS Maxwell are conducted to analyze methods for achieving decoupling on the Tx side and reducing mutual inductance fluctuations on the Rx side. The design procedures for the proposed DIWC magnetic coupler are outlined and explained in detail. Moreover, the DIWC system incorporating multiple Tx coils is analyzed using the FHA method, and the experimental configuration is also detailed. It can be concluded that the proposed structure shows preliminary superiority in achieving decoupling, reducing mutual inductance fluctuations and optimized efficiency. Simulated and experimental results will be presented in Chapter 4 to validate the speculations discussed here.

CHAPTER 4: RESULTS AND DISCUSSIONS

4.1 Introduction

To validate the findings of the proposed DIWC magnetic coupler discussed in Chapter 3, a scaled-down experimental prototype was constructed. This prototype features the DIWC magnetic coupler with four segmented Tx coils, and is used to evaluate both static and dynamic performance. The mutual inductance between Tx coils and the single Rx coil is assessed by varying Rx coil's relative position to Tx coils. Moreover, this chapter presents experimental evaluations of load voltage and transfer efficiency at various Rx positions. Additionally, it examines the system's performance under longitudinal misalignment and varying load conditions. In the discussion section, results from the experimental setup are presented to compare the proposed DIWC magnetic coupler with existing models. The effectiveness of the newly introduced cross-overlapped coil structure is demonstrated in mitigating mutual inductance fluctuations, achieving both high efficiency and effective decoupling between segmented coils simultaneously.

4.2 Simulated Result

4.2.1 Mutual inductance between adjacent Tx coils M_{T1T2}

Since the segmented coils in the Tx are identical in size, the mutual inductance between adjacent coils is equivalent. Consequently, the mutual inductance between coils T1 and T2 serves as a representative measure for the mutual inductance of neighboring Tx coils. Table 4.1 shows the mutual inductances between T1 and T2 coils, mentioned in (3.2). When the number of turns N_{t3} is set to 4, the total mutual inductance between the adjacent T1 and T2 coils, labeled as M_{T1T2} , equals -1.2 μ H. This results in a coupling coefficient of only -0.007, which can be considered negligible according to (Li et al., 2019; Liu et al., 2023). Therefore, N_{t3} has been chosen as 4 in this paper. However, if N_{t3} is increased to 5 turns, M_{T1T2} becomes only -10nH, further reducing the coupling to as

low as 0.00006, suitable for applications requiring more precise decoupling. Other Tx coil parameters that can satisfy the (3.3) are shown in Table 4.1.

Table 4.1: Simulation values of the mutual inductances between adjacent Tx segmented coils (when N_{t3} =4)

Symbol	Value	Symbol	Value	Symbol	Value
M_{t11t21}	-1.99µH	M_{t12t21}	-1.85µH	M_{t13t21}	8.74μΗ
M_{t11t22}	-0.36µH	M_{t12t22}	-1.99µH	M_{t13t22}	1.12μΗ
M_{t11t23}	-0.26µH	M_{t12t23}	-0.53μH	M_{t13t23}	-2.89µH

4.2.2 Mutual inductance between activated Tx coils and Rx M_{3TR}

4.2.2.1 M_{3TR} in Y direction

The length of Rx coils along Y direction l_{rl} is chosen as 42cm in Figure 4.5, which will be further discussed in the Section 4.2.4. By establishing the simulation model in the ANSYS Maxwell, it can be easily found that both M_{TlR} and M_{T2R} experience significant fluctuations, as shown in Figure 4.1, while the Rx coil moves along the Y direction from y = -66cm to y = 108cm as depicted in Figure 3.6. This fluctuation will cause the output voltage on the Rx side to vary. As illustrated in Figure 4.1, when M_{TlR} reaches its maximum value, M_{T2R} drops to zero. Conversely, when M_{T2R} reaches its peak value, M_{TlR} diminishes to zero. The same variation trend also exists between mutual inductances of M_{T2R} and M_{T3R} . Considering this situation, by activating the T1, T2, and T3 coils simultaneously, a relatively stable mutual inductance can ultimately be attained, as shown in the green curve of Figure 4.1. It can be observed that the variation trend of the mutual inductance M_{3TR} between the Rx positions of y = 0cm and y = 36cm is much more stable than M_{T1R} , M_{T2R} , and M_{T3R} .

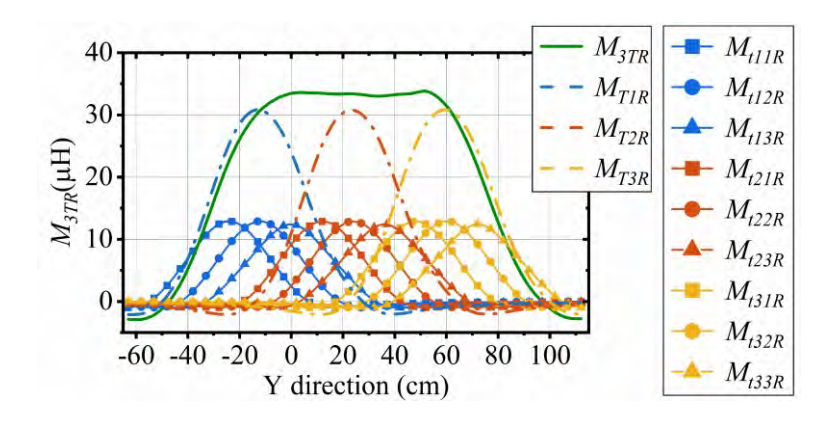


Figure 4.1: The M_{3TR} variation curve when crossed ratio z = (1/3) %;

4.2.2.2 M_{3TR} with different crossed ratio z

Designing the cross-overlapped Tx coil with different ratio values leads to various trends of mutual inductance, as presented in Figure 4.2. These different ratios will affect the length of the single cross-overlapped Tx coil along the Y direction. When the ratio z is more than or equal to 50%, the ti3 coils will not partially overlap with ti1 and ti2 coils (i=1, 2, 3), and the proposed magnetic coupler will lose the characteristics of an overlapped structure, which has been discussed in the Section 3.4. Therefore, various ratios ranging from 0% to 50% have been analyzed, as shown in Figure 4.2. Furthermore, as the cross-ratio of Tx coil groups increases, it can be concluded that the proposed one with the cross-ratio z set between z0 to z0 exhibits better mutual inductance stability in the DIWC system, as described in this paper. Therefore, A cross ratio of z1 is applied in this paper to achieve a relatively constant mutual inductance that can be achieved as the Rx coil travels along the Tx coils in the Y direction.

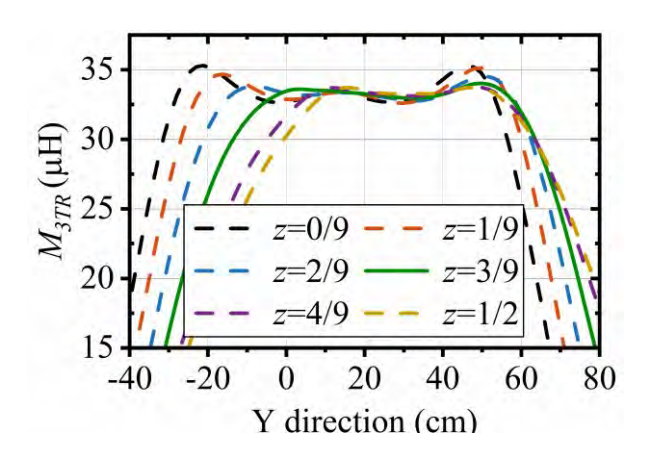


Figure 4.2: M_{3TR} variation curves with different crossed ratio z;

4.2.2.3 M_{3TR} in X direction

The longitudinal misalignment (X direction) performance of the proposed system is discussed in this section by analyzing the M_{3TR} variation as the Rx moves along the Y-axis, as illustrated in Figure 4.3. It can be observed that in cases of positive and negative X-misalignment, using a single transmitter group, such as T1, results in asymmetric mutual variation M_{T1R} due to the inherent design of the proposed one. This leads to poorer longitudinal misalignment tolerance compared to existing symmetric Q coil structures, as mentioned in (F. Lu et al., 2016). However, this asymmetric mutual fluctuation along the X-axis can be addressed in the proposed system by activating more than a single group of Tx coils. Since we are using three sets of Tx coils, the total mutual inductance variation of M_{3TR} (M_{T1R} and M_{T2R}) demonstrates naturally symmetric performance, as clearly indicated in Figure 4.3. This shows that the mentioned issues have been addressed.

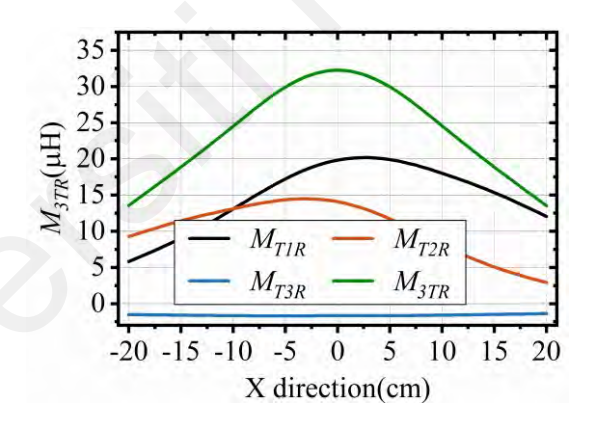


Figure 4.3 M_{3TR} variation along the X direction (when Rx positioned at y=0cm) 4.2.3 The selection of the control method for segmented Tx coils.

In the lumped track coil type of DIWC system, the Rx coil mainly couples with the nearby Tx coils. Therefore, a suitable coil segmented control method is required, and it involves the proper turning OFF Tx coils that are further from the Rx coil and turning ON Tx coils that are close to the Rx coil using switches S_{pi} (i=1,2,3,4). This method can reduce EMI, enhance power transfer efficiency, and simultaneously improve mutual inductance fluctuations (Cai et al., 2022; X. Li et al., 2020; Li et al., 2019; Xiang et al., 2018). Two

more segmented Tx coils (T4 and T5) are introduced in Figure 4.4, represented in purple, and grey respectively. Ti (ON) and Ti (OFF) respectively represent whether the switch S_{pi} is closed or open. Furthermore, a relatively stable mutual inductance can be obtained between three turned-ON Tx coils and the Rx coil, as presented in Figure 4.1. Thus, when the Rx coil moves along the Tx described in Figure 4.4, a segmented control method using only three turned-ON segmented Tx coils simultaneously is employed in the proposed DIWC system to ensure that the output performance of the system remains effectively stable. The general order in which the Tx coil group should be turned ON is shown in Figure 4.4 if more than three sets of Tx groups need to be used.

From Figure 4.1, it can be observed that the mutual inductance drop of M_{3TR} exists when y < 0cm. Thus, the zero point "O" (y=0cm) is chosen as the starting position of the Rx movement. In addition, starting from y=0cm, whenever the Rx coil moves a specific distance l_c along the Y-axis, specific segmented Tx coils need to be turned ON or OFF. Therefore, due to the need for simplifying the analysis and the stable mutual inductance obtained from the position of y=0cm to y=36cm depicted in Figure 4.1, the specific distance l_c is set to be equal to the length of a single ti1, ti2, or ti3 coil, denoted as l_t .

The effect of EV moving speed on segmented coil control and the response time of the position detection sensor are ignored in this paper. This is intended to focus on verifying the feasibility of the DIWC magnetic coupler proposed in this paper while the factors mentioned above are beyond the scope of this study. Li et al. (2019) proposes a method that alternately employs three-coils and four-coils segmented control to consistently maintain stable mutual inductance between Tx and Rx. However, this approach increases the complexity of coil control and is unsuitable for high-speed EV applications. In contrast, the segmented coil control method proposed in this study achieves stable mutual inductance while utilizing only a single three-coil control strategy. This simplified control

approach is more advantageous for implementing the proposed coil structure in higherspeed EV applications. (Li et al., 2019).

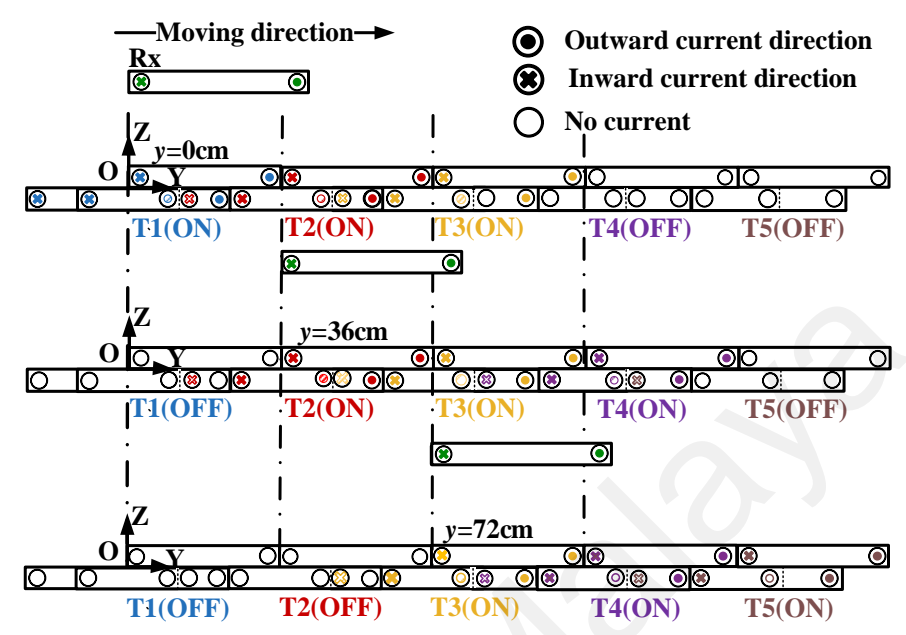


Figure 4.4: Timing of switching action with changed Rx position at Y direction (Rx length l_{rl} =42cm)

4.2.4 Rx coil turns N_r and coil length l_{rl} optimization

A stable M_{3TR} should be guaranteed when the Rx coil moves along the Tx coils in the Y-direction, as depicted in Figure 4.4. It is effective to maintain the width of the Rx coil (l_{rv}) constant and properly extend the length of the Rx coil (l_{rl}) , aiming to minimize the mutual inductance fluctuations caused during the movement of the Rx coil. This approach has been verified for its feasibility in previous research (F. Lu et al., 2016). This work adopts the same approach to suppress mutual inductance fluctuations. Therefore, the objective is to minimize mutual inductance fluctuations by appropriately extending the Rx coil, while maximizing the coupling coefficient k_{TR} . This method is also known as the traversal method by ANSYS Maxwell, which helps to enhance the efficiency of the DIWC system by considering the Rx coil turns as an important variable as well (Li et al., 2019). The coil parameters of the proposed magnetic coupler are followed in Table 3.1.

The number of coil turns N_{tI} and N_{t2} is set to 16. According to previous simulation results of Tx side, the number of coils turns N_{t3} is set to 4. Figure 4.5 illustrates the variation in the value of M_{3TR} with changes in the Y-direction position of Rx based on different values of the Rx coil length l_{rl} when $N_r = 16$. Figure 4.6 presents the changes in coupling coefficient with different Rx coil turns N_r and length l_r when the Rx is positioned at y = 0cm. It can be observed that the fluctuations of mutual inductance can be minimized when the Rx coil length l_{rl} is chosen as 42cm, which is controlled within 1%. The coupling coefficient k_{TR} can be maximized when the Rx coil turns N_r is set as 16.

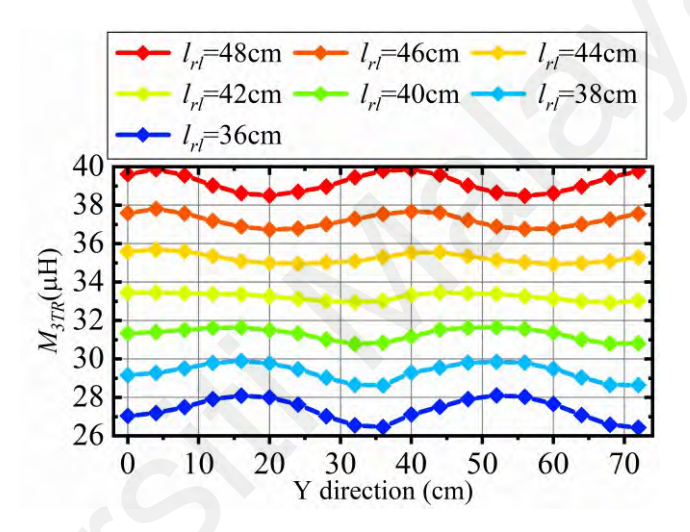


Figure 4.5: The M_{3TR} variation with changed Rx Y-direction position and different values of the Rx coil length l_{rl} . (when $N_r=16$);

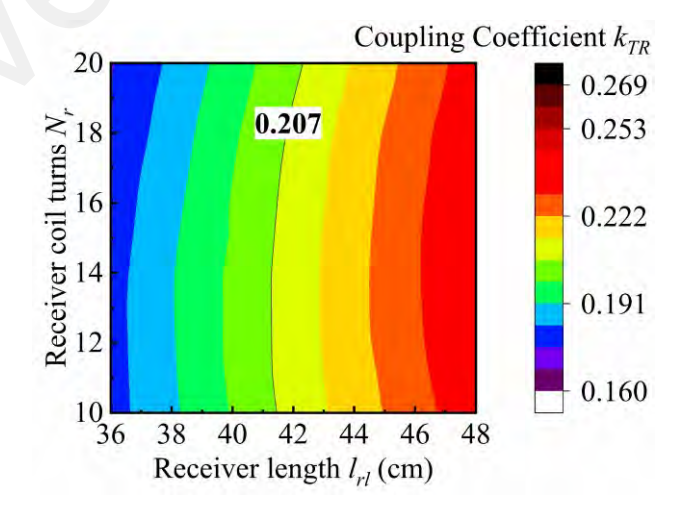


Figure 4.6: Temperature contour map of coupling coefficient k_{TR} (when Rx position at y=0cm)

4.3 Experimental Results

4.3.1 Load R_L and efficiency η

The transfer efficiency and the output voltage variation of the proposed system concerning the load resistance are shown in Figure 4.7, when the Rx coil is positioned at y = 0cm. The maximum DC-DC efficiency is recorded at 92.87% when R_L =17.2 Ω .

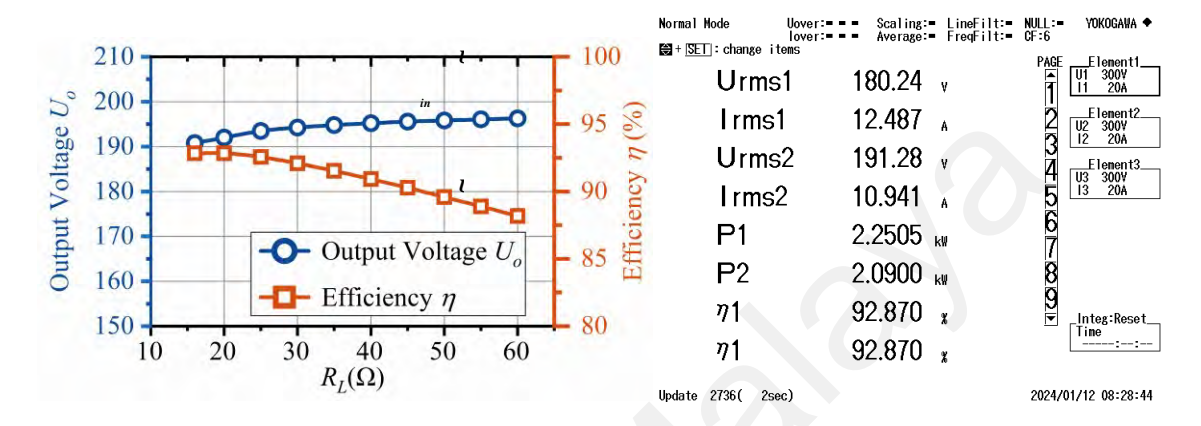


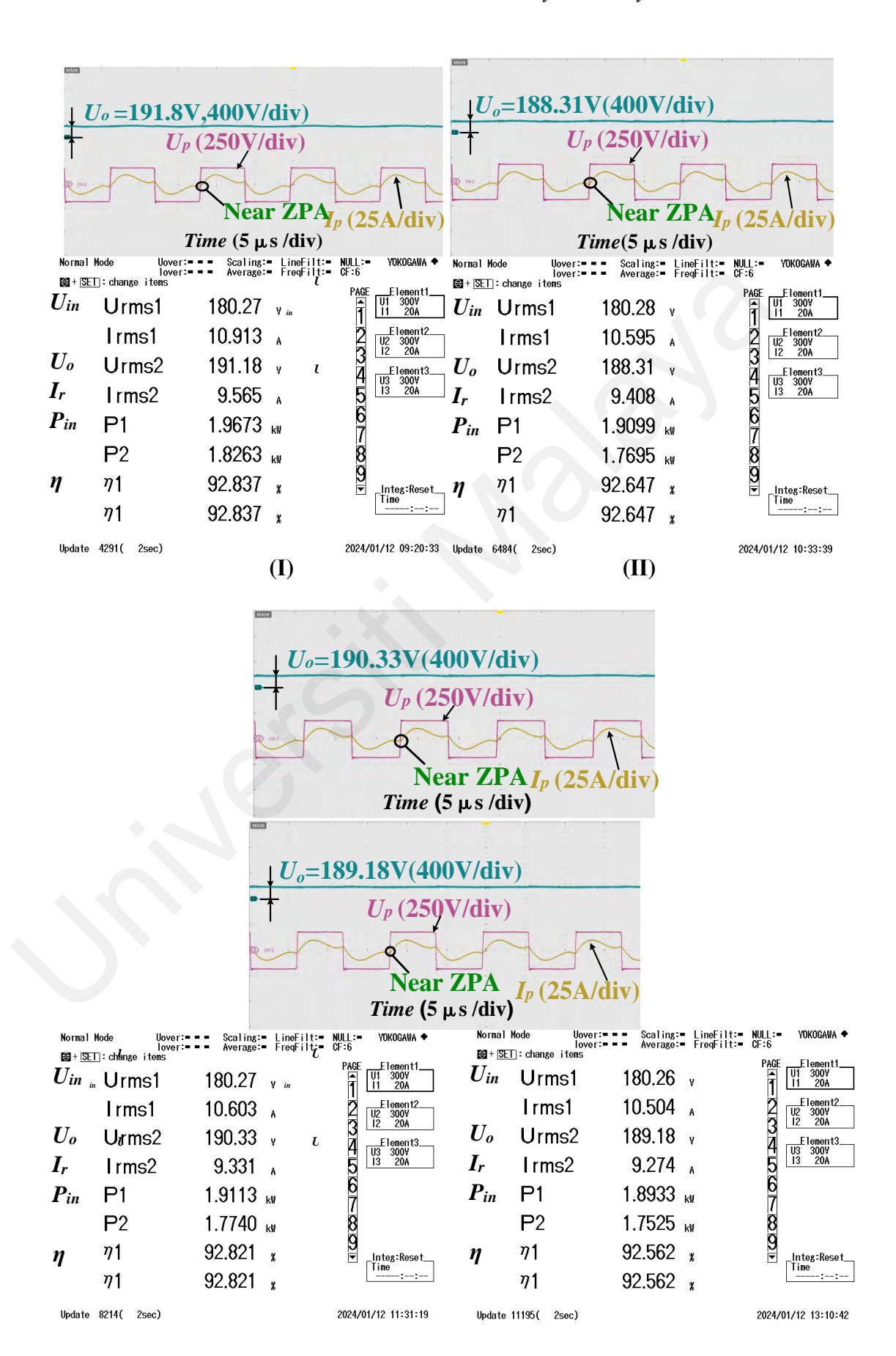
Figure 4.7: Relationship between load resistance R_L and system efficiency η (y=0cm)

4.3.2 Output voltage U_0 and efficiency η in Y direction (x=0cm)

Figure 4.8 presents output voltage U_o , inverter voltage U_p , and current I_p waveforms of the DIWC system, along with corresponding power analyzer images, when the Rx coil is at different positions along the Y direction. According to Figure 4.8, when the Rx coil is positioned at y=0 or 18cm, only the T1, T2, and T3 coil is turned ON. When the Rx coil is positioned at y=36cm, 54cm, only the T2, T3, and T4 coils are turned ON. It can be concluded that the system can reach near-ZPA (Zero phase Angle) input, which mainly supplies active power. Furthermore, it also achieves ZVS (Zero Voltage Switching), thereby reducing power loss.

When the Rx coil moves above the Tx coils in the Y direction, the output voltage U_o and the DC-DC efficiency are shown in Figure 4.9. Considering the fluctuations caused by fabrication error, both DC-DC efficiency and output voltage are approximately the same as the variation trend of the simulated M_{3TR} presented in Figure 4.5, indicating that the fabricated DIWC system with CV characteristics works efficiently. Moreover, the

output voltage fluctuation is controlled within $\pm 1\%$, and the DC-DC efficiency remains stable at around 92% when the Rx coil is moved from y=0cm to y=72cm.



(III) (IV)

Figure 4.8: U_p , I_p , and U_o waveforms and power analyzer images at different Rx positions along Y-direction. (I) y=0cm. (II) y=18cm. (III) y=36cm. (IV) y=54cm.

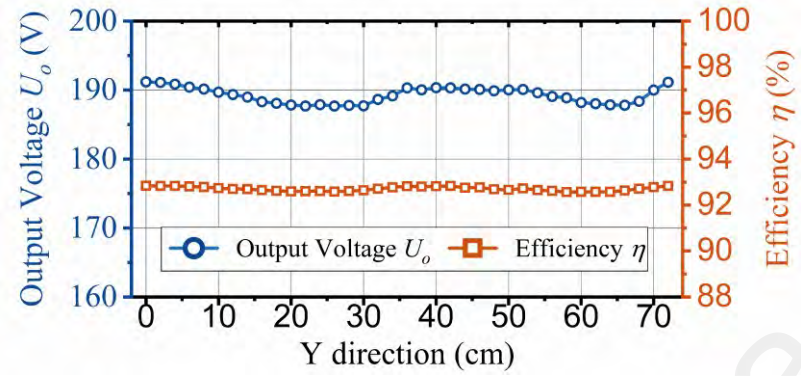


Figure 4.9: Efficiency and output voltage along Y direction from y=0cm to y=72cm (x=0cm)

4.3.3 Output voltage U_o and efficiency η in Y direction at different X-direction positions ($x=\pm 4$ cm, ± 10 cm)

The performance of Y-direction efficiency and output voltage performance with different X-direction position ($x=\pm 4$ cm and ± 10 cm) is also analyzed in this paper, as illustrated in Figure 4.10. The output voltage U_o decreases when the Rx coil offsets along the X-direction, but the system efficiency can be maintained above 90% within an offset distance of ± 10 cm. Furthermore, similar output voltage and efficiency performance can be achieved with the same offset distance in both the positive and negative X-directions. It can be concluded that, due to multi-coil segmented control, the asymmetrical design of the proposed segmented Tx coil does not lead to significant differences in the system's output characteristics in both positive and negative X-directions.

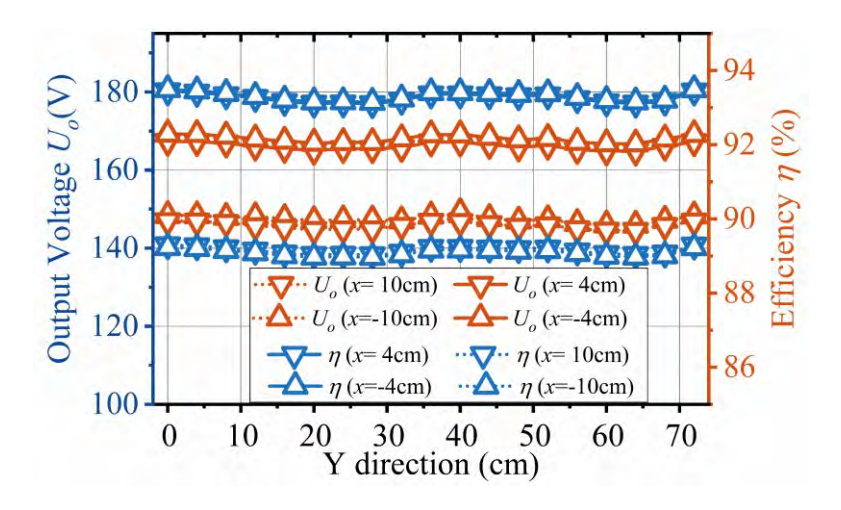


Figure 4.10: Y-direction efficiency and output voltage performance with different X-direction positions ($x=\pm 4$ cm, ± 10 cm)

4.4 Comparison with Other Existing DIWC Magnetic Couplers

Table 4.2 presents a comparison between the proposed DIWC magnetic coupler and previous works aimed at achieving decoupling, reduced mutual inductance fluctuation, and higher efficiency. In contrast to the mixed structure of Q and DD coils used at either the Tx (Li et al., 2019) or Rx (X. Li et al., 2020), this paper maximizes utilization of Tx or Rx coils to save coil costs. Additionally, as opposed to the structure solely using DD coils (Liu et al., 2022; Lv et al., 2020), this paper proposes a new magnetic coupler composed of multi-Q coils to completely avoid the power null problem that exists in the DD coil. Compared to magnetic coupler solely using Q coils, as well as in contrast with other works presented in Table 4.2, the proposed structure achieves reduced mutual inductance fluctuation (±1% output voltage fluctuation), higher transfer efficiency (maximum efficiency 92.87%), while achieving decoupling between adjacent Tx coils.

Table 4.2: Comparison with other DIWC magnetic couplers

DIWC Magne tic Couple r	Coupl ing betwe en TX adjace nt coils	Tx coils size	Tx Self- Induct ance (μH)	Rx coils size	Rx Self- induct ance (μH)	Airg ap (cm	Power Capab ility (kW)	Maxi mum Efficie ncy (%)	Fluctua tion	Ferr ite Usa ge	Maxi mize the Tx or Rx coils
(Li et al., 2019)	Elimi n- ating	Q or DD : 20 cm×40 cm	Q: 95 DD: 120	Q and DD :20cm×40c m	232.0 6	10	0.384	90.37	V: ±2%	Yes	Tx: Yes Rx: No
(X. Li et al., 2020)	Elimi n- ating	Q and DD Q: 50 cm×50 cm DD: 10cm×20cm.	64 or 73	Q:50cm×50 cm	58	10	0.259	90	V: ±2.5%	Yes	Tx: No Rx: Yes
(Liu et al., 2017)	Elimi n- ating	DD: 10 cm×20c m	62.7 or 145.8	DD: 20 cm×40 cm	87.55	4	0.6	90.4	The max output voltage error is 4.72%	Yes	Tx: No Rx: Yes
(Liu et al., 2022)	Elimi n- ating	DD: 28cm×56 cm	282	DD:50.4cm ×56cm	521.3 2	16	0.43	83.05	P: ±1.52%	Yes	Tx: Yes Rx: Yes
(Cai et al., 2022)	Elimi n- ating	Q: 30 cm×50 cm	192.9 7	Q: 7.5 cm (radius)	60.77	5	0.167	87	V: ±2%	Yes	Tx: Yes Rx: Yes
(F. Lu et al., 2016)	Exist ing	Q: 40cm×38 .8cm	62.5	Q: 48.5cm×40 cm	105.4 6	15	1.4	89.78	P: ±7.5% (Middle part ±2.9%)	Yes	Tx: Yes Rx: Yes
(S. Li et al., 2020)	Elimi n- ating	Q: 27 cm×72 cm	93.29 8	Q: 27 cm×36 cm	231.7	10. 5	1.2	85	P: ±6%	Yes	Tx: Yes Rx: Yes
(Zhou et al., 2024)	Elimi n- ating	Q: 30 cm×30 cm	147.8 3	Q: 30 cm×33 cm	83 and 71	5	0.939	93.07	V: ±3.39 %	Yes	Tx: Yes Rx: Yes

Propo sed	Elimi n- ating	Q: 36 cm×42 cm or Q:36 cm×21cm	164	Q: 42 cm×42 cm	165	12	2	92.87	V: ±1%	No	Tx: Yes Rx: Yes	
--------------	----------------------	--------------------------------------	-----	-------------------	-----	----	---	-------	-----------	----	--------------------	--

4.5 Summary

In this chapter, simulated results are presented to prove the effectiveness of the proposed DIWC magnetic coupler. A 2kW experimental prototype has been developed to validate the multiple advantages of the proposed DIWC magnetic coupler, including effective decoupling, reduced mutual inductance fluctuations, and optimized efficiency. The experimental results demonstrate that output voltage fluctuations are maintained within $\pm 1\%$. The DC-DC efficiency remains around 92% during Rx movement in the Y direction and stays above 90% within a ± 10 cm longitudinal offset, with a maximum DC-DC efficiency of 92.87%. A comparative analysis with other existing DIWC magnetic couplers is also presented. The conclusions of the thesis and directions for future work will be discussed in the next chapter.

CHAPTER 5: CONCLUSION

5.1 Conclusion

In the conventional DIWC magnetic coupler designs, it is challenging to both minimize output voltage or power fluctuations during EV movement and eliminate cross-coupling between adjacent segmented Tx coils while achieving high system efficiency. Traditional overlapped coil structures are designed to enhance the magnetic field between the Tx and Rx. However, this design also increases cross-coupling effects between adjacent Tx coils. Conversely, traditional crossed-coil structures aim to reduce output fluctuations in DIWC systems, but they can also lead to decreased efficiency due to increased magnetic field leakage.

This work proposes a new DIWC magnetic coupler, consisting of cross-overlapped Tx and single Rx coils, with multiple purposes. The main goal is to simultaneously address the issues existing in the DIWC system, such as mutual inductance fluctuation, the unwanted cross-coupling between adjacent segmented Tx coils, and efficiency optimization. Additionally, this paper discusses the comparison analysis between magnetic couplers consisting solely of DD or Q coils and those with a mixed structure of DD and Q coils. It addresses the challenges of maximizing the use of Tx or Rx coils to reduce coil fabrication costs, improving performance in longitudinal misalignment, and addressing the power null point issue occurring with DD coils. A 2kW prototype is constructed to validate the proposed DIWC magnetic coupler. Experimental results indicate that the DIWC system, utilizing the proposed magnetic coupler, can maintain output voltage fluctuation within ±1%. The DC-DC efficiency is sustained around 92% during Rx movement in the Y direction and remains above 90% within ±10cm longitudinal offset. The maximum DC-DC efficiency achieved is 92.87%. Based on the comparison analysis with existing research, the proposed multifunctional magnetic coupler is successfully realized. In the future, a dual-receiver connected in parallel is

anticipated to replace single-receiver coils for high-power applications. Additionally, more cross-overlapped segmented Tx coils are expected to be activated simultaneously for high-speed EV applications. To reduce coil material costs and explore broader applications of this proposed magnetic coupler, ferrite bars and aluminum plates may also be incorporated into the Tx and Rx designs.

5.2 Limitations of the Research

Based on the aforementioned results, while the proposed DIWC magnetic coupler demonstrates excellent performance, its limitations are also highlighted and summarized as follows.

- 1. Implementing the single Tx of the proposed DIWC magnetic coupler requires an excessive amount of Litz wire for coil fabrication, leading to increased construction costs.
- 2. Each Tx in the proposed DIWC magnetic coupler consists of three coils connected in series. The series connection of multiple coils leads to an increase in the internal resistance of the coil, resulting in higher power losses within the system.
- 3. The impact of EV speed is not considered in this study, which also influences the fluctuation of mutual inductance between the Tx and Rx coils. Additionally, due to experimental constraints and the high cost of ferrite materials, ferrite was not incorporated into the experimental setup. Its inclusion could further enhance efficiency.

5.3 Future Works

Several future tasks, listed below, can be pursued:

- 1. The single Rx coil used in the proposed magnetic coupler can be replaced by multiple receivers connected in parallel. It aims to investigate the performance of the proposed cross-overlapped Tx coil structure in higher-power applications.
- 2. More cross-overlapped segmented Tx coils can be activated to investigate the performance of cross-overlapped Tx coil structures in high-speed applications of EVs.

3. Ferrite bars and aluminum plates can be incorporated into the proposed DIWC magnetic coupler to reduce the usage of Litz wire and electromagnetic interference.

REFERENCES

- Ahmad, A., Alam, M. S., & Chabaan, R. (2017). A comprehensive review of wireless charging technologies for electric vehicles. *IEEE Transactions on Transportation Electrification*, 4(1), 38-63.
- Ahmad, A., Alam, M. S., & Chabaan, R. (2018). A Comprehensive Review of Wireless Charging Technologies for Electric Vehicles. *IEEE Transactions on Transportation Electrification*, 4(1), 38-63.
- Ahson, S. A., & Ilyas, M. (2017). *RFID handbook: applications, technology, security, and privacy*. CRC press.
- Arakawa, T., Goguri, S., Krogmeier, J. V., Kruger, A., Love, D. J., Mudumbai, R., & Swabey, M. A. (2018). Optimizing wireless power transfer from multiple transmit coils. *IEEE Access*, 6, 23828-23838.
- Bolger, J. (1994). Urban electric transportation systems: The role of magnetic power transfer. *Proceedings of WESCON'94* (pp.41-45). IEEE,
- Bolger, J., Kirsten, F., & Ng, L. (1978). Inductive power coupling for an electric highway system. 28th IEEE vehicular technology conference (Vol. 28, pp. 137-144). IEEE.
- Bolger, J., Ng, L., Turner, D., & Wallace, R. (1979). Testing a prototype inductive power coupling for an electric highway system. 29th IEEE Vehicular Technology Conference (Vol. 29, pp. 48-56). IEEE.
- Bosshard, R., Kolar, J. W., Mühlethaler, J., Stevanović, I., Wunsch, B., & Canales, F. (2014). Modeling and Optimization of Inductive Power Transfer Coils for Electric Vehicles. *IEEE Journal of Emerging and Selected Topics in Power Electronics*, 3(1), 50-64.
- Boys, J. T., & Covic, G. A. (2014). IPT fact sheet series: no. 2 magnetic circuits for powering electric vehicles. *Department of Electrical and Computer Engineering, The University of Auckland, Auckland.*
- Boys, J. T., & Covic, G. A. (2015). The inductive power transfer story at the University of Auckland. *IEEE circuits and systems magazine*, 15(2), 6-27.
- Budhia, M., Boys, J. T., Covic, G. A., & Huang, C.-Y. (2011). Development of a single-sided flux magnetic coupler for electric vehicle IPT charging systems. *IEEE Transactions on Industrial Electronics*, 60(1), 318-328.

- Budhia, M., Covic, G. A., & Boys, J. T. (2011). Design and optimization of circular magnetic structures for lumped inductive power transfer systems. *IEEE Transactions on Power Electronics*, 26(11), 3096-3108.
- Buja, G., Bertoluzzo, M., & Dashora, H. K. (2016). Lumped Track Layout Design for Dynamic Wireless Charging of Electric Vehicles. *IEEE Transactions on Industrial Electronics*, 63(10), 6631-6640.
- Cai, C., Saeedifard, M., Wang, J., Zhang, P., Zhao, J., & Hong, Y. (2022). A Cost-Effective Segmented Dynamic Wireless Charging System With Stable Efficiency and Output Power. *IEEE Transactions on Power Electronics*, 37(7), 8682-8700.
- Campi, T., Cruciani, S., Maradei, F., & Feliziani, M. (2015). Magnetic shielding design of wireless power transfer systems. 2015 31st International Review of Progress in Applied Computational Electromagnetics (ACES) (pp.1-2), IEEE.
- Campi, T., Cruciani, S., Maradei, F., & Feliziani, M. (2021). Two-coil receiver for electrical vehicles in dynamic wireless power transfer. *Energies*, 14(22), 7790.
- Cardama, M., Cortez, A., Hosek, E., Krapp, A., Medimorec, N., & Yiu, A. (2023). SLOCAT Transport, Climate and Sustainability Global Status Report.
- Chen, W., Liu, C., Lee, C. H., & Shan, Z. (2016). Cost-effectiveness comparison of coupler designs of wireless power transfer for electric vehicle dynamic charging. *Energies*, 9(11), 906.
- Chigira, M., Nagatsuka, Y., Kaneko, Y., Abe, S., Yasuda, T., & Suzuki, A. (2011). Small-size light-weight transformer with new core structure for contactless electric vehicle power transfer system. 2011 IEEE Energy Conversion Congress and Exposition (pp. 260-266). IEEE.
- Choi, S. Y., Gu, B. W., Jeong, S. Y., & Rim, C. T. (2014). Advances in wireless power transfer systems for roadway-powered electric vehicles. *IEEE Journal of Emerging and Selected Topics in Power Electronics*, 3(1), 18-36.
- Covic, G., Boys, J., & Lu, H. (2006). A three-phase inductively coupled power transfer system. 2006 1ST IEEE Conference on Industrial Electronics and Applications (pp. 1-6). IEEE.
- Covic, G. A., & Boys, J. T. (2013). Modern Trends in Inductive Power Transfer for Transportation Applications. *IEEE Journal of Emerging and Selected Topics in Power Electronics*, *I*(1), 28-41.

- Covic, G. A., Kissin, M. L., Kacprzak, D., Clausen, N., & Hao, H. (2011). A bipolar primary pad topology for EV stationary charging and highway power by inductive coupling. 2011 IEEE energy conversion congress and exposition (pp. 1832-1838). IEEE.
- Cui, S., Song, B., Gao, X., & Dong, S. (2018). A narrow-width three phase magnetic coupling mechanism with constant output power for electric vehicles dynamic wireless charging. 2018 IEEE PELS Workshop on Emerging Technologies: Wireless Power Transfer (WoW) (pp. 1-6). IEEE.
- Cui, S., Song, B., & Wang, Z. (2022). Overview of magnetic coupler for electric vehicles dynamic wireless charging. *Trans. China Electrotech. Soc*, 37(3), 537-554.
- Darvish, P., Hossain, A., Mekhilef, S., Tey, K. S., Mubin, M. B., Yin, J., Akhtar, M. M., Mustafa, A., Khalid, H., Imtiaz, T., Mohammed, K. K., Cao, H., & Xiao, W. (2023). Dual Receiver-Based Naturally Decoupled Coil Structure with Improved Rotational Misalignment Tolerance for WPT systems. *IEEE Transactions on Transportation Electrification*, 1-1.
- Darvish, P., Mekhilef, S., & Illias, H. A. B. (2021). A Novel S–S–LCLCC Compensation for Three-Coil WPT to Improve Misalignment and Energy Efficiency Stiffness of Wireless Charging System. *IEEE Transactions on Power Electronics*, *36*(2), 1341-1355.
- Debbou, M., & Colet, F. (2016). Inductive wireless power transfer for electric vehicle dynamic charging. 2016 IEEE PELS Workshop on Emerging Technologies: Wireless Power Transfer (WoW) (pp. 118-122). IEEE.
- Dolara, A., Leva, S., Longo, M., Castelli-Dezza, F., & Mauri, M. (2017). Coil design and magnetic shielding of a resonant wireless power transfer system for electric vehicle battery charging. 2017 IEEE 6th International Conference on Renewable Energy Research and Applications (ICRERA) (pp. 200-205). IEEE.
- Erel, M. Z., Bayindir, K. C., Aydemir, M. T., Chaudhary, S. K., & Guerrero, J. M. (2021). A comprehensive review on wireless capacitive power transfer technology: Fundamentals and applications. *IEEE Access*, 10, 3116-3143.
- Green, A. W., & Boys, J. (1994). 10 kHz inductively coupled power transfer-concept and control.
- Hossain, A., Darvish, P., Mekhilef, S., Tey, K. S., & Tong, C. W. (2022). A New Coil Structure of Dual Transmitters and Dual Receivers With Integrated Decoupling Coils for Increasing Power Transfer and Misalignment Tolerance of Wireless EV Charging System. *IEEE Transactions on Industrial Electronics*, 69(8), 7869-7878.

- Hu, A. P., Liu, C., & Li, H. L. (2008). A novel contactless battery charging system for soccer playing robot. 2008 15th International Conference on Mechatronics and Machine Vision in Practice (pp. 646-650). IEEE.
- Huh, J., Lee, S. W., Lee, W. Y., Cho, G. H., & Rim, C. T. (2011). Narrow-width inductive power transfer system for online electrical vehicles. *IEEE Transactions on Power Electronics*, 26(12), 3666-3679.
- Hutin, M., & LeBlanc, M. (1894). Transform system for electric railways. In: Oct.
- Jadidian, J., & Katabi, D. (2014). Magnetic MIMO: How to charge your phone in your pocket. *Proceedings of the 20th annual international conference on Mobile computing and networking* (pp. 495-506).
- Jin, K., & Zhou, W. (2018). Wireless laser power transmission: A review of recent progress. *IEEE Transactions on Power Electronics*, *34*(4), 3842-3859.
- Kapranov, V., Matsak, I., Tugaenko, V. Y., Blank, A., & Suhareva, N. (2017). Atmospheric turbulence effects on the performance of the laser wireless power transfer system. *Free-Space Laser Communication and Atmospheric Propagation XXIX* (Vol. 10096, pp. 374-385). SPIE.
- Karalis, A., Joannopoulos, J. D., & Soljačić, M. (2008). Efficient wireless non-radiative mid-range energy transfer. *Annals of physics*, 323(1), 34-48.
- Kim, J., Kim, J., Kong, S., Kim, H., Suh, I.-S., Suh, N. P., Cho, D.-H., Kim, J., & Ahn, S. (2013). Coil design and shielding methods for a magnetic resonant wireless power transfer system. *Proceedings of the IEEE*, *101*(6), 1332-1342.
- Kim, S., Covic, G. A., & Boys, J. T. (2016). Tripolar pad for inductive power transfer systems for EV charging. *IEEE Transactions on Power Electronics*, 32(7), 5045-5057.
- Kim, S., Park, H.-H., Kim, J., Kim, J., & Ahn, S. (2014). Design and analysis of a resonant reactive shield for a wireless power electric vehicle. *IEEE Transactions on Microwave theory and techniques*, 62(4), 1057-1066.
- Kim, S., Zaheer, A., Covic, G., & Boys, J. (2014). Tripolar pad for inductive power transfer systems. *IECON 2014-40th Annual Conference of the IEEE Industrial Electronics Society* (pp. 3066-3072). IEEE.
- Kline, M., Izyumin, I., Boser, B., & Sanders, S. (2011). Capacitive power transfer for contactless charging. 2011 Twenty-Sixth Annual IEEE Applied Power Electronics Conference and Exposition (APEC) (pp. 1398-1404). IEEE.

- Kurs, A., Karalis, A., Moffatt, R., Joannopoulos, J. D., Fisher, P., & Soljacic, M. (2007). Wireless power transfer via strongly coupled magnetic resonances. *science*, 317(5834), 83-86.
- Ladan, S., Ghassemi, N., Ghiotto, A., & Wu, K. (2013). Highly efficient compact rectenna for wireless energy harvesting application. *IEEE microwave magazine*, 14(1), 117-122.
- Lashkari, K., Shladover, S. E., & Lechner, E. H. (1986). *Inductive power transfer to an electric vehicle. International Electric Vehicle Symposium* (8th: 1986: Washington DC).
- Lechner, E., & Shladover, S. E. (1986). Roadway powered electric vehicle: An all-electric hybrid system. *International Electric Vehicle Symposium* (8th) (No. CONF-8610122).
- Li, L., & Loo, B. P. Y. (2014). Alternative and Transitional Energy Sources for Urban Transportation. *Current Sustainable/Renewable Energy Reports*, *1*(1), 19-26.
- Li, S., Li, W., Deng, J., Nguyen, T. D., & Mi, C. C. (2014). A double-sided LCC compensation network and its tuning method for wireless power transfer. *IEEE Transactions on Vehicular Technology*, 64(6), 2261-2273.
- Li, S., Wang, L., Guo, Y., Tao, C., & Ji, L. (2020). Power Stabilization With Double Transmitting Coils and T-Type Compensation Network for Dynamic Wireless Charging of EV. *IEEE Journal of Emerging and Selected Topics in Power Electronics*, 8(2), 1801-1812.
- Li, X., Hu, J., Wang, H., Dai, X., & Sun, Y. (2020). A New Coupling Structure and Position Detection Method for Segmented Control Dynamic Wireless Power Transfer Systems. *IEEE Transactions on Power Electronics*, 35(7), 6741-6745.
- Li, Y., Hu, J., Li, X., Mai, R., Li, Z., Liu, M., & He, Z. (2020). Efficiency Analysis and Optimization Control for Input-Parallel Output-Series Wireless Power Transfer Systems. *IEEE Transactions on Power Electronics*, *35*(1), 1074-1085.
- Li, Y., Hu, J., Lin, T., Li, X., Chen, F., He, Z., & Mai, R. (2019). A New Coil Structure and Its Optimization Design With Constant Output Voltage and Constant Output Current for Electric Vehicle Dynamic Wireless Charging. *IEEE Transactions on Industrial Informatics*, 15(9), 5244-5256.
- Li, Y., Lin, T., Mai, R., Huang, L., & He, Z. (2018). Compact Double-Sided Decoupled Coils-Based WPT Systems for High-Power Applications: Analysis, Design, and Experimental Verification. *IEEE Transactions on Transportation Electrification*, 4(1), 64-75.

- Li, Y., Xu, Q., Lin, T., Hu, J., He, Z., & Mai, R. (2018). Analysis and design of load-independent output current or output voltage of a three-coil wireless power transfer system. *IEEE Transactions on Transportation Electrification*, 4(2), 364-375.
- Liu, C., Hu, A. P., & Budhia, M. (2010). A generalized coupling model for capacitive power transfer systems. *IECON 2010-36th Annual Conference on IEEE Industrial Electronics Society* (pp. 274-279). IEEE.
- Liu, J., Liu, Z., Chen, W., Sun, X., & Su, H. (2022). An Optimized Coil Array and Passivity-Based Control for Receiving Side Multilevel Connected DC-DC Converter of Dynamic Wireless Charging. *IEEE Transactions on Vehicular Technology*, 71(4), 3715-3726.
- Liu, S., Li, Y., Wu, Y., Zhou, L., Zhao, X., Mai, R., & He, Z. (2023). An Output Power Fluctuation Suppression Method of DWPT Systems Based on Dual-Receiver Coils and Voltage Doubler Rectifier. *IEEE Transactions on Industrial Electronics*, 70(10), 10167-10179.
- Liu, Y., Mai, R., Liu, D., Li, Y., & He, Z. (2017). Efficiency optimization for wireless dynamic charging system with overlapped DD coil arrays. *IEEE Transactions on Power Electronics*, 33(4), 2832-2846.
- Long, B. R., Miller, J. M., Daga, A., Schrafel, P. C., & Wolgemuth, J. (2016). Which way for wireless power: High Q or high k? 2016 IEEE PELS Workshop on Emerging Technologies: Wireless Power Transfer (WoW) (pp. 6-10). IEEE.
- Lu, F., Zhang, H., Hofmann, H., & Mi, C. C. (2016). A Dynamic Charging System With Reduced Output Power Pulsation for Electric Vehicles. *IEEE Transactions on Industrial Electronics*, 63(10), 6580-6590.
- Lu, X., Wang, P., Niyato, D., Kim, D. I., & Han, Z. (2015). Wireless charging technologies: Fundamentals, standards, and network applications. *IEEE Communications Surveys & Tutorials*, 18(2), 1413-1452.
- Lu, X., Wang, P., Niyato, D., Kim, D. I., & Han, Z. (2016). Wireless Charging Technologies: Fundamentals, Standards, and Network Applications. *IEEE Communications Surveys & Tutorials*, 18(2), 1413-1452.
- Ludois, D. C., Reed, J. K., & Hanson, K. (2012). Capacitive power transfer for rotor field current in synchronous machines. *IEEE Transactions on Power Electronics*, 27(11), 4638-4645.
- Lv, X., Dai, X., Jiang, C., & Wang, S. (2020). A Cross Double-D Coil for Electric Vehicles Dynamic Wireless Transfer System to Reduce Output Power Pulsation

- 2020 8th International Conference on Power Electronics Systems and Applications (PESA) (pp. 1-5). IEEE.
- Macharia, J. (2017). Wireless Inductive Charging for Low Power Devices.
- Matsumoto, H. (2002). Research on solar power satellites and microwave power transmission in Japan. *IEEE microwave magazine*, *3*(4), 36-45.
- Maxwell, J. C. (1873). A treatise on electricity and magnetism (Vol. 1). Clarendon press.
- Mi, C. C., Buja, G., Choi, S. Y., & Rim, C. T. (2016). Modern Advances in Wireless Power Transfer Systems for Roadway Powered Electric Vehicles. *IEEE Transactions on Industrial Electronics*, 63(10), 6533-6545.
- Miller, J. M., & Daga, A. (2015). Elements of wireless power transfer essential to high power charging of heavy duty vehicles. *IEEE Transactions on Transportation Electrification*, 1(1), 26-39.
- Mohamed, A. A., Lashway, C. R., & Mohammed, O. (2017). Modeling and feasibility analysis of quasi-dynamic WPT system for EV applications. *IEEE Transactions on Transportation Electrification*, *3*(2), 343-353.
- Mohamed, A. A., Shaier, A. A., Metwally, H., & Selem, S. I. (2020). A comprehensive overview of inductive pad in electric vehicles stationary charging. *Applied Energy*, 262, 114584.
- Mohamed, A. A., Shaier, A. A., Metwally, H., & Selem, S. I. (2022). An overview of dynamic inductive charging for electric vehicles. *Energies*, 15(15), 5613.
- Mohamed, A. A. S., & Mohammed, O. (2018). Physics-Based Co-Simulation Platform With Analytical and Experimental Verification for Bidirectional IPT System in EV Applications. *IEEE Transactions on Vehicular Technology*, 67(1), 275-284.
- Mohamed, A. A. S., Shaier, A. A., Metwally, H., & Selem, S. I. (2022). An Overview of Dynamic Inductive Charging for Electric Vehicles. *Energies*, *15*(15).
- Mohamed, N., Aymen, F., Alqarni, M., Turky, R. A., Alamri, B., Ali, Z. M., & Aleem, S. H. A. (2022). A new wireless charging system for electric vehicles using two receiver coils. *Ain Shams Engineering Journal*, 13(2), 101569.
- Moon, S., Kim, B.-C., Cho, S.-Y., Ahn, C.-H., & Moon, G.-W. (2014). Analysis and design of a wireless power transfer system with an intermediate coil for high efficiency. *IEEE Transactions on Industrial Electronics*, 61(11), 5861-5870.

- Moon, S., & Moon, G.-W. (2015). Wireless power transfer system with an asymmetric four-coil resonator for electric vehicle battery chargers. *IEEE Transactions on Power Electronics*, 31(10), 6844-6854.
- Mukhatov, A., Bagheri, M., Dehghanian, P., Carabias, V., & Gharehpetian, G. (2018). Reduction of output power pulsations for electric vehicles by changing distances between transmitter coils. 2018 7th International Conference on Renewable Energy Research and Applications (ICRERA) (pp. 307-312). IEEE.
- Musavi, F., Edington, M., & Eberle, W. (2012). Wireless power transfer: A survey of EV battery charging technologies. 2012 IEEE Energy Conversion Congress and Exposition (ECCE) (pp. 1804-1810). IEEE.
- Neaimeh, M., Wardle, R., Jenkins, A. M., Yi, J., Hill, G., Lyons, P. F., Hübner, Y., Blythe, P. T., & Taylor, P. C. (2015). A probabilistic approach to combining smart meter and electric vehicle charging data to investigate distribution network impacts. *Applied Energy*, 157, 688-698.
- Onar, O. C., Campbell, S. L., Seiber, L. E., White, C. P., Chinthavali, M. S., Tang, L., Chambon, P. H., Ozpineci, B., & Smith, D. E. (2016). *Oak ridge national laboratory wireless charging of electric vehicles-CRADA report*.
- Onar, O. C., Miller, J. M., Campbell, S. L., Coomer, C., White, C. P., & Seiber, L. E. (2013). A novel wireless power transfer for in-motion EV/PHEV charging. 2013 Twenty-Eighth Annual IEEE Applied Power Electronics Conference and Exposition (APEC) (pp. 3073-3080). IEEE.
- Panchal, C., Stegen, S., & Lu, J. (2018). Review of static and dynamic wireless electric vehicle charging system. *Engineering science and technology, an international journal*, 21(5), 922-937.
- Patil, D., McDonough, M. K., Miller, J. M., Fahimi, B., & Balsara, P. T. (2017). Wireless power transfer for vehicular applications: Overview and challenges. *IEEE Transactions on Transportation Electrification*, 4(1), 3-37.
- Patil, D., McDonough, M. K., Miller, J. M., Fahimi, B., & Balsara, P. T. (2018). Wireless Power Transfer for Vehicular Applications: Overview and Challenges. *IEEE Transactions on Transportation Electrification*, 4(1), 3-37.
- Protection, I. C. o. N.-I. R. (2010). Guidelines for limiting exposure to time-varying electric and magnetic fields (1 Hz to 100 kHz). *Health physics*, 99(6), 818-836.
- Regensburger, B., Sinha, S., Kumar, A., Vance, J., Popovic, Z., & Afridi, K. K. (2018). Kilowatt-scale large air-gap multi-modular capacitive wireless power transfer

- system for electric vehicle charging. 2018 IEEE applied power electronics conference and exposition (APEC) (pp. 666-671). IEEE.
- Roßkopf, A., Bär, E., & Joffe, C. (2013). Influence of inner skin-and proximity effects on conduction in litz wires. *IEEE Transactions on Power Electronics*, 29(10), 5454-5461.
- Shi, K., Tang, C., Long, H., Lv, X., Wang, Z., & Li, X. (2021). Power fluctuation suppression method for EV dynamic wireless charging system based on integrated magnetic coupler. *IEEE Transactions on Power Electronics*, *37*(1), 1118-1131.
- Shi, K., Tang, C., Wang, Z., Li, X., Zhou, Y., & Fei, Y. (2022). A Magnetic Integrated Method Suppressing Power Fluctuation for EV Dynamic Wireless Charging System. *IEEE Transactions on Power Electronics*, 37(6), 7493-7503.
- Shin, J., Shin, S., Kim, Y., Ahn, S., Lee, S., Jung, G., Jeon, S.-J., & Cho, D.-H. (2013). Design and implementation of shaped magnetic-resonance-based wireless power transfer system for roadway-powered moving electric vehicles. *IEEE Transactions on Industrial Electronics*, 61(3), 1179-1192.
- Shinohara, N. (2010). Beam efficiency of wireless power transmission via radio waves from short range to long range. *Journal of the Korean Institute of Electromagnetic and Science*, 10(4), 224-230.
- Shinohara, N., Kubo, Y., & Tonomura, H. (2013). Wireless charging for electric vehicle with microwaves. 2013 3rd International Electric Drives Production Conference (EDPC) (pp. 1-4). IEEE.
- Shladover, S. E. (1988). Systems engineering of the roadway powered electric vehicle technology. *INTERNATIONAL ELECTRIC VEHICLE SYMPOSIUM (9TH:*.
- Siqi, L., & Mi, C. C. (2015). Wireless Power Transfer for Electric Vehicle Applications. *IEEE Journal of Emerging and Selected Topics in Power Electronics*, 3(1), 4-17.
- Solvi Hoen, F., Díez-Gutiérrez, M., Babri, S., Hess, S., & Tørset, T. (2023). Charging electric vehicles on long trips and the willingness to pay to reduce waiting for charging. Stated preference survey in Norway. *Transportation Research Part A: Policy and Practice*, 175.
- Song, B., Du, B., Cui, S., Li, Y., & Zhu, C. (2021). Mechanism analysis of output fluctuation in a three-phase dynamic wireless charging system. *IEEE Transactions on Industrial Electronics*, 69(3), 2252-2264.

- Takanashi, H., Sato, Y., Kaneko, Y., Abe, S., & Yasuda, T. (2012). A large air gap 3 kW wireless power transfer system for electric vehicles. 2012 IEEE energy conversion congress and exposition (ECCE) (pp. 269-274). IEEE.
- Tesla, N. (1914). *U.S. Patent No. 1,119,732*. Washington, DC: U.S. Patent and Trademark Office.
- Thrimawithana, D. J., Madawala, U. K., & Neath, M. (2011). A synchronization technique for bidirectional IPT systems. *IEEE Transactions on Industrial Electronics*, 60(1), 301-309.
- Triviño-Cabrera, A., González-González, J. M., & Aguado, J. A. (2020). Wireless power transfer for electric vehicles: foundations and design approach.
- Tseng, V. F.-G., Bedair, S. S., & Lazarus, N. (2017). Acoustic wireless power transfer with receiver array for enhanced performance. 2017 IEEE Wireless Power Transfer Conference (WPTC) (pp. 1-4). IEEE.
- Wang, H., Wu, Y., Shen, Z., Pan, W., Chen, X., & Zhang, Y. (2024). High-Misalignment-Tolerant Dual-Channel Inductive Power Transfer System Based on Cross-Shaped Reversed-Winding-Incorporated Solenoid Pad. *IEEE Transactions on Industrial Electronics*.
- Wang, S., & Dorrell, D. (2013). Review of wireless charging coupler for electric vehicles. *IECON 2013-39th Annual Conference of the IEEE Industrial Electronics Society* (pp. 7274-7279). IEEE.
- Wang, Y., Lin, F., Yang, Z., Cai, P., & Liu, Z. (2018). Coils layout optimization of dynamic wireless power transfer system to realize output voltage stable. 2018 International Power Electronics Conference (IPEC-Niigata 2018-ECCE Asia) (pp. 3495-3500). IEEE.
- Wojda, R. P., & Kazimierczuk, M. K. (2018). Winding resistance and power loss of inductors with litz and solid-round wires. *IEEE Transactions on Industry Applications*, 54(4), 3548-3557.
- Xiang, L., Li, X., Tian, J., & Tian, Y. (2018). A Crossed DD Geometry and Its Double-Coil Excitation Method for Electric Vehicle Dynamic Wireless Charging Systems. *IEEE Access*, 6, 45120-45128.
- Xiang, L., Sun, Y., Tang, C., Dai, X., & Jiang, C. (2017). Design of crossed DD coil for dynamic wireless charging of electric vehicles. 2017 IEEE PELS Workshop on Emerging Technologies: Wireless Power Transfer (WoW) (pp. 1-5). IEEE.

- Yilmaz, M., & Krein, P. T. (2013). Review of Battery Charger Topologies, Charging Power Levels, and Infrastructure for Plug-In Electric and Hybrid Vehicles. *IEEE Transactions on Power Electronics*, 28(5), 2151-2169.
- Yin, J., Mekhilef, S., Darvish, P., Mokhlis, H., & Soon, T. K. (2024). A New Cross-Overlapped Decoupling Coil Structure for EV Dynamic Inductive Wireless Charging System. *IEEE Transactions on Industrial Electronics*, 1-11.
- Zaheer, A., Covic, G. A., & Kacprzak, D. (2013). A bipolar pad in a 10-kHz 300-W distributed IPT system for AGV applications. *IEEE Transactions on Industrial Electronics*, 61(7), 3288-3301.
- Zhang, J., Yuan, X., Wang, C., & He, Y. (2016). Comparative analysis of two-coil and three-coil structures for wireless power transfer. *IEEE Transactions on Power Electronics*, 32(1), 341-352.
- Zhang, X., Zhu, C., & Song, H. (2022). Wireless Power Transfer Technologies for Electric Vehicles. Springer.
- Zhou, H., Shen, Z., Wu, Y., Chen, X., & Zhang, Y. (2024). A Stable Dynamic Electric Vehicle Wireless Charging System Based on Triple Decoupling Receiving Coils and a Novel Triple-Diode Rectifier. *IEEE Transactions on Industrial Electronics*, 71(10), 12011-12018.